Geological Society of America Bulletin

Switch from thrusting to normal shearing in the Zanskar shear zone, NW Himalaya: Implications for channel flow

Melanie Finch, Pavína Hasalová, Roberto F. Weinberg and C. Mark Fanning

---

Email alerting services	click www.gsapubs.org/cgi/alerts to receive free e-mail alerts when new articles cite this article
Subscribe	click www.gsapubs.org/subscriptions/ to subscribe to Geological Society of America Bulletin
Permission request	click http://www.geosociety.org/pubs/copyrt.htm#gsa to contact GSA

Notes

THE
GEOLOGICAL
SOCIETY
OF AMERICA

Switch from thrusting to normal shearing in the Zanskar shear zone, NW Himalaya: Implications for channel flow

Melanie Finch[1,†], Pavlína Hasalová[1,2,§], Roberto F. Weinberg[1], and C. Mark Fanning[3]
[1]*School of Geosciences, Monash University, Clayton, Victoria 3800, Australia*
[2]*Centre for Lithospheric Research, Czech Geological Survey, Klárov 3, 118 21 Prague 1, Czech Republic*
[3]*Research School of Earth Sciences, Australian National University, Mills Road, Canberra, ACT 0200, Australia*

ABSTRACT

The Zanskar shear zone is a ductile, normal-sense shear zone that exploited the contact between the High Himalayan Crystalline series and the Tethyan sedimentary series. The Zanskar shear zone is an extension of the South Tibetan detachment system with similar timing and nature, and, in Zanskar, it accommodated 24 km of normal movement. Early thrusting is preserved in the footwall and hanging wall and is overprinted by normal shearing. Thrusting and normal shearing were coplanar and codirectional, with SW-directed thrusting overprinted by NE-directed normal shearing—a simple inversion of movement sense. The telescoped isograds related to normal shearing define a broad pattern of colder rocks on top of hotter. However, we found preserved thrust-related metamorphic series, with hotter rocks on top of colder, severely telescoped by normal shearing. Some determinations of the amount of displacement and thinning on the Zanskar shear zone prior to the current work have assumed a steady-state crustal profile and have disregarded preexisting perturbations of isograds such as those indicated here. Miocene leucogranitic intrusions accumulated within and below the normal Zanskar shear zone. Intrusions were sheared during thrusting and normal movement, and magmatism outlasted normal shearing. We have dated monazites by U-Pb sensitive high-resolution ion microprobe (SHRIMP) from leucogranite samples that were sheared by the thrusting event, by the normal movement event, and those that postdate all shearing. Results constrain the timing of the switch from thrusting to normal movement to between 26 and 24 Ma and ca. 22 Ma. At ca. 20 Ma, normal shearing in Zanskar shear zone was no longer active, and magmatism was waning, producing late, undeformed leucogranitic dikes. Taking into account the shear zone thickness of 0.83 km, the maximum duration of normal movement of 6 m.y., and the estimated strain of $\gamma = 28.6$, we estimate the lower bound of strain rate for the Zanskar shear zone to be 1.5×10^{-13} s^{-1}. Given the short duration of the normal shearing event and magmatism, we find little support for the hypothesis of channel flow in Zanskar. We propose instead that Miocene anatexis weakened the midcrustal levels and caused the switch from thrusting to normal movement, doming, and cooling of the anatectic core of the High Himalayan Crystalline series.

INTRODUCTION

The Himalayas are the result of the N-S collision of the Indian and Asian continental plates, which commenced at ca. 55–50 Ma (e.g., Rowley, 1996). As the type example of collisional orogenesis, the structures that accommodated shortening and thickening have been well documented. Large-scale thrust faults with remarkable lateral continuity strike parallel to the orogeny; the Main Central thrust is one such example (Fig. 1A). To the north of and parallel to the Main Central thrust, there lies the South Tibetan detachment system (Fig. 1A; e.g., Burg and Chen, 1984; Burchfiel and Royden, 1985), a series of normal-sense shear zones that are found along the entire 2400 km length of the Himalaya. While large-scale normal fault movement is not a typical prediction of active collisional regimes, the South Tibetan detachment system has been active since at least the Miocene, locally temporally coincident with movement on the Main Central thrust to the south (Fig. 1A; Hodges et al., 1996; Vannay and Hodges, 1996;

Coleman, 1998; Murphy and Harrison, 1999; Hurtado et al., 2001; Harris et al., 2004; Vannay et al., 2004; Godin et al., 2006). Coeval movement on these shear zones with opposite shear sense between 24 and 12 Ma (Hodges et al., 1996; Vannay and Hodges, 1996; Coleman, 1998; Harris et al., 2004; Vannay et al., 2004; Godin et al., 2006) resulted in the extrusion of the High Himalayan Crystalline sequence (Fig. 1A), the metamorphic core of the Himalaya.

The High Himalayan leucogranites (Fig. 1A) intrude the top of the High Himalayan Crystalline sequence at the contact with the overlying Tethyan sedimentary series, a sequence of metasedimentary rocks deposited in a marine setting (Fuchs, 1987). Leucogranites outcrop sporadically along the length of the Himalaya, and their genesis is attributed to: (1) thrust movement on the Main Central thrust causing devolatilization of the footwall and consequent fluid-present melting of the hanging wall (e.g., Le Fort et al., 1987); (2) shear heating focused around the Main Central thrust (e.g., Harrison et al., 1998); and (3) normal movement on the South Tibetan detachment system, causing decompression melting in its footwall (e.g., Dézes et al., 1999; Walker et al., 1999).

A great deal of research has been conducted on the field relationships between the High Himalayan Crystalline sequence and the South Tibetan detachment system to explain why normal movement occurs within an overall compressive setting (e.g., Dézes et al., 1999; Grujic et al., 1996; Law et al., 2004; Godin et al., 2006; Cottle et al., 2007; Webb et al., 2007, 2011; Kellett and Godin, 2009; Long and McQuarrie, 2010; Kellett and Grujic, 2012). Field-based research has been accompanied by numerical models to understand the physical processes that underlie deformation and the conditions that favor extrusion of the High Himalayan Crystalline sequence (Beaumont et al., 2001, 2004, 2006; Jamieson et al., 2004, 2006). One model that has received wide support is that of channel
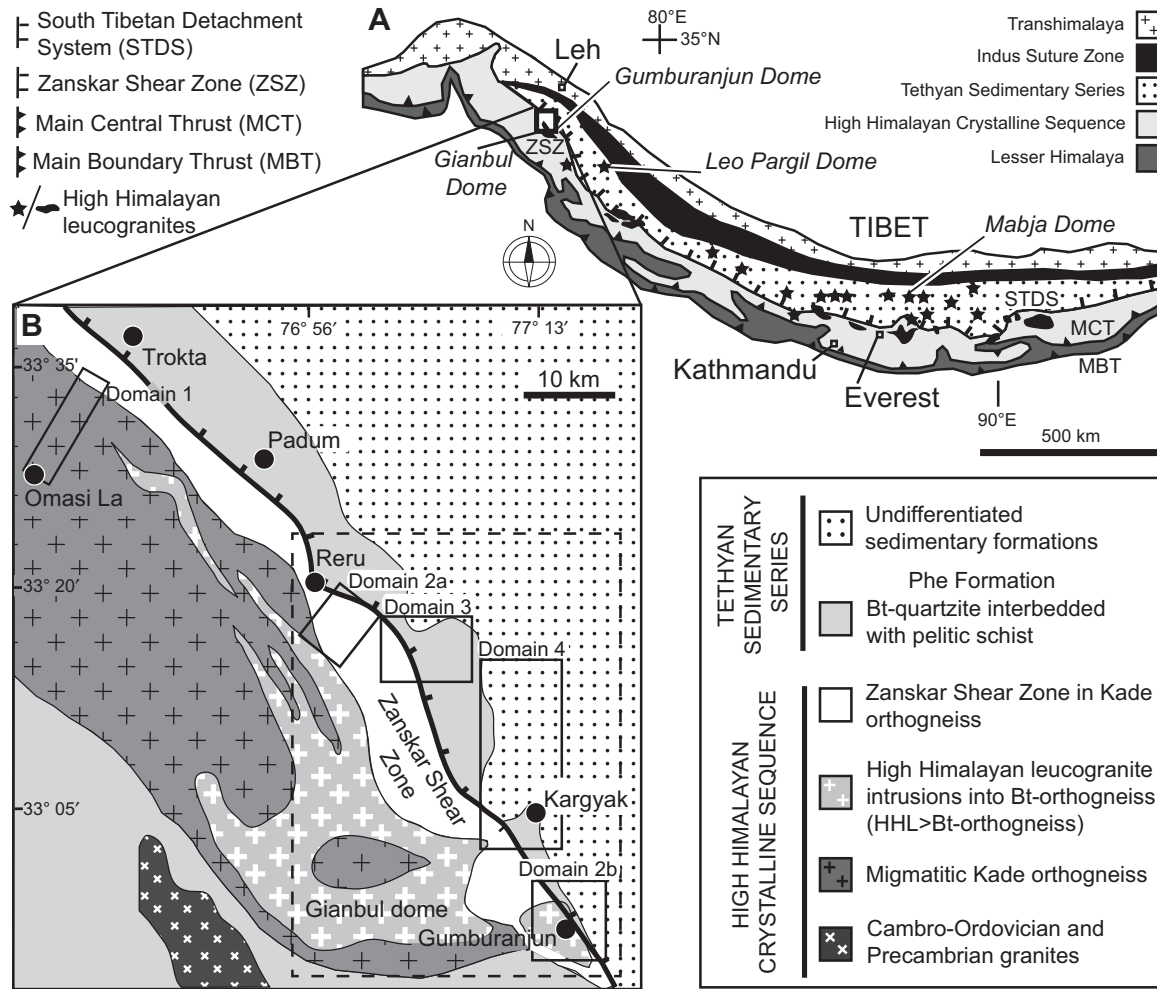
Figure 1. (A) Simplified geological map of the Himalaya including major faults, lithologies, and leucogranite intrusions (adapted from Herren, 1987; Dézes, 1999). Location of studied area in Zanskar is indicated by rectangle. Small (unmappable) leucogranite intrusions are shown as stars. (B) Detailed geological map of studied area. Four domains were defined (rectangles) based on distinct structural and lithological characteristics. Dashed rectangle indicates area shown in Figure 2.

flow, which posits that a region in the midcrust underwent partial melting, which, in combination with lateral pressure gradients related to topography and focused erosion, caused it to tunnel through the overriding crust and extrude at the erosional front of the Himalaya as the High Himalayan Crystalline sequence (e.g., Beaumont et al., 2004; Jamieson et al., 2004). While numerous studies have examined the applicability of the channel-flow model for the central Himalaya, considerably fewer have explored the NW Himalaya (e.g., Dézes, 1999; Robyr et al., 2006; Webb et al., 2007; Mukherjee and Koyi, 2010). In this region, the complete succession of the system, from the Main Central thrust through to the South Tibetan detachment system, is exposed (Fig. 1B), with the higher reaches close to and across the South Tibetan

detachment system, well exposed in Zanskar (NW India; Figs. 1B and 2), where the South Tibetan detachment system is known as the Zanskar shear zone (Herren, 1987).

Zanskar is bordered by the Ladakh Range to the northeast and the Great Himalayan Range to the southwest (e.g., Dézes, 1999). The channel flow model potentially explains many of the features of the Zanskar shear zone, including: (1) anatexis resulting from dehydration melting (perhaps combined with fluid present melting) and leucogranite intrusion at the top of the High Himalayan Crystalline sequence (Pognante and Lombardo, 1989; Pognante, 1992; Dézes et al., 1999; Walker et al., 1999); (2) the presence of a complete and locally telescoped Barrovian metamorphic series (Searle, 1986; Herren, 1987; Pognante and Lombardo, 1989; Pognante

et al., 1990; Pognante, 1992; Noble and Searle, 1995; Dézes, 1999; Searle et al., 1999; Walker et al., 2001); and (3) a pervasive normal shear zone that overprints an earlier thrust system (Herren, 1987; for a complete list of channel-flow predictions, see Grujic, 2006). However, in the western Himalayas, the initiation and duration of magmatism in the upper part of the High Himalayan Crystalline sequence are only poorly constrained, and the same is true with regard to the duration of normal movement on the South Tibetan detachment system, both of which are crucial factors needed to determine whether channel flow was a significant process. In order to constrain these events, this study focuses on the structural evolution of the Zanskar shear zone and surroundings, with particular focus on the overprinting of the thrusting phase by

Switch from thrusting to normal shearing in the Zanskar shear zone, NW Himalaya: Implications for channel flow
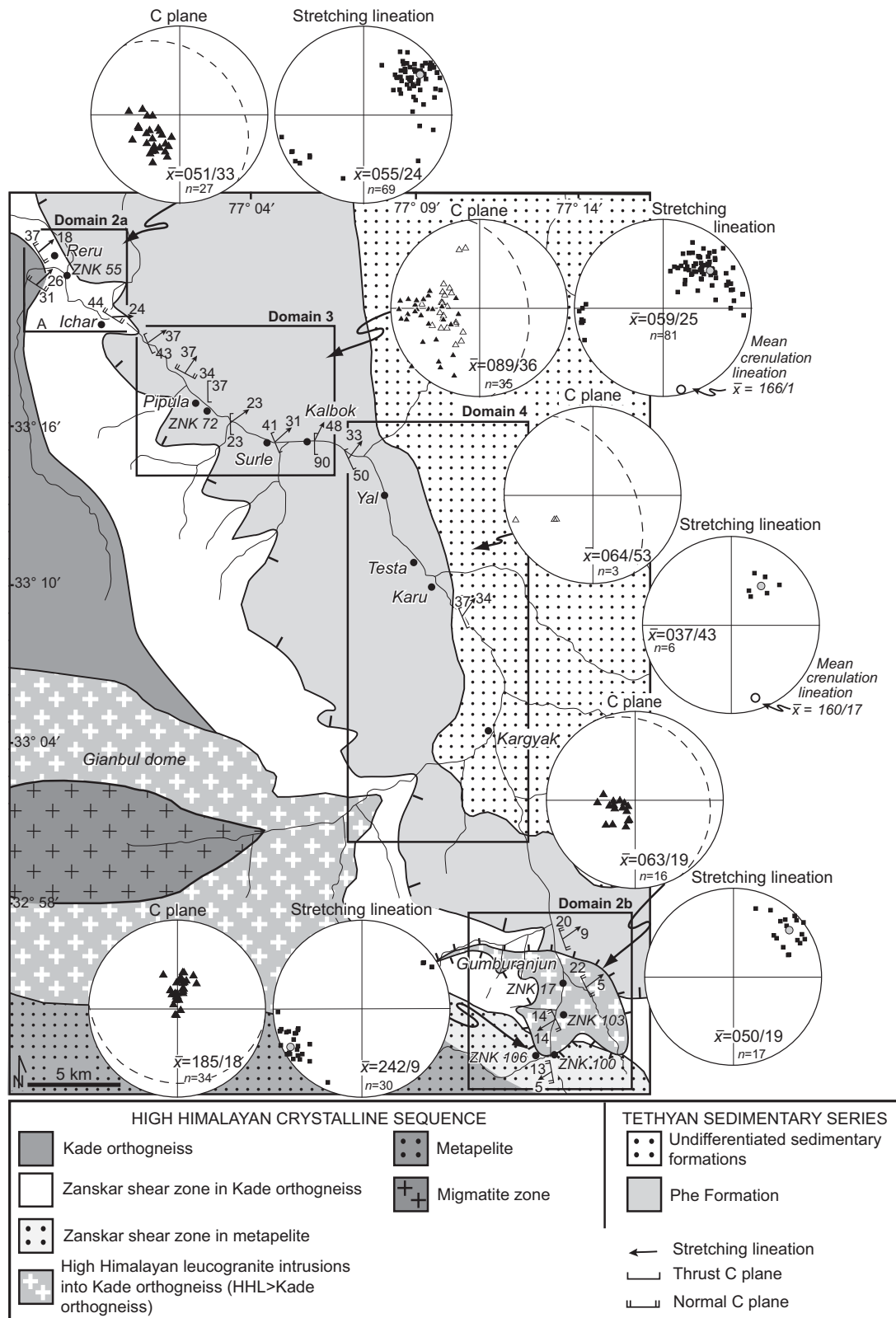
Figure 2. Detailed geological map of studied area. Structural domains are marked by black rectangles. Structural data are from this study; the distribution of lithologies combines our observations, generally restricted to the vicinity of the Kargyak River, and data from Dézes et al. (1999) and Landsat images. "ZNK" is sample label. Stereographic projections of C planes related to normal shearing (black triangles) and thrusts (white triangles), and stretching lineation (circles) for each domain are shown. Projections are lower hemisphere, equal area, with the mean plane ($\bar{x}$; dashed great circle), mean lineation (gray circle), and number of measurements (*n*) indicated.

ductile normal shearing, and the timing of magmatism, which brackets the duration of normal movement. The results constrain the timing of the shear sense reversal and its relationship to crustal melting and magmatism, thus assisting in determination of mechanisms for extrusion of the High Himalayan Crystalline sequence.

REGIONAL GEOLOGY

This work focuses on an ~50 km along-strike section of the Zanskar shear zone in eastern Zanskar and includes orthogneisses of the High Himalayan Crystalline sequence and metasedimentary rocks of the base of the Tethyan sedimentary series (Figs. 1 and 2). Following others, the term Zanskar shear zone refers here to a zone of intense normal shearing, characteristically restricted to the orthogneisses and metapelites of the High Himalayan Crystalline sequence, immediately below the Tethyan sedimentary series. This definition excludes the pervasive thrusting recorded by rocks in both the hanging wall and footwall of the Zanskar shear zone that defines an earlier event (Patel et al., 1993; Robyr et al., 2002).

The Zanskar shear zone strikes parallel to the Himalayan mountain chain, approximately NE-SW, for ~150 km through Zanskar (Dézes, 1999). The uppermost level of the High Himalayan Crystalline sequence is bounded by the Zanskar shear zone and contains two generations of intrusions (Robyr et al., 2002). The earlier intrusive cycle took place at 472 Ma (+9/–6 Ma; U-Pb zircon, thermal ionization mass spectrometry [TIMS]; Pognante et al., 1990) and consisted of massive batholiths of shallow-level granitic intrusions ($^{87}Sr/^{86}Sr_i$ = 0.718; Pognante et al., 1990). The granite was deformed and metamorphosed to porphyritic two-mica orthogneiss, known as the Kade orthogneiss (Pognante et al., 1990; Robyr et al., 2002), consisting of Qtz + Kfs + Pl + Bt + Ms ± Tur ± Grt (mineral abbreviations are after Kretz, 1983). In some areas, rafts of metapelites are present, indicating that this was the country rock into which the Paleozoic granite intruded. The metapelites are very fine grained, with an assemblage of Qtz + Kfs + Pl + Bt + Ms ± Grt ± Tur ± Sil. Dézes (1999) also reported rare kyanite in these metapelites. The Kade orthogneiss and surrounding country rock were metamorphosed and partially melted during the Himalayan orogeny to form the second intrusive cycle (Pognante, 1992). The second cycle consisted of leucogranitic sills, dikes, and lenses (Pognante, 1992) containing Qtz + Kfs + Pl + Ms ± Bt ± Tur ± Grt. The leucogranites have been dated at a range of ages between ca. 37 and 20 Ma (TIMS U-Pb monazite—Dézes, 1999; TIMS U-Pb uraninite and monazite—Walker et al., 1999; TIMS and secondary ion mass spectrometry [SIMS] U-Pb monazite—Robyr et al., 2006) and commonly include inherited monazites from the Kade orthogneiss (ca. 500–450 Ma) and other older sources. Ages at the upper limit of this spectrum (ca. 37–28 Ma) were interpreted to date the thermal peak or near-peak of the regional metamorphism, and the younger ages (ca. 25–20 Ma) represent crystallization ages of these leucogranites (e.g., Walker et al., 1999; Horton, 2011).

The leucogranites are part of a broader magmatic series known as the High Himalayan leucogranites (Le Fort et al., 1987; Coleman, 1998; Harrison et al., 1998, 1999; Lee et al., 2004, 2006; Zhang et al., 2004), which are found sporadically along the length of the High Himalaya (Fig. 1A) and are variably concordant with layering. Minor anatexis in the Himalaya began in the Oligocene (e.g., Viskupic et al., 2005; Lee et al., 2006; Rubatto et al., 2013), with the major stage of partial melting in the early-middle Miocene (e.g., Coleman, 1998; Harrison et al., 1998; Harris et al., 2004; Robyr et al., 2006). In a few localities, such as the Gumburanjun dome, an offshoot of the larger Gianbul dome in Zanskar (Dézes et al., 1999; Figs. 1 and 2), the intrusions coalesce immediately underneath the normal shear zone, or in association with strike-slip shear zones, to form large composite granitic plutons (Le Fort et al., 1987; Pognante, 1992; Coleman, 1998; Harrison et al., 1999; Walker et al., 1999; Weinberg et al., 2009), forming domes resulting from thinning of the cover and rise of the low-density plutons (Lee et al., 2004). In Zanskar and many other locations in the Himalaya, the intrusions cease at the boundary between the High Himalayan Crystalline sequence and the Tethyan sedimentary series, indicating that the contact, whether tectonic or lithologic, controlled their emplacement (Dézes et al., 1999). There are also some rare reports of leucogranites that intrude metamorphosed lithologies above the High Himalayan Crystalline sequence (e.g., Haimanta Unit—Thöni et al., 2012; Tethyan sedimentary series—Guillot et al., 1994). The Zanskar shear zone (Figs. 1B and 2) is recognized in the field by zones of high strain up to 7 km wide (Searle, 1986; Herren, 1987; Pognante et al., 1990; Pognante, 1992; Noble and Searle, 1995; Dézes, 1999; Walker et al., 2001). In the studied area, the Zanskar shear zone is characterized by a normal sense of displacement in strongly sheared Kade orthogneiss intruded by dikes of High Himalayan leucogranites (Fig. 2). To the northeast and overlying the Zanskar shear zone, the Tethyan sedimentary Series (Fig. 2) consists of interbedded biotite-quartzite and biotite-mus-covite schist with dolomite nodules defining the Phe Formation at the base of the sequence (Nanda and Singh, 1976; Fuchs, 1987). This sequence becomes intercalated with layers of dolomite, with the first significant layer of dolomite marking the base of the Karsha Formation (Nanda and Singh, 1976; Fuchs, 1987; Dézes, 1999). The schist is fine grained and consists dominantly of Qtz + Kfs + Pl + Bt + Ms + Chl. The layers of schist are ~2–20 cm thick and are generally thinner and more deformed than the biotite-quartzite, which consists of layers up to a meter thick. The biotite-quartzite is fine grained and contains Qtz + Bt ± Pl ± Ms ± Grt ± Fe-oxides ± Chl. Dolomite is typically orange to yellow in color and forms layers in the Karsha Formation, becoming thick up sequence to the NE, where dolomite layers attain thickness of a few hundred meters. This sedimentary sequence is interpreted to have been deposited in a shallow-marine setting on the northern margin of the Indian plate between the Upper Precambrian and Middle Cambrian (Fuchs, 1987). As a result of collision, the Tethyan sedimentary series was folded and imbricated, and it forms a 100-km-wide synclinorium in NW India consisting of several nappes (Dézes, 1999).

Migmatites in the High Himalayan Crystalline sequence reached muscovite-dehydration melting conditions, which, perhaps combined with fluid-present melting, formed the Miocene leucogranites (Pognante, 1992; Robyr et al., 2006). In the studied area, the Zanskar shear zone is marked by a sharp decrease in metamorphic grade over the thickness of the shear zone, with migmatites at the southwest margin in the footwall grading to greenschist facies just outside and to the northeast of the shear zone in the hanging wall. In other regions, the Zanskar shear zone is marked by a Barrovian metamorphic series, which grades over 1 km (the thickness of the Zanskar shear zone) from the kyanite zone to the biotite zone and then abruptly to lower greenschist facies at the base of the Tethyan sedimentary series (Dézes, 1999), or is part of a Barrovian metamorphic series that continues into the footwall but is severely telescoped in the Zanskar shear zone (Herren, 1987; Searle et al., 1999). Vance and Harris (1999) found that prograde regional metamorphism in Zanskar continued until 20 Ma and was attributed to burial as a result of SW-directed thrusting.

In the central and eastern Himalaya, the High Himalayan Crystalline sequence is bounded by the Main Central thrust below and the South Tibetan detachment system above (Yin, 2006). In contrast, the hanging wall of the Main Central thrust in Zanskar (SW of the studied area) consists of low- to medium-grade rocks, and the high-grade High Himalayan Crystalline

Switch from thrusting to normal shearing in the Zanskar shear zone, NW Himalaya: Implications for channel flow

sequence spans only a narrow area underneath the Zanskar shear zone.

In their models of channel flow, Beaumont et al. (2004) proposed a number of mechanisms for doming in the Himalaya, including thinning of the upper crust above the channel and subsequent inflation and doming of the channel to fill the space, or doming caused by underthrusting of the footwall and uplift of the channel. Beaumont et al. (2001) suggested that doming can occur when the upper crust overriding the channel is weak and the denudation rate is insufficient to induce channeling at the Main Central thrust. In such a case, the High Himalayan Crystalline sequence may pierce through the upper crust as domes, in a position more internal to the range. Robyr et al. (2002) attributed reduced erosion to the lack of major river systems in the NW Himalaya near the Main Central thrust. While Beaumont et al. (2001) suggested that such domes may form at sites of extension, it is not known whether normal shearing on the Zanskar shear zone induced doming or was a consequence of it (Robyr et al., 2002).

STRUCTURAL AND MICROSTRUCTURAL OBSERVATIONS

On the basis of structural and lithological differences, the area studied was divided into four domains (Figs. 1 and 2). The domains correspond to different structural levels of the shear zone and are described from the shear zone footwall toward its hanging wall (Fig. 3). The broad features of each domain will be described before detailing their structures and rock characteristics. Microstructural work has been done in order to decipher distinct deformation features in the domains and better constrain the relationship between normal and reverse shearing. Thin sections were cut perpendicular to foliation and parallel to stretching lineation (*x-z* section). The stretching lineation was defined by aligned biotite and muscovite grains, and stretched quartz and feldspars grains.

Domain 1: Thrusting in the Zanskar Shear Zone Footwall

Domain 1 consists of the footwall of the Zanskar shear zone, investigated in the Malung Thokpo valley (see Herren, 1987) close to the village of Trokta (Figs. 1, 3, and 4), NW of and isolated from domains 2–4. This valley drains the interior of the Zanskar Mountains and is oriented NNE-SSW (Fig. 4). The Zanskar shear zone is exposed for 1 km SW of the village of Trokta, and, like in domains 2 and 3, the shear zone places low-grade metasedimentary rocks of the Tethyan sedimentary series hanging wall in contact with high-grade migmatitic Kade orthogneisses of the High Himalayan Crystalline sequence. Kade orthogneiss is intruded by Tur-Grt-Ms-Bt leucogranites (Fig. 4), typically forming foliation-parallel sills, varying in thickness from centimetric to hectometric, and have a gneissic or mylonitic fabric (Fig. 5).

Normal shearing of the Zanskar shear zone gives way gradually to pervasive ductile thrusting recorded by both the migmatitic orthogneisses and leucogranite sills (Fig. 5). Between the SW margin of the Zanskar shear zone and the more distant footwall, there is a transition zone where normal shearing overprints thrusting (Fig. 4). This zone extends to the Zungkul Monastery (Fig. 4), beyond which the footwall is accessible and well exposed at low altitudes. Significantly, we note that leucogranites here are mineralogically and texturally identical to leucogranites within the Zanskar shear zone or in the thrusted areas toward the core of the mountains. The normal and reverse shear planes have essentially the same attitude ($\overline{x}$ = 70/37, notation for planes is dip direction/dip) and the same stretching lineation ($\overline{x}$ = 57/30; Fig. 4).

There are numerous indicators of shear sense, including S-C-C′, K-feldspar porphyroblasts or leucosomes, asymmetrically sheared leucogranite dikes, and verging, asymmetric, isoclinal

fold trains developed around rheological heterogeneities (Fig. 5). That the normal shearing overprints thrusting is evidenced by competent mafic lithons, 10 m or more in length and several meters in height, with normal shearing in the outer 50 cm and in the surroundings, and reverse shearing preserved in the core of the lithon (Figs. 5A–5D). Leucogranite intrusions, similar to those found in the normal shear zone, as well as leucosomes in the orthogneiss (Fig. 5E–F) record the thrusting event suggesting that peak temperature conditions were likely associated with thrusting.

Domain 2: Zanskar Shear Zone

Domain 2 corresponds to the Zanskar shear zone proper, characterized by top-down-to-the-NE normal shearing, which is exposed in two places: in the Reru area (domain 2a) and in the Gumburanjun area (domain 2b; Fig. 2). These two domains are described separately.

Zanskar Shear Zone: Reru Area (Domain 2a)

The Reru area comprises the entire thickness of the Zanskar shear zone, which is exposed between the villages of Reru and Ichar (Fig. 2). Domain 2a is characterized by ductile, top-down-to-the-NE normal shearing (Figs. 2, 3, 6, 7A, and 7C). Rocks here are dominantly mylonitic Kade orthogneiss, consisting of Qtz + Kfs + Pl + Bt + Ms ± Grt ± Tur (Pognante and Lombardo, 1989; Pognante, 1992). These are intruded by leucogranites with essentially the same mineralogy. This domain is bounded on the southwestern side by weakly to highly deformed rocks of a similar lithology, and on the northeastern side by the Phe Formation, the basal formation of the Tethyan sedimentary series (Fig. 2).

The dominant foliation is the shear plane, C, which dips moderately to the NE ($\overline{x}$ = 51/33), with a downdip stretching lineation ($\overline{x}$ = 55/24; Fig. 2). Sense of shear is inferred from numer-
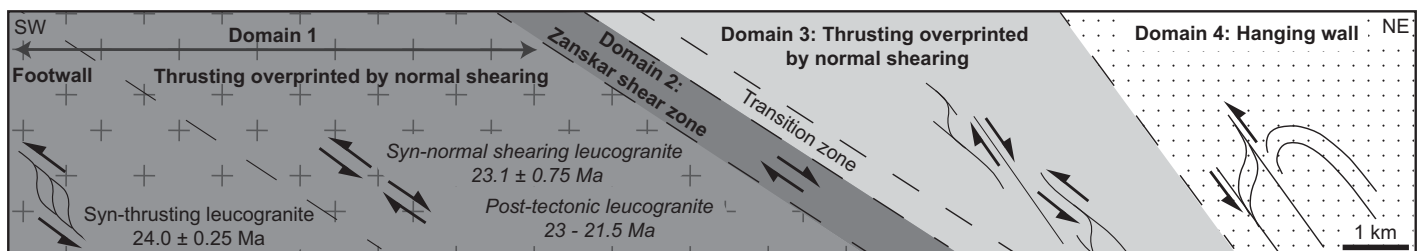
Figure 3. Schematic cross section of the Zanskar shear zone. Note transition from top-to-the-SW thrusting in the footwall (domain 1), to normal top-to-the-NE shearing in the Zanskar shear zone (domain 2a), to top-to-the-SW folding and thrusting in the hanging wall (domain 4). Transition zone between the Zanskar shear zone and hanging wall is an area where both thrusting and normal shearing are evident, but overprinting relationships are unclear. Legend is the same as in Figures 2 and 4.
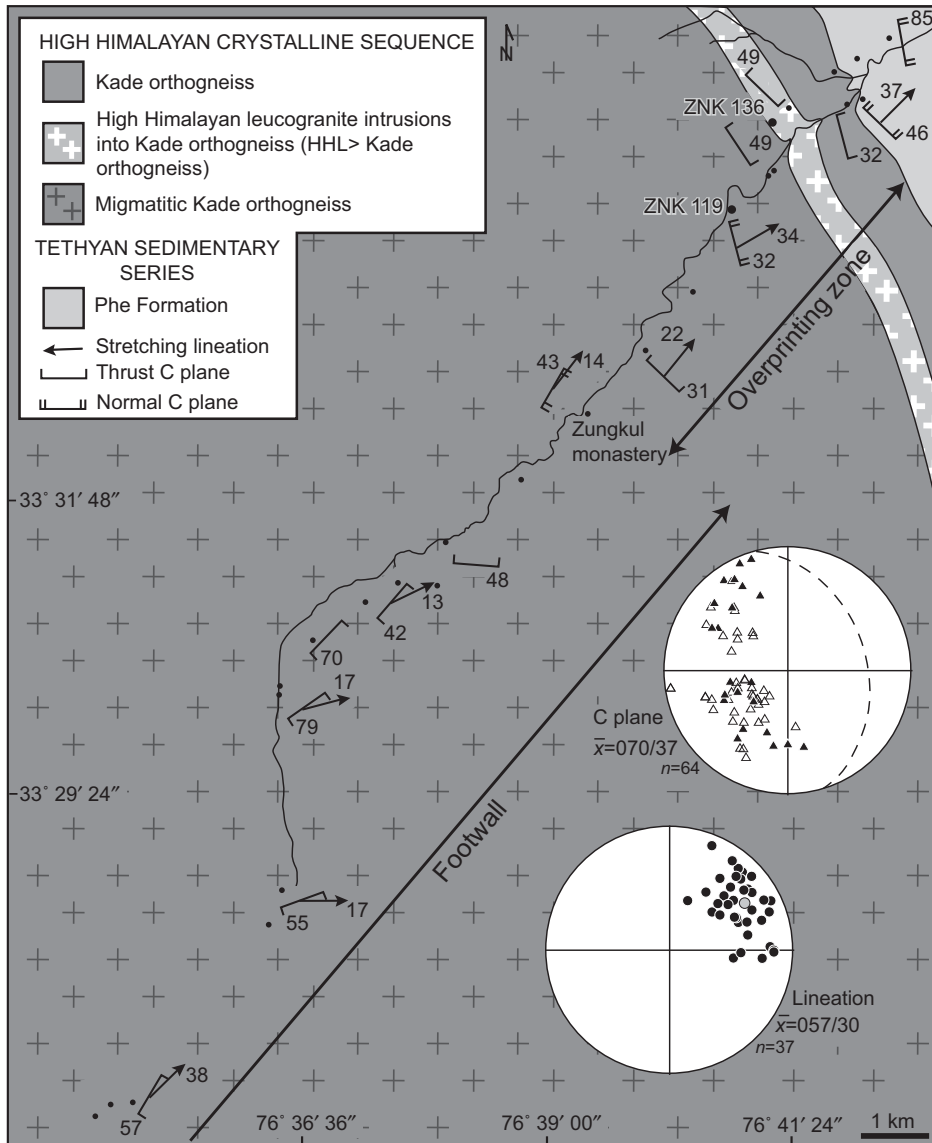
Figure 4. Geological map of domain 1. Stereographic projections of C planes related to normal shearing (black triangles) and thrusting (white triangles), and stretching lineation (circles) for each domain are shown. Projections are lower hemisphere, equal area, with the mean plane ($\bar{x}$; dashed great circle), mean lineation (gray circle), and number of measurements (n) indicated.

ous features, including S-C-C′ (Figs. 6B and 7), intrafolial asymmetric folds, deformation of leucogranitic veins forming stair-stepping structures, asymmetrically sheared dikelets (Fig. 6B), and antithetic normal faults in more competent amphibolite boudins that show clockwise bookshelf rotation (Fig. 6A). Microstructures include σ-type clasts of feldspars, mica fish, kink bands, and dynamically recrystallized quartz ribbons, which uniformly indicate ductile normal shearing (Figs. 7A–7D). At outcrop scale, strain is partitioned into narrow (generally <0.5 cm) micaceous layers parallel to the C plane and

into steeper normal NNE-dipping synthetic C′ planes ($\bar{x} = 16/49$; Figs. 6B and 7).

Mylonitic Kade orthogneiss has characteristic compositional banding with alternating mica-rich, quartz-rich, and feldspar-rich layers at millimeter to centimeter scale. Narrow micaceous layers accommodate most of the deformation, resulting in alignment of biotite and muscovite and intense C, S, and C′ planes (Fig. 7A). Muscovite grains are generally larger than biotite, forming asymmetrical mica fish (Fig. 7A).

Quartz grains (0.01–0.8 mm in size) are dynamically recrystallized (Fig. 7B), with grain

size dependent on position, i.e., generally smaller in micaceous bands (0.01–0.3 mm in size) than in quartz- and feldspar-dominated bands (0.1–0.8 mm in size). Quartz recrystallization involves both dominant grain boundary migration, as indicated by sutured grain boundaries (Figs. 7B and 7D), as well as subgrain rotation, as indicated by larger, equant grains. Activity of both recrystallization mechanisms indicates deformation temperatures of 490–530 °C (Stipp et al., 2002), but prevailing grain boundary migration supports temperatures at the higher limit of this range (Stipp et al., 2002; Passchier and Trouw, 2005; Law et al., 2011).

K-feldspar and plagioclase grains form porphyroblasts (up to 1 cm in size) that are locally flattened and show undulatory extinction (Fig. 7C), and plagioclase displays kink bands (Fig. 7D). These microstructures are indicative of ductile deformation at minimum temperatures of 450–500 °C (Fitzgerald and Stünitz, 1993; Passchier and Trouw, 2005). The larger K-feldspar and plagioclase porphyroblasts were also deformed in brittle conditions (Figs. 7C and 7D). These porphyroblasts have been fractured, and subsequently, during shearing, their lattices were distorted, and the fractured pieces were rotated, resulting in domain, domino-like, undulatory extinction and slight to high crystallographic preferred orientation (CPO) misorientation in the different fractured pieces (Fig. 7C). In extreme cases, the fractured pieces have been displaced and rotated during shearing so as to be completely disconnected. Fractures are filled with small, recrystallized K-feldspar, plagioclase, and quartz grains (Fig. 7C). Large feldspar porphyroblasts are surrounded by fine-grained matrix of K-feldspar and plagioclase grains and recrystallized quartz (Figs. 7C and 7D).

Zanskar Shear Zone: Gumburanjun Dome (Domain 2b)

The Zanskar shear zone is also exposed in the area around the Gumburanjun leucogranitic dome (Figs. 1B, 2, and 8) at the upper reaches of the Kargyak valley, defining domain 2b. This domain is bound by the first appearance of leucogranite along the valley approaching from the NE, which also coincides with the contact between the sedimentary rocks of the Phe Formation and the Kade orthogneiss (Fig. 2). Lithologically, it consists of an intrusion complex within Kade orthogneiss, immediately below the contact with the Tethyan sedimentary series, containing rare rafts of biotite-quartzite interbedded with biotite-muscovite schist. The proportion of leucogranite intrusions relative to Kade orthogneiss increases gradually from ~10% at the dome margins to 90% in the middle (Fig. 8A).

Switch from thrusting to normal shearing in the Zanskar shear zone, NW Himalaya: Implications for channel flow
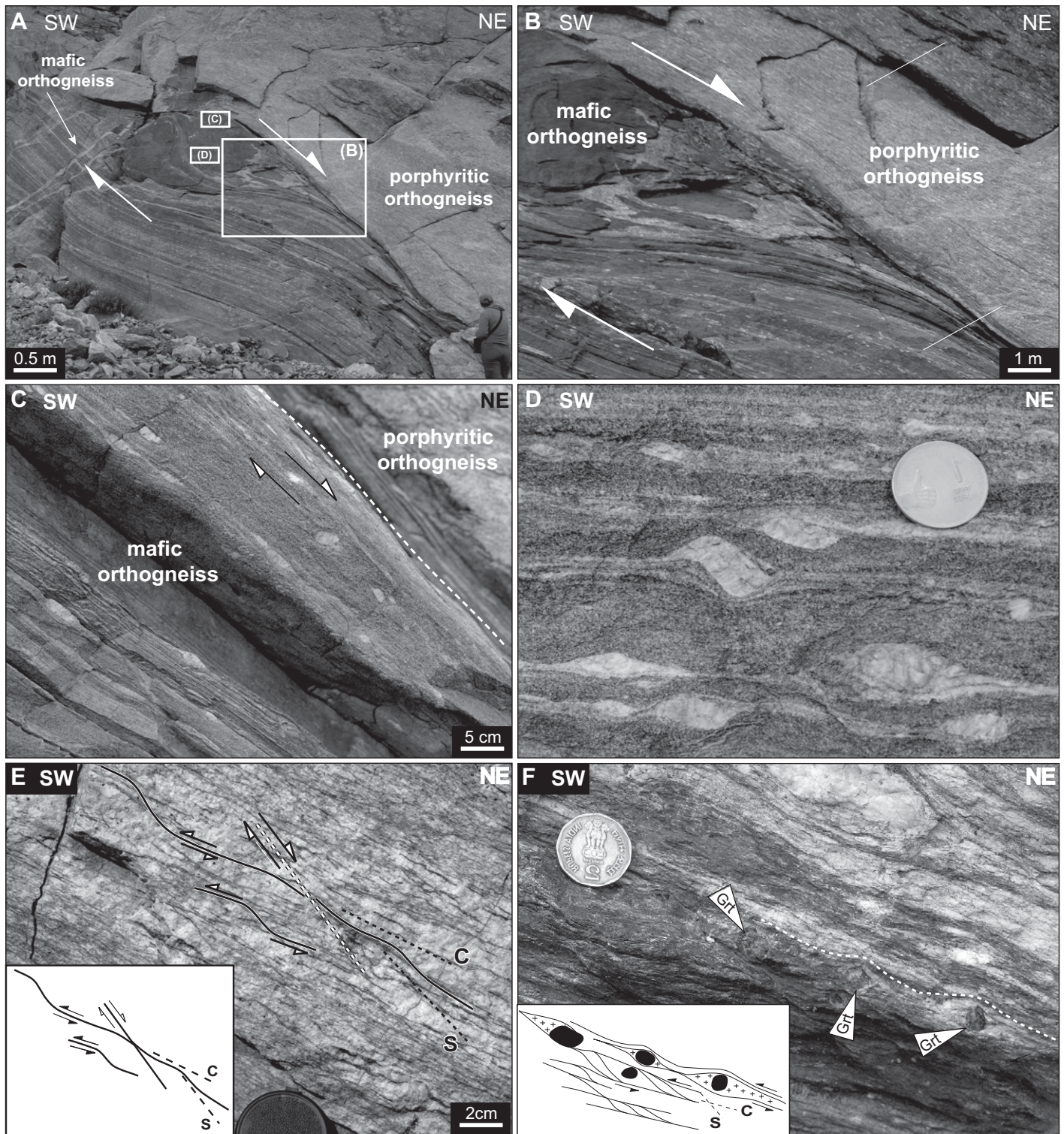
Figure 5. Characteristic structures of the Zanskar shear zone footwall in domain 1. (A) Mafic orthogneiss lithon inside porphyritic orthogneiss shows normal top-to-the-NE shearing (white arrows; locality ZNK134). Rectangles mark position of photographs in B, C, and D. (B) Detail of mafic lithon with normal shearing at its margin and in surroundings, and thrusting preserved in lithon core. (C) K-feldspar porphyroblasts in mafic orthogneiss with asymmetric tails indicative of normal top-to-the-NE normal shearing. (D) Porphyroblasts of K-feldspar with asymmetric tails indicating top-to-the-SW thrusting in the core of mafic lithon. (E) Top-to-the-SW thrusting (black lines) overprinted by normal movement (white dashed line) recorded by a Tur-Grt-Ms-Bt leucogranite (locality ZNK119). (F) Top-to-the-SW thrusting of garnet-bearing leucosome in mylonitic orthogneiss indicative of crustal anatexis before or during thrusting (locality ZNK119). Grt—garnet. Insets depict observed structures. Vertical walls in all photographs are oriented subparallel to stretching lineation.

Finch et al.

Domain 2a: Zanskar Shear Zone
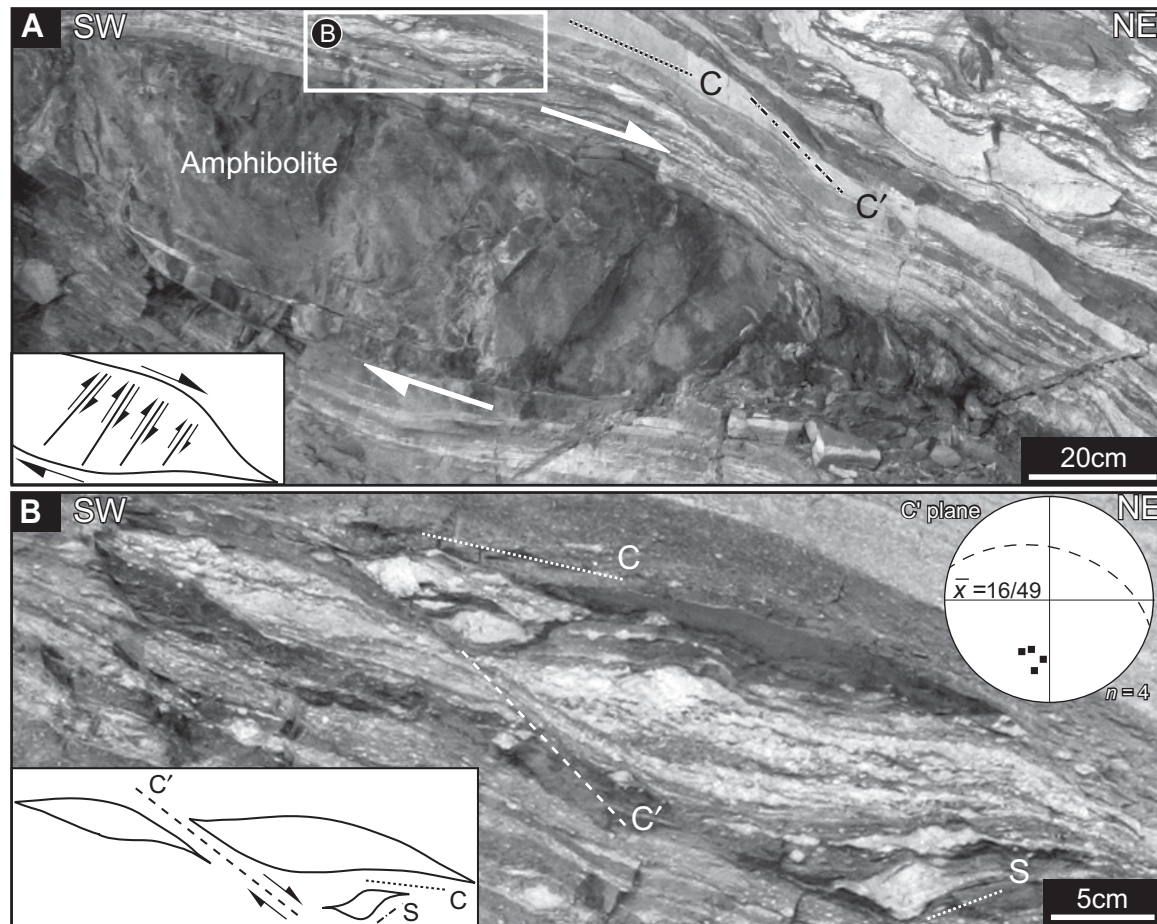
Figure 6. Characteristic structures in domain 2a indicative of ductile top-to-the-NE normal shearing (locality ZNK55). (A) Amphibolite boudin within mylonitic Kade orthogneiss and leucogranite with asymmetric features. Boudin has antithetic faults that have rotated clockwise. White rectangle shows position of B. (B) Asymmetric boudins sheared on C, S, and C′ planes. Insets depict observed structures. Photographs were taken approximately parallel to stretching lineation, perpendicular to the foliation. Stereographic projection is lower hemisphere, equal area, with the mean C′ plane ($\overline{x}$; dashed great circle) and number of measurements (n) indicated.

Crosscutting relationships and differences in mineralogy and deformation intensity indicate at least three different generations of intrusions (Fig. 8B). The earliest is a coarse-grained Ms-Grt-Tur-Bt leucogranite that was deformed during normal shearing, as interpreted from S-C fabric and asymmetrically sheared dikelets. This leucogranite was crosscut by a fine-grained, undeformed Tur-Ms leucogranite (white arrows in Fig. 8B). Finally, both of these leucogranites were crosscut by a Tur-Ms-Grt leucogranite that is dominantly fine grained but coarser in some regions, with Tur crystals centimeters long.

The foliation related to normal shearing, generally striking NE-SW, is deflected close to the contact between metasedimentary rocks and Kade orthogneiss, defining the granitic-gneissic Gumburanjun dome. In the north part of the dome, foliation dips NE ($\overline{x}$ = 63/19; Fig. 2), approximately parallel to the dominant shear planes in all other domains (Fig. 2), whereas in the south part of the dome, it dips south ($\overline{x}$ = 185/18; Fig. 2). Both sides record a top-down shear sense indicated by a downdip stretching lineation in the north ($\overline{x}$ = 50/19) and by a gently SW plunging lineation in the south ($\overline{x}$ = 242/9; Fig. 2).

North of the dome, rocks of the Tethyan sedimentary series show shear sense indicating both normal and reverse movement within the same plane, thus rendering the identification of overprinting relationships more difficult and defining a transition zone akin to that documented in domain 1. To the south of the dome, pervasive normal shearing on S-C planes (Fig. 8E) is associated with top-to-the-SW (Figs. 8C and 8E) and top-to-the-NE C′ planes (Figs. 8D and 8E), indicating normal shearing. The top-to-the-NE

C′ planes are interpreted as antithetic and part of top-to-the-SW simple shear.

In the Gumburanjun area, microstructures have been studied in mylonitic leucogranite and pelitic schist (Fig. 9) from the northern side of the dome recording thrusting and normal shearing. The mylonitic leucogranite and the pelitic schist consist of Qtz + Kfs + Pl + Bt ± Grt ± Ms ± Tur in different modal proportions.

Mylonitic leucogranite and pelitic schist samples recording thrusting have a strong foliation defined by recrystallized quartz, and feldspars, and preferred orientation of biotite and muscovite (Fig. 9). The micas define S-C-C′ fabric (Figs. 9A–9C). Quartz grains are also elongate parallel to S, C, and C′ planes, as their shape and orientation are dominantly controlled by mica distribution (Figs. 9A–9C). Quartz is

Switch from thrusting to normal shearing in the Zanskar shear zone, NW Himalaya: Implications for channel flow
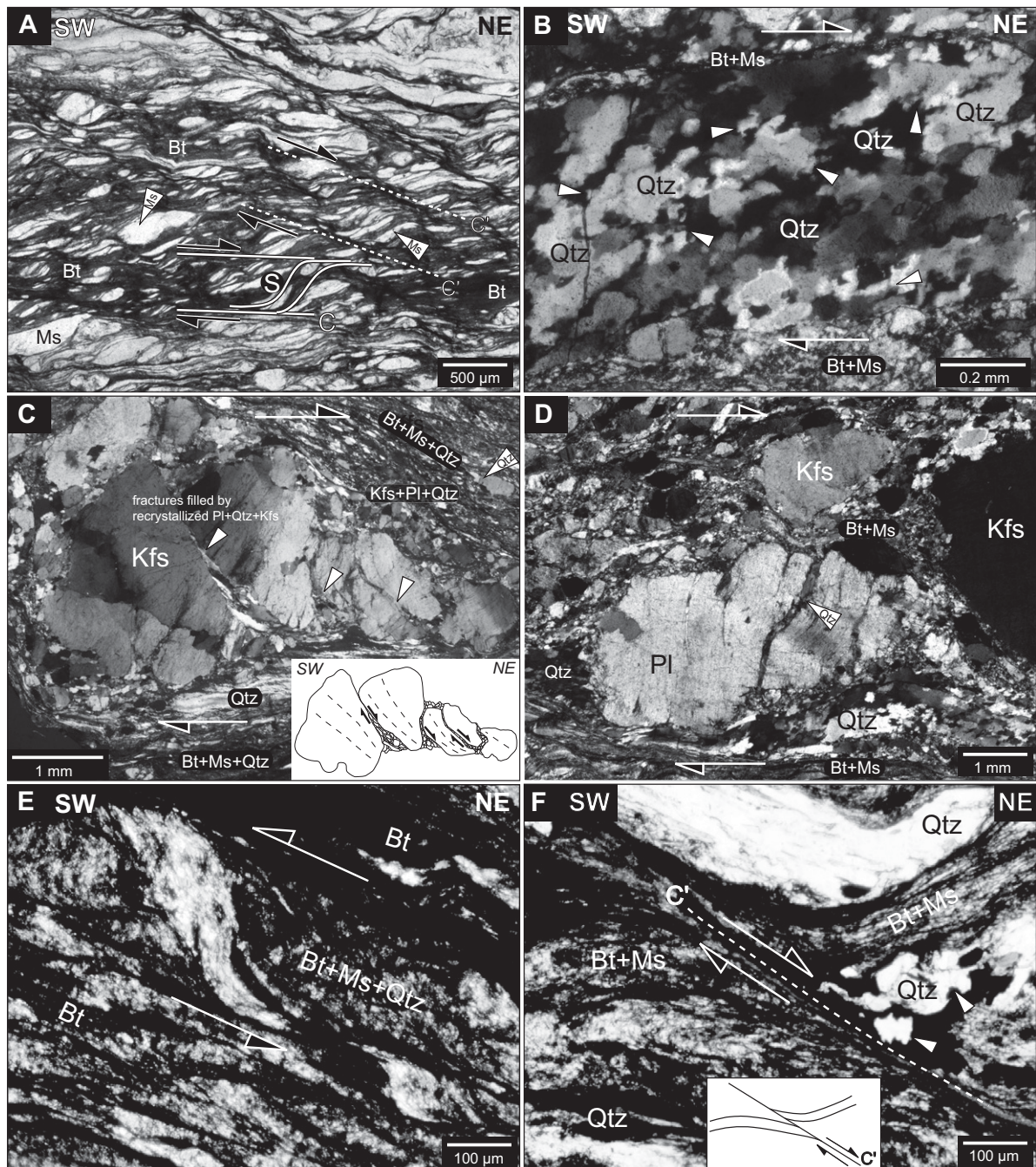
Figure 7. Photomicrographs of characteristic microstructures in domain 2 (A–D), characterized by top-to-the-NE normal shear sense (locality ZNK55), and domain 3 (E–F), where microstructures indicating both top-to-the-SW and top-to-the-NE shear senses are seen (locality ZNK72). (A) Biotite and muscovite define S, C, and C′ planes. Muscovite forms asymmetric fish. Quartz and feldspars recrystallize between micaceous layers that control their shape and orientation (sample ZNK55C4). (B) Sutured quartz grain boundaries (white arrows) indicating dynamic recrystallization by grain boundary migration. Quartz shape preferred orientation is parallel to S planes, consistent with top-to-the-NE shear sense (sample ZNK55C1). Recrystallized quartz-rich layer is surrounded by mica-rich layers. (C) K-feldspar porphyroblast faulted during shearing. Faults are filled by fine-grained recrystallized quartz–plagioclase–K-feldspar grains (white arrows), which allowed block rotation (inset; sample ZNK55C4). K-feldspar also shows undulatory extinction, suggesting crystal plasticity during deformation. (D) Kink bands in Pl porphyroblast. Both plagioclase and K-feldspar porphyroblasts show undulatory extinction and are flattened due to shearing. Quartz ribbon shows grain boundary migration recrystallization (sample ZNK55C4). (E) Sheared, recrystallized, quartz σ porphyroclasts indicating top-to-the-SW thrusting (sample ZNK72B1). (F) Synthetic shear plane (C′ plane; white dashed line) indicating top-to-the-NE normal shearing (sample ZNK72B3). Quartz displays sutured boundaries (white arrows) indicating recrystallization by grain boundary migration. Sections are perpendicular to foliation, parallel to stretching lineation. Mineral abbreviations after Kretz (1983).

Domain 2b: Gumburanjun dome
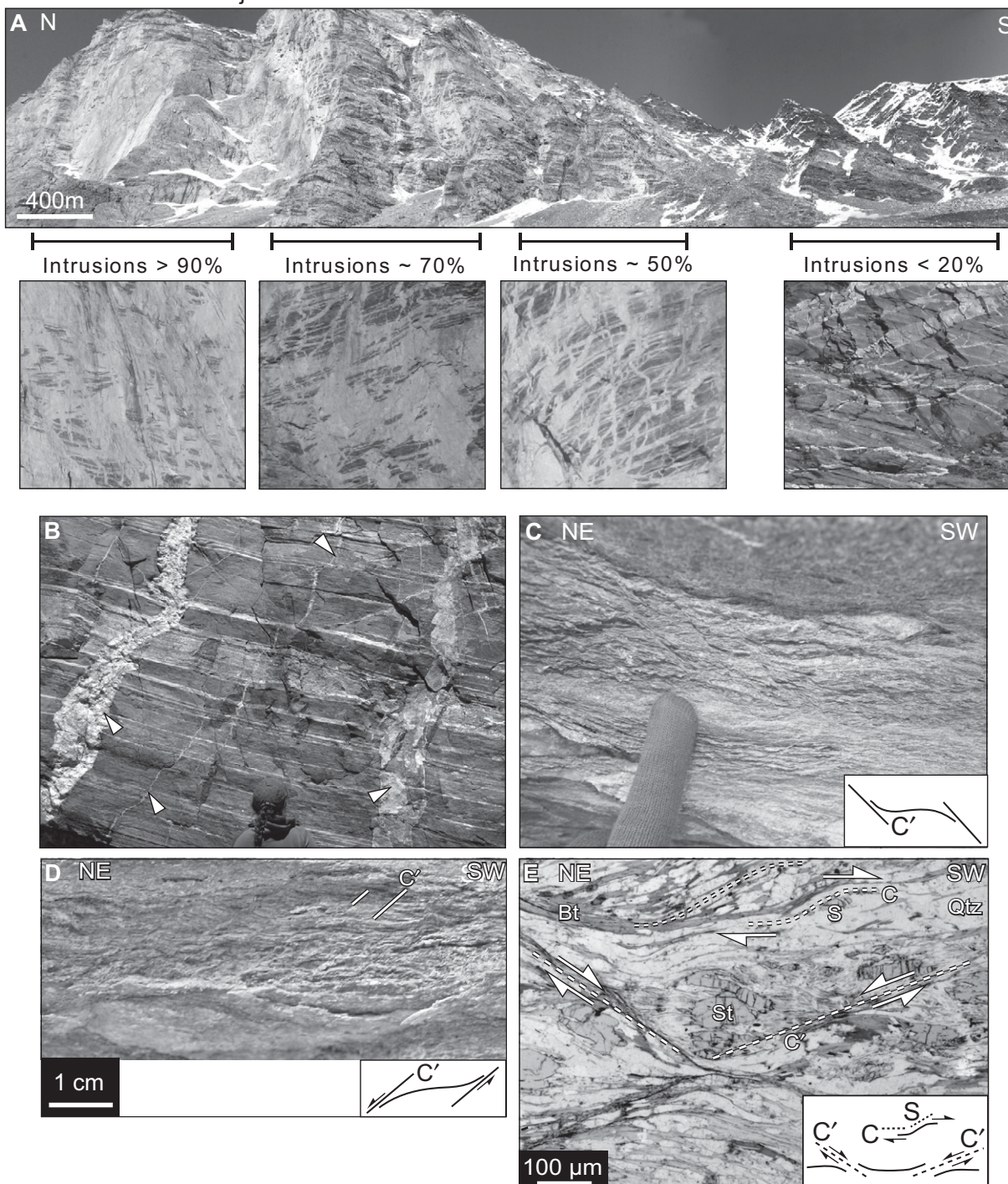
Figure 8. Characteristic structures of Gumburanjun area in domain 2b. (A) Leucogranitic injection complex in Gumburanjun dome. In center of dome, leucogranite comprises >90% of the volume, with gradual decrease to north and south. (B) Layered mylonites of Zanskar shear zone at the foot of Gumburanjun wall showing light bands corresponding to intensely sheared (Grt-Tur-Ms-Bt) leucogranites parallel to foliation, interlayered with biotite-rich mylonitic gneiss corresponding to sheared Kade orthogneiss. Layered mylonites are intruded by irregular, undeformed, post–normal shearing Tur-Ms leucogranite dikes (white arrows; viewing direction toward east). (C) C′ shear bands indicating top-to-the-SW normal shear in metapelites south of Gumburanjun. (D) Antithetic C′ shear bands within a region dominated by top-to-the-SW normal shear in metapelites south of Gumburanjun. (E) C-S shear bands in metapelite indicating top-to-the-SW normal shear C′ planes (sample ZNK107). Thin sections and photographs are parallel to stretching lineation and perpendicular to foliation. Mineral abbreviations after Kretz (1983).

completely dynamically recrystallized by grain boundary migration, as indicated by sutured boundaries between quartz grains. Bulbous myrmekites tracing K-feldspar boundaries are common and reflect deformation at high temperatures (Paterson et al., 1989; Vernon, 1991). K-feldspar and plagioclase grains are plastically deformed with undulose extinction and slightly sutured boundaries, but their shape and orientation are dominantly controlled by micas. Garnet in pelitic schist forms large sub- to euhedral porphyroblasts (up to 2 cm in size; Fig. 9). Metamorphic minerals are described in detail further in the section "Metamorphism in the Gumburanjun Area."

Microstructures and mineral assemblages in the mylonitic leucogranite and pelitic schist in domain 2 indicate a high deformation temperature of at least upper amphibolite facies (>650 °C; e.g., Toy et al., 2008; Law et al., 2011), followed by brittle deformation at low-temperature conditions. The sutured to straight grain boundaries and slightly bimodal grain size of quartz indicate dynamic recrystallization by grain boundary migration in combination with subgrain rotation. K-feldspar and plagioclase form large porphyroblasts (up to 1.5 cm in size) that were fractured during shearing and also record incipient ductile deformation, as indicated by their elongate shape and undulose extinction. Quartz, micas, and feldspars in leucogranites have the same microstructures as in the Reru area (domain 2a) and indicate lower temperatures of deformation at 490–530 °C (Stipp et al., 2002; Passchier and Trouw, 2005; Law et al., 2011).

Domain 3: Normal Shearing Overprinting Thrusting

Domain 3 is structurally above domain 2 and consists of the structurally deepest lithologies of the Tethyan sedimentary series in the region, consisting of an ~1–2-km-thick package of biotite-muscovite pelitic schists or slate and biotite-quartzites (Phe Formation; Fuchs, 1987; Herren, 1987; Dézes, 1999). These rocks preserve primary structures, including graded bedding, cross-bedding, and ripples, typically indicating upward younging.

Domain 3 marks the end of the intense and pervasive ductile normal shearing of domain 2, giving way to a region dominated by top-to-the-SW thrusting overprinted by sharp shear planes with top-to-the-NE normal shearing (Fig. 10). Thrusting is indicated by S-C fabric, σ-type clasts of quartz and mica (Fig. 7E), asymmetric folds, and well-developed crenulation cleavage. Normal shearing is indicated by asymmetric folds and normal shear planes at microscale (Fig. 7F).

Domain 3 starts 4.5 km SE of the village of Ichar and extends to ~1.5 km west of the village of Kalbok (Fig. 2). There is a narrow transition zone of complex overprinting between domains 2 and 3. This transition zone is between the village Ichar and the locality of Pipula (Fig. 2), where thrusting is accompanied by recumbent and inclined folds that verge southwest, with complex relationships between thrust and normal shear zones. Between Pipula and Kalbok (Fig. 2), the nature of the overprinting relationship becomes clear.

In this region, the overprinting of low-angle, ENE-dipping thrusts ($\bar{x} = 87/30$; Fig. 2) by high-angle, NE-dipping normal shear ($\bar{x} = 45/56$; Fig. 2) is apparent from hectometer to decimeter scale and is characterized by the dragging of bedding and thrust planes, indicating a normal sense (Fig. 10). Although the normal shear planes appear brittle in outcrops (Fig. 10), thin-section observations reveal they are sharp, narrow zones of ductile shearing (Fig. 7F). The thrust planes in these low-grade rocks are essentially parallel to those in the high-grade rocks in the footwall of the Zanskar shear zone described in domain 1 (Figs. 4 and 5). The thrust planes in domain 3 also have essentially the same orientation and similar downdip stretching lineation ($\bar{x} = 59/25$; Fig. 2) as the normal shear planes and stretching lineation in domain 2a ($\bar{x} = 55/24$; Fig. 2). This indicates that normal shearing used the preexisting thrust planes and had a similar

shear direction but opposite sense (Fig. 3). A crenulation lineation is associated with folding caused by thrusting and is at a high angle to the stretching lineation, plunging shallowly to the SSE or NW ($\bar{x} = 166/1$; Fig. 10A).

Biotite-rich schist has a strongly developed foliation defined by alignment of biotite and muscovite grains (Figs. 7E and 7F). Quartz (0.05–0.2 mm in size) is dynamically recrystallized by grain boundary migration, as indicated by lobate grain boundaries (Fig. 7F), with shape and grain size controlled by mica distribution. Plagioclase and K-feldspar grains are small (up to 0.4 mm) and have only incipient recrystallization.

Domain 4: Fold-and-Thrust Belt

Domain 4 is the hanging wall further removed from the Zanskar shear zone and is structurally the highest domain (Fig. 3). This domain is characterized by large-scale folding and thrusting (Figs. 3 and 11), lacking the significant normal shear overprint characteristic of domain 3. From SW to NE, this domain begins within the Phe Formation and grades into the overlying Lower to Middle Cambrian Karsha Formation, marked by the first appearance of thick dolomite beds (Dézes, 1999) close to the village Karu (Fig. 2). This domain was investigated along the valley and continues into the ranges northeastwards.

Figure 9 (*on following page*). **Photomicrographs and backscattered electron (BSE) image of metamorphic assemblages and textures in pelitic schist, Gumburanjun area, domain 2. (A) Garnet porphyroblasts in garnet zone with straight inclusion trails of quartz + plagioclase + ilmenite (dashed white line) discontinuous with external foliation. External foliation is marked by elongation of biotite (white solid line). Matrix is formed by recrystallized quartz + plagioclase + K-feldspar grains (sample ZNK106). (B) Garnet porphyroblast in garnet zone from same thin section as A with curved inclusion trails of quartz + plagioclase + ilmenite that link continuously with external foliation (dashed white line). Asymmetry indicates top-to-the-S normal shear. (C) Staurolite porphyroblasts from staurolite zone varying from euhedral to strongly anhedral and irregular shapes suggestive of corrosion. Staurolite is oriented parallel to main foliation and contains inclusion trails of quartz + ilmenite + garnet continuous with external foliation, parallel to either S or C planes. External foliation wraps around staurolite, producing asymmetric strain shadows. C′ plane is emphasized by black dashed line (sample ZNK107). C-C′-S shear bands indicate top-to-the-S normal shear. (D) Staurolite porphyroblast from staurolite zone with inclusion trails of quartz + plagioclase + garnet parallel to C′ plane but discontinuous with external S-C foliations (sample ZNK107). C-C′-S shear bands indicate top-to-the-S normal shear. (E) Brittle deformation of staurolite porphyroblast from staurolite zone. Staurolite is fractured, with fractures at high angle to external foliation and filled by retrograde chlorite. Foliation is emphasized by white dashed line (sample ZNK107). Chl—chlorite. (F) Mineral assemblage of kyanite + garnet + staurolite in kyanite zone. Kyanite porphyroblasts are elongated parallel to external foliation with fractures at high angle to foliation filled by muscovite. Foliation is defined by biotite + muscovite alignment (white line; sample ZNK108). (G) Schematic summary depicting deformation and metamorphic history recorded in this sequence of metapelitic rocks. Mineral abbreviations after Kretz (1983).**
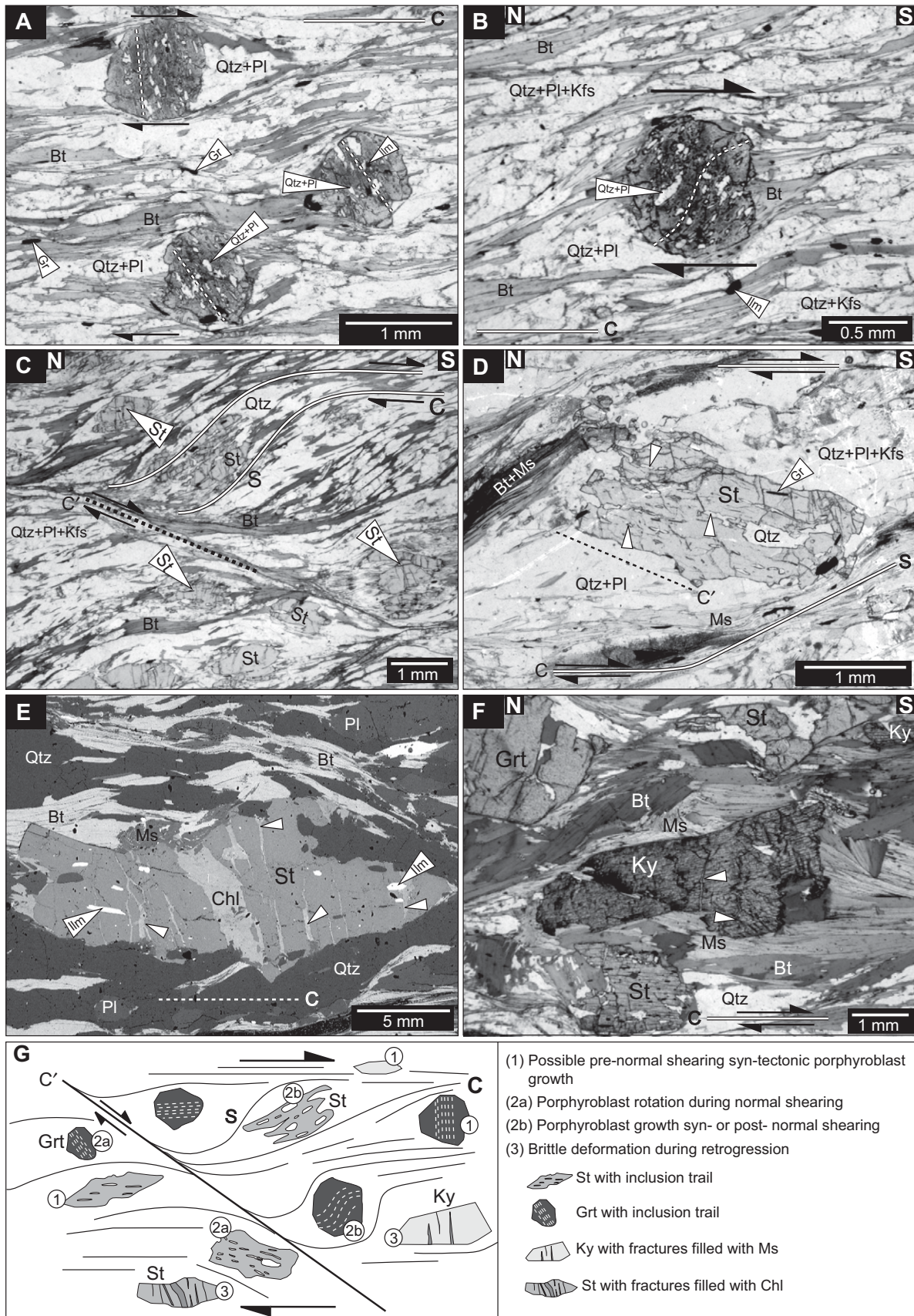
Figure 9.

Domain 3: Normal shearing overprinting thrusting
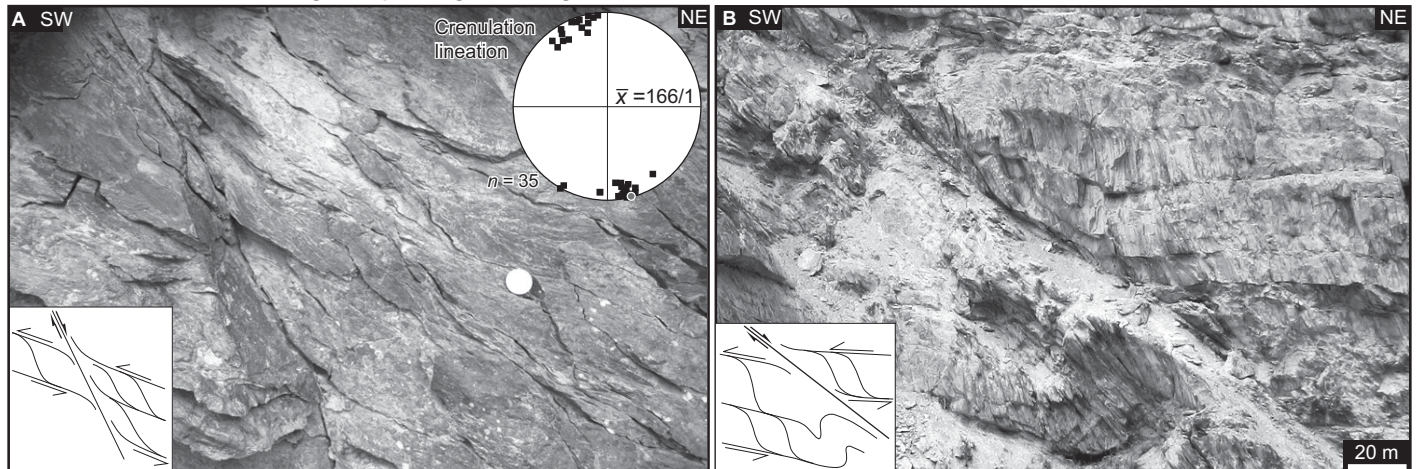
Figure 10. Characteristic structures of domain 3 (SE of Pipula). Sharp normal shear planes overprint thrust planes at (A) decimeter scale (coin diameter is 22 mm) and (B) at large scale. Inset is line drawing interpretation of the photograph. The crenulation lineation (inset in A) is perpendicular to the stretching lineation shown in Figure 2. Photographs are taken approximately parallel to stretching lineation and perpendicular to foliation plane. Stereographic projection is lower hemisphere, equal area, with the mean lineation ($\bar{x}$) and number of measurements (n) indicated.

Thrusting is associated with inclined to recumbent folds with intensely developed axial planar foliation (Fig. 11). Folds vary from hectometric to decimetric in scale (Fig. 11). The thrust plane dips moderately to steeply NE ($\bar{x}$ = 64/53), with a top-to-the-SW sense of shear and a stretching lineation more northerly than the dip direction ($\bar{x}$ = 37/43; Fig. 2). The thrust plane in domain 4 is slightly steeper than that in domain 3 and the normal shear plane in domain 2 (Figs. 2 and 3). The folds are tight to isoclinal, with axial planes parallel to the thrust plane or fanning away from the thrust plane (Fig. 3).

Fold hinges are at a high angle to the stretching lineation (defined by alignment of muscovite) and parallel to the crenulation lineation, plunging shallowly to the south ($\bar{x}$ = 160/17; Fig. 11).

QUARTZ FABRIC

In order to understand different quartz deformation styles and constrain deformation temperatures in the domains at different structural levels, we measured c-axis orientation of quartz in leucogranites and pelitic schists deformed in normal and/or reverse shearing (Fig. 12). Quartz

c-axis fabrics were determined using the Fabric Analyzer G50 at Monash University, Australia (for details see Wilson et al., 2003, 2007). Based on a stack of photomicrographs, an axial distribution image (Sander, 1950) is generated with a spatial resolution of 5 µm/pixel and 3 µm/pixel, and the c-axis orientation of each pixel is then evaluated using the INVESTIGATOR software (Peternell et al., 2010). C-axis orientations were collected automatically in a regular grid, but rather than evaluating every pixel, we manually chose one spot for each subgrain/grain. Thus, each individual grain/subgrain is represented by
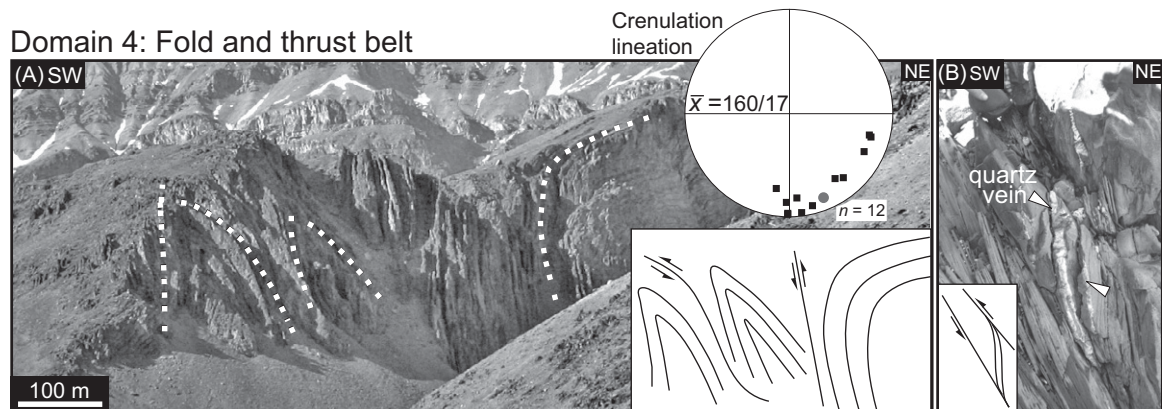
Figure 11. Characteristic structures of domain 4. (A) Folding and thrusting at large scale. (B) Thrusting in narrow pelitic layers in biotite-quartzite interbedded with biotite-muscovite schist, indicated by foliation and sheared quartz veins (white arrows). Photographs are taken approximately parallel to stretching lineation and perpendicular to foliation plane. The fold axis is parallel to the crenulation lineation (inset). Stereographic projection is lower hemisphere, equal area, with the mean lineation ($\bar{x}$) and number of measurements (n) indicated.
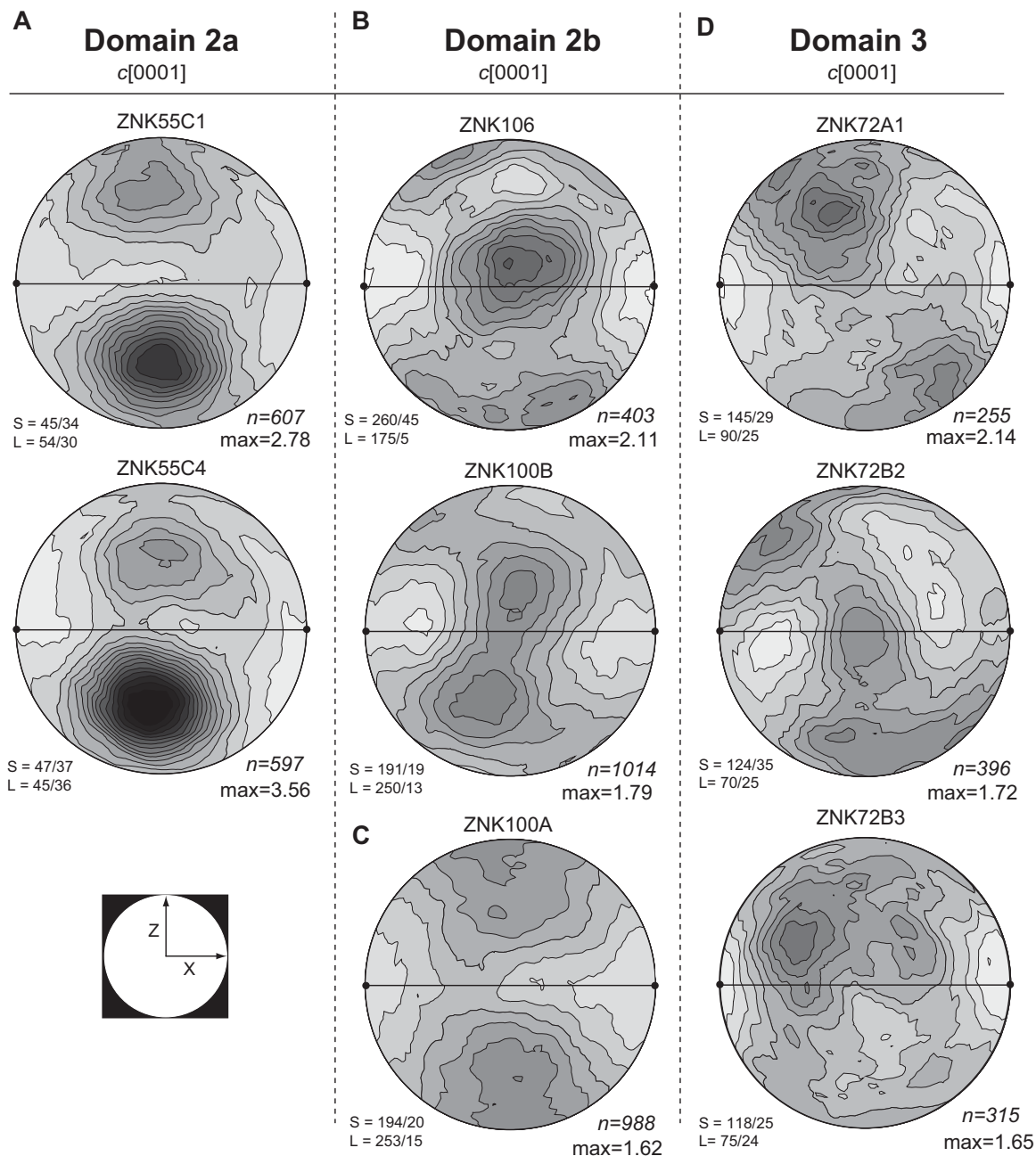
Figure 12. Lower-hemisphere, equal-area stereographic projections of quartz *c*-axis preferred orientations measured using the Fabric Analyzer. (A) Two mylonitic Kade orthogneiss samples (samples from locality ZNK55C, Fig. 4) deformed during ductile normal shearing (Reru area, domain 2a) reveal pure shear deformation and strong maxima indicating activity of rhomb <a> with minor basal <a> slip systems. (B) Quartz in muscovite (Ms) + biotite (Bt) + garnet (Grt) schist (sample ZNK106) and Kade orthogneiss (sample ZNK100B), both deformed by ductile thrusting (transition zone between domain 2b and domain 3). Sample ZNK100B defines type I cross girdle with maxima indicating combination of rhomb <a>, prism <a>, and basal <a> slip systems. Sample ZNK106 defines type II cross girdle. (C) Leucogranite deformed by normal shearing in domain 2b (sample ZNK100A) showing basal <a> slip system in combination with minor rhomb <a> slip system. (D) Pelitic schists of domain 3 (samples from locality ZNK72, Fig. 10), where normal shearing overprints thrusting, showing noncoaxial deformation and weak rhomb <a> slip system in combination with weak basal <a> slip system, indicative of upper-greenschist to lower-amphibolite facies conditions. Stereonets are contoured at interval of 0.2 times uniform distribution. Trace of foliation determined in the field is represented by horizontal black solid lines, stretching lineation is represented by dot on this line, *n* is number of quartz analyses in each sample, and maximum density values are indicated. S values are dip direction/dip of foliation, and stretching lineation (L) values are plunge direction/plunge.

only one orientation measurement. Fabrics were plotted and contoured using StereoNett 2.46 software and are displayed on lower-hemisphere equal-area projections in which the projection plane is oriented perpendicular to foliation and parallel to stretching lineation (Fig. 12).

In samples studied, quartz has distinct CPO patterns and fabric intensities for rocks deformed in thrusting and normal shearing. In domain 2a, we investigated two mylonitic orthogneiss samples (Fig. 12A) that were deformed during ductile normal shearing. Quartz grains define strong c-axis maxima (max. density = 3.57 in ZNK55C4 and 2.78 in ZNK55C1; Fig. 12A), indicating activity of rhomb <a> and minor basal <a> slip systems (Fig. 12A). Activation of these slip systems indicates deformation at upper-greenschist- to lower-amphibolite facies conditions (~500–600 °C; e.g., Schmid and Casey, 1986; Passchier and Trouw, 2005; Toy et al., 2008).

From the Gumburanjun area (domain 2b), we studied samples of mylonitic leucogranite (sample ZNK100B) and garnet-bearing schist (sample ZNK106), both deformed during thrusting (Fig. 12B). C-axis preferred orientations reveal asymmetric type I cross girdle (sample ZNK100B) or a slightly asymmetric type II cross girdle (sample ZNK106) with an opening angle of 90°–95° indicative of noncoaxial deformation. Clear maxima indicate activity of the rhomb <a+c> slip system in combination with weak basal <a> and prism <a> slip systems (max. density = 1.79–2.11; Fig. 12B) characteristic of high temperatures in upper-amphibolite facies (~650–700 °C; e.g., Kruhl, 1998; Toy et al., 2008; Law et al., 2011). In contrast, a sample of leucogranite (ZNK 100A) deformed during normal shearing (Fig. 12C) shows an incomplete single girdle, and maxima indicating activity of the basal <a> slip system in combination with minor activity on the rhomb <a> slip system (max. density = 1.62; Fig. 12C). This reflects upper-greenschist facies (~500 °C; e.g., Schmid and Casey, 1986; Passchier and Trouw, 2005; Toy et al., 2008).

Three low-grade pelitic schist samples from domain 3 were analyzed and record the overprinting relationship of normal shearing on thrusting (Fig. 12D). The c-axis orientation of quartz shows a broad asymmetric single girdle and clear maxima indicative of basal <a> in combination with the rhomb <a> slip system (max. density = 1.65–2.14; Fig. 12D), characteristic of upper-greenschist to lower-amphibolite facies (e.g., Schmid and Casey, 1986; Toy et al., 2008). Shear fabric asymmetry indicates dominant noncoaxial deformation.

In summary, leucogranites from within the Zanskar shear zone in domain 2 deformed during normal shearing and record deformation temperatures of upper-greenschist to lower-amphibolite facies (Figs. 12A and 12C). This contrasts with the mylonitic leucogranite and schist from domain 2, deformed during thrusting, which record higher deformation temperatures of upper-amphibolite facies (Fig. 12B). Quartz CPOs in pelitic schist samples from domain 3 (Fig. 12D), which record overprinting relationships between normal and reverse shearing, show similar or weaker fabric than rocks in domain 2 at similar temperatures. Active slip systems show a combination of lower-temperature basal <a> and rhomb <a> slip systems in domain 2 during normal shearing, and rhomb <a+c> and prism <a> slip systems in domain 2 during thrusting. Interestingly, domain 3 reveals a combination of all these slip systems, suggesting that quartz here partially preserves fabric developed during early thrusting, but this fabric weakened and was overprinted by fabric developed during normal shearing.

SUMMARY OF DEFORMATION STYLE OF THE ZANSKAR SHEAR ZONE

The footwall (domain 1) is characterized by normal shearing overprinting thrusting with the same geometry (Fig. 5). Both events are recorded by both the migmatitic orthogneisses and leucogranite sills. The Zanskar shear zone in domain 2 in the Reru area is characterized by ductile normal top-down-to-the-NE shearing (Fig. 6) at upper-greenschist- to amphibolite-facies conditions, as indicated by microstructures, quartz CPO, and mineralogy, with strain mostly localized into micaceous bands (Figs. 7A–7D and 12A). Domain 2 in the Gumburanjun area is characterized by normal shearing of Kade orthogneiss intensely intruded by leucogranites, which coalesce to form a region consisting of greater than 90% leucogranite intrusions, forming the Gumburanjun dome (Fig. 8). Normal shear zones at both the northern and southern margins indicate that the dome was a result of normal movement. Quartz CPO indicates deformation of mylonitic leucogranite at upper-amphibolite facies conditions (~650–700 °C; Fig. 12B) during thrusting, while other leucogranites record normal shearing at upper-greenschist to lower-amphibolite conditions (~500–600 °C; Fig. 12C). The transitions between normal shearing and thrusting in the hanging wall and footwall are also recorded by quartz CPO. The end of the transition zone and start of domain 3 are marked by narrow normal shear zones that overprint pervasive ductile thrusting (Figs. 3 and 10). Here, strain partitioned mostly into micaceous layers and quartz CPO indicates upper-greenschist to lower-amphibolite conditions during deformation (~500–600 °C; Figs. 7E and 12D). Further into domain 3 and structurally upward, abundant chloritization of biotite and absence of high-grade minerals (or their retrograde equivalents) indicate a decrease in metamorphic grade to greenschist facies (~450–500 °C). Domain 4 records folding and thrusting with only local evidence of normal overprint (Figs. 3 and 11).

Generally, the attitude of the shear planes (C planes) in high-grade rocks in domains 1 and 2, whether normal or thrust, are essentially the same, dipping ~35°NE, and the attitudes of stretching lineations are also the same, down-dip in both cases (Figs. 2 and 4). This indicates that the normal shear zone reactivated preexisting thrust C planes and that the switch between the two was a reversal of the transport direction from top-to-the-SW thrusting to top-to-the-NE normal movement. Brittle-ductile, narrow, normal shear on steep, NE-dipping planes overprints both generations of ductile movement, indicating a late stage of normal shear.

U-Pb MONAZITE GEOCHRONOLOGY

In order to constrain the maximum duration of the normal shearing event in eastern Zanskar, and the timing of the switch from thrusting to normal shearing and related anatexis, we dated (U-Pb monazite sensitive high-resolution ion microprobe [SHRIMP] dating) leucogranites from domains 1 and 2. We collected two leucogranites (samples ZNK136 and ZNK119) sheared by thrusting. We also sampled a leucogranite that is strongly sheared by the normal shear zone (sample ZNK103A), which could either predate or be contemporaneous with normal shearing, and a late leucogranite (sample ZNK17E) that crosscuts sheared rocks, is undeformed and is assumed to postdate normal shearing.

Methodology

Each sample was crushed and milled, and monazite grains were separated and mounted in epoxy resin together with monazite 44069 standard (425 ± 1 Ma; Aleinikoff et al., 2006). The final mount was polished, and prior to analysis, all monazite grains were photographed in transmitted and reflected light, as well as imaged by backscattered electrons (BSE) on the scanning electron microscope. This allowed identification of pristine areas for analysis and determination of whether multiple age components (e.g., cores and overgrowths) were present. Monazites were dated using the SHRIMP II at the Research School of Earth Sciences at the Australian National University (ANU). The analytical procedure for mona-

zite dating followed methods described in Williams et al. (1996). The SHRIMP raw data were reduced with the SQUID 2 Excel macro of Ludwig (2001; http://sourceforge.net/projects/squid2/files). Isotopic age data for the four samples are given in Tables 1 and 2 and Figures 13 and 14; uncertainties given for individual analysis (ratios and ages) are at the 1σ level. Probability density plots, weighted mean $^{206}Pb/^{238}U$ ages, and Tera-Wasserburg (Tera and Wasserburg, 1972) concordia plots were calculated using Isoplot (Ludwig, 2003). Error ellipses in the Tera-Wasserburg diagrams and error bars in weighted average diagrams are plotted at 2σ.

Results

ZNK136 and ZNK119: Leucogranites Related to Thrusting

These two samples are from Malung Thokpo valley in domain 1 (ZNK119: 33°34′00.5″N, 76°40′46.0″E; ZNK136: 33°34′41.9″N, 76°41′10.6″E; Fig. 4). Sample ZNK 136 is a porphyritic Bt-Grt-Ms leucogranite sheared during thrusting, whereas sample ZNK 119 is a garnet-bearing leucosome formed in mylonitic orthogneiss during thrusting and is intensely sheared.

ZNK136 leucogranite. Monazite grains are rounded to irregular in shape, corroded, and fairly uniform in size (100–200 μm; Fig. 13A). They contain large apatite and xenotime inclusions and in BSE show patchy zoning of Y and Th (e.g., grains 6 and 11 in Fig. 13A), concentric zoning (e.g., grains 3, 4, 7, and 8 in Fig. 13A), or are homogeneous with narrow rims (e.g., grains 2 and 10 in Fig. 13A). Monazite grains have high U concentrations (3000–9000 ppm; Table 1), which are common for Himalayan leucogranite monazite (e.g., Walker et al., 1999). Twenty-one spots on 15 mounted monazite grains were analyzed. All analyses are slightly normally discordant (Fig. 13B) and yield single $^{206}Pb/^{238}U$ ages between ca. 26 and 21 Ma (Fig. 13C–13D; Table 1). The $^{206}Pb/^{238}U$ ages were individually projected onto the concordia. The weighted mean $^{206}Pb/^{238}U$ age for all analyses is 23.8 ± 1.2 Ma (mean square of weighted deviates [MSWD] = 11.5, $n = 21$; Fig. 13C). The MSWD suggests excess scatter, and the probability density plot shows one broad peak including all data. If the outliers on either side of the dominant age population are removed, the weighted mean age is 24.0 ± 0.25 Ma, with a better MSWD of 1.2 (Fig. 13C). Most monazite grains are zoned, but the spread of ages does not correlate with distinct positions in grains (Fig. 13A): rims show ages similar to the cores. Therefore, we interpret the whole range as crystallization ages of the leucogranite during thrusting (Fig. 13A; Table 1).

ZNK119 leucogranite. Monazite grains in this sample are euhedral to round in shape, with some grains showing irregular, corroded shapes (Fig. 13E). They are large, fairly uniform in size (100–200 μm), and all grains contain high amounts of apatite inclusions, with minor xenotime and zircon inclusions (Fig. 13E). Internal zoning of the grains (visible in BSE) is quite complex, with concentric zoning (e.g., grains 2, 11, 15, and 19 in Fig. 13E), patchy zoning (e.g., grains 7, 16, and 18 in Fig. 13E), or clear oscillatory growth zoning (e.g., grains 3 and 12 in Fig. 13E). A few grains are homogeneous with narrow rims (e.g., grains 8 and 14 in Fig. 13E). Forty-two spots on 22 mounted monazite grains were analyzed, and results yield slightly reverse discordant isotope ratios (disc. = 1–14%), and a few analyses are slightly normally discordant (Table 1). Of the 42 analyses, 11 were more than 15% discordant (disc. = 15–70%) and were not included in age calculations.

Reverse discordance is a common feature of U-Pb monazite data and is thought to indicate ^{230}Th disequilibrium (Schärer, 1984; Parrish, 1990; Hawkins and Bowring, 1997). However, reverse discordance is rarely observed in SHRIMP monazite data, and additionally we do not observe any correlation between the degree of discordance and either the concentration of Th or Th/U (Table 1). The reverse discordance can also result from high U concentrations (1500–9200 ppm, Ø = 4200 ppm; Table 1) in the studied monazites (e.g., Stern and Berman, 2000). High-U areas, when analyzed by SHRIMP, usually give anomalously old $^{206}Pb/^{238}U$ ratios or ages, because Pb is preferentially sputtered, and the high U does not match the U of the reference monazite (2500 ppm) used to calibrate the U/Pb ratios (Stern and Berman, 2000; Williams and Hergt, 2000). We are unable to tell whether the reverse discordance is a result of ^{206}Pb excess due to ^{230}Th disequilibrium in monazite, or due to preferential Pb sputtering. As a consequence, we regard the calculated $^{207}Pb/^{206}Pb$ ages as the most reliable estimates of the crystallization ages of these monazites and use these for further discussion (e.g., Cheney et al., 2004). The analyses yield $^{207}Pb/^{206}Pb$ single corrected ages ranging between ca. 360 Ma and 460 Ma (Fig. 13F; Table 1) with a weighted mean $^{207}Pb/^{206}Pb$ age of 427.1 ± 7.6 Ma (2σ, MSWD = 0.96, $n = 29$; Figs. 13G and 13H). Although most of the monazite grains show clear zoning, there is no significant age difference between core and rims or different zones (Fig. 13E). Some monazite grains (e.g., grains 2 and 6) even have slightly younger cores than rims, which suggest replacement or resorption of original monazite, as indicated by the cuspate embayment boundaries between mona-

zite zones (Zhu and O'Nions, 1999). However, in this case, the age difference is within the 2σ uncertainty (note 1σ in Fig. 13E).

These analyses are interpreted to represent either old detrital monazite or monazite from pre-Himalayan granites. Given the probable Precambrian–Cambrian age of the sedimentary protolith of the High Himalayan Crystalline sequence (e.g., Steck et al., 1993; Walker et al., 1999), it seems unlikely that these monazites are detrital. Moreover, the sample was collected from within the Kade orthogneiss (Pognante and Lombardo, 1989; Pognante, 1992), which ranges in age between ca. 500 Ma and 400 Ma (Ordovician–Devonian; Pognante et al., 1990; Noble and Searle, 1995; Walker et al., 1999; Horton, 2011). Therefore, we interpret these ages as representing the crystallization ages of the Kade orthogneiss. Interestingly, this sample does not have any Miocene ages, in contrast to sample ZNK136.

ZNK103A: Leucogranite Related to Normal Shearing

Sample ZNK103A is from domain 2b, close to the Gumburanjun dome immediately below the Tethyan sedimentary series (ZNK103: 32°56′50.06″N, 77°14′57.25″E; Fig. 1). This sample is from a Ms-Grt-Tur-Bt leucogranite dike parallel to the main foliation of the Zanskar shear zone, and it is strongly overprinted by normal shearing. Monazite grains are euhedral to rounded in shape and fairly uniform in size (100–200 μm; Fig. 14A). They contain apatite, xenotime, and zircon inclusions and have internal zoning in BSE (Fig. 14A) varying from patchy (e.g., grains 2 and 10 in Fig. 14A) to concentric zoning (e.g., grains 1, 3, 4, 5, 8, and 13 in Fig. 14A) or are homogeneous with narrow rims. In some grains, these narrow rims overgrow corroded monazite grains, resulting in euhedral monazite grains with a patchy core (e.g., grain 10 in Fig. 14A). The monazite grains have high U concentrations (1900–14,000 ppm, Ø = 6500 ppm; Table 2). Twenty-five spots on 13 monazites were analyzed. They define three major $^{206}Pb/^{238}U$ age groups: (1) Cambrian–Ordovician (ca. 494–453 Ma), (2) Eocene–Oligocene (ca. 37–29 Ma), and (3) Oligocene–Miocene (ca. 26–21 Ma).

Four monazite cores yielded older concordant $^{206}Pb/^{238}U$ ages between 494 Ma and 453 Ma (Fig. 14B; Table 2), defining a weighted mean $^{206}Pb/^{238}U$ age of 470 ± 29 Ma (2σ, MSWD = 14). These ages are consistent with the ages for the Kade orthogneiss, as for sample ZNK119 (Fig. 13E–H; Table 1). One monazite core (ZNK103A-12.2) is highly discordant and reveals a singular age of 240 ± 5 Ma (Table 2). Horton (2011) and Noble et al. (2001) reported such Permian–Triassic U-Pb

Switch from thrusting to normal shearing in the Zanskar shear zone, NW Himalaya: Implications for channel flow

TABLE 1. SUMMARY OF SENSITIVE HIGH-RESOLUTION ION MICROPROBE (SHRIMP) U-Pb RESULTS FOR MONAZITE FROM SAMPLES ZNK136 AND ZNK119

Grain spot	Position	U (ppm)	Th (ppm)	Th/U	206Pb* (ppm)	204Pb/206Pb	f206 %	Total ratios 238U/206Pb	±	207Pb/206Pb	±	Radiogenic ratios 206Pb/238U	±	207Pb/235U	±	207Pb/206Pb	±	σ	Age (Ma) 206Pb/238U	±	207Pb/206Pb	±	% disc.
Sample ZNK119 (leucogranite related to thrusting)																							
1.1	Core	3122	41,013	13.14	207	0.000111	0.07	12.966	0.196	0.0573	0.0002	0.0770	0.0012	0.5904	0.0097	0.0556	0.0004	0.923	478	7	438	14	–9
1.2	Rim	5019	36,565	7.29	329	0.000040	–0.07	13.114	0.211	0.0560	0.0004	0.0762	0.0012	0.5824	0.0101	0.0554	0.0004	0.924	473	7	430	15	–10
1.3	Rim	7609	42,601	5.60	461	0.000038	0.05	14.186	0.211	0.0561	0.0001	0.0704	0.0010	0.5392	0.0082	0.0555	0.0002	0.983	439	6	433	6	–1
2.1	Rim	4050	41,166	10.16	266	0.000071	0.07	13.081	0.211	0.0571	0.0002	0.0763	0.0012	0.5907	0.0098	0.0561	0.0002	0.971	474	7	457	7	–4
2.2	Core	2014	27,886	13.85	133	0.000083	–0.03	13.029	0.196	0.0563	0.0002	0.0766	0.0012	0.5826	0.0093	0.0551	0.0003	0.949	476	7	418	11	–14
3.1	Core	5277	45,794	8.68	341	0.000046	–0.02	13.313	0.211	0.0562	0.0002	0.0751	0.0012	0.5748	0.0093	0.0555	0.0002	0.977	467	7	434	8	–7
3.2	Rim	2355	31,930	13.56	151	0.000084	0.02	13.374	0.219	0.0564	0.0002	0.0747	0.0012	0.5685	0.0097	0.0552	0.0003	0.963	464	7	421	10	–10
4.1	Rim	9205	41,749	4.54	617	0.000026	–0.16	12.843	0.189	0.0555	0.0004	0.0778	0.0011	0.5919	0.0095	0.0552	0.0004	0.916	483	7	419	14	–15
4.2	Rim	3288	33,268	10.12	204	0.000073	0.03	13.853	0.221	0.0562	0.0002	0.0721	0.0012	0.5479	0.0090	0.0551	0.0002	0.974	449	7	417	8	–8
5.1	Core	2751	35,208	12.80	185	0.000113	0.02	12.790	0.305	0.0570	0.0003	0.0780	0.0019	0.5957	0.0148	0.0554	0.0004	0.957	484	11	427	16	–13
6.1	Rim	4871	37,311	7.66	323	0.000061	–0.04	12.946	0.204	0.0563	0.0001	0.0772	0.0012	0.5899	0.0095	0.0555	0.0002	0.977	479	7	430	8	–11
6.2	Patchy	1488	28,429	19.10	94	0.000145	0.12	13.616	0.235	0.0571	0.0002	0.0732	0.0013	0.5550	0.0102	0.0550	0.0003	0.939	456	8	410	14	–11
6.3	Patchy	2493	25,154	10.09	167	0.000104	0.05	12.785	0.192	0.0573	0.0005	0.0781	0.0012	0.6000	0.0104	0.0557	0.0005	0.865	485	7	442	19	–10
7.1	Rim	1729	22,208	12.85	110	0.000097	0.00	13.490	0.231	0.0562	0.0002	0.0740	0.0013	0.5594	0.0106	0.0548	0.0005	0.901	460	8	405	18	–14
7.2	Core	3755	63,576	16.93	233	0.000101	0.06	13.821	0.221	0.0564	0.0002	0.0722	0.0012	0.5472	0.0091	0.0549	0.0002	0.969	450	7	410	7	–10
8.1	Rim	3533	24,908	7.05	193	0.000103	0.20	15.718	0.448	0.0563	0.0002	0.0635	0.0018	0.4796	0.0138	0.0548	0.0002	0.991	397	11	403	11	2
8.2	Core	5890	29,667	5.04	361	0.000035	–0.03	14.020	0.296	0.0555	0.0002	0.0713	0.0015	0.5406	0.0117	0.0550	0.0003	0.976	444	9	413	9	–8
9.2	Core	6969	29,914	4.29	436	0.000026	–0.05	13.724	0.204	0.0556	0.0004	0.0728	0.0011	0.5545	0.0093	0.0552	0.0004	0.886	453	7	421	17	–8
10.1	Core	4517	23,403	5.18	315	0.000038	–0.18	12.357	0.243	0.0558	0.0003	0.0809	0.0016	0.6161	0.0125	0.0553	0.0003	0.970	501	9	423	11	–19
11.1	Rim	3243	26,805	8.26	38	0.000347	1.03	72.965	1.098	0.0559	0.0002	0.0136	0.0002	0.0955	0.0020	0.0508	0.0007	0.722	87.2	1	234	33	63
11.2	Rim	1742	33,584	19.28	109	0.000192	0.15	13.694	0.207	0.0573	0.0002	0.0728	0.0011	0.5464	0.0091	0.0545	0.0004	0.909	453	7	390	16	–16
12.1	Rim	3758	25,133	6.69	251	0.000046	–0.05	12.863	0.201	0.0564	0.0001	0.0777	0.0012	0.5968	0.0095	0.0557	0.0002	0.984	482	7	441	6	–9
12.2	Core	2732	25,945	9.50	178	0.000053	0.01	13.211	0.197	0.0565	0.0002	0.0756	0.0011	0.5811	0.0090	0.0557	0.0002	0.967	470	7	442	9	–6
13.1	Core	4387	27,343	6.23	305	0.000049	–0.27	12.387	0.183	0.0551	0.0003	0.0807	0.0012	0.6049	0.0095	0.0544	0.0003	0.939	500	7	387	12	–29
14.1	Rim	2141	23,380	10.92	150	0.000096	–0.11	12.249	0.183	0.0565	0.0002	0.0815	0.0012	0.6195	0.0097	0.0551	0.0002	0.961	505	7	418	10	–21
14.2	Core	587	33,334	56.78	41	0.000335	0.12	12.182	0.200	0.0584	0.0004	0.0816	0.0013	0.6024	0.0140	0.0535	0.0009	0.708	506	8	352	37	–44
15.1	Core	6428	29,859	4.64	344	0.000111	0.24	16.006	0.236	0.0564	0.0001	0.0624	0.0009	0.4709	0.0073	0.0548	0.0003	0.949	390	6	403	11	3
15.2	Core	6328	30,931	4.89	397	0.000037	–0.35	13.742	0.213	0.0532	0.0013	0.0727	0.0011	0.5283	0.0156	0.0527	0.0013	0.524	453	7	315	57	–43
16.1	Core	1920	28,787	14.99	122	0.000233	0.26	13.528	0.231	0.0582	0.0004	0.0736	0.0013	0.5566	0.0108	0.0548	0.0005	0.877	458	8	406	21	–13
16.2	Core	2027	32,587	16.08	127	0.000131	0.20	13.634	0.206	0.0577	0.0002	0.0732	0.0011	0.5633	0.0092	0.0558	0.0003	0.928	455	7	446	7	–2
17.1	Rim	6005	33,583	5.59	416	0.000055	–0.15	12.415	0.495	0.0560	0.0004	0.0805	0.0032	0.6121	0.0249	0.0552	0.0004	0.981	499	19	419	18	–19
17.2	Core	5513	43,971	7.98	379	0.000062	–0.28	12.514	1.494	0.0549	0.0014	0.0798	0.0095	0.5942	0.0725	0.0540	0.0014	0.978	495	57	370	57	–34
18.1	Rim	2189	34,718	15.86	135	0.000102	0.12	13.917	0.234	0.0568	0.0002	0.0717	0.0012	0.5471	0.0096	0.0553	0.0003	0.952	447	7	425	12	–5
18.2	Core	2440	25,067	10.28	144	0.000063	0.13	14.565	0.240	0.0564	0.0004	0.0686	0.0011	0.5245	0.0097	0.0555	0.0005	0.889	428	7	431	19	1
19.1	Rim	6050	27,216	4.50	357	0.000042	–0.02	14.558	0.221	0.0553	0.0001	0.0686	0.0010	0.5170	0.0080	0.0546	0.0001	0.989	428	6	397	5	–8
19.2	Core	2820	24,056	8.53	178	0.000093	0.08	13.591	0.220	0.0568	0.0002	0.0735	0.0012	0.5613	0.0094	0.0554	0.0002	0.968	457	7	429	9	–7
20.1	Rim	6954	20,216	2.91	71	0.000217	0.86	83.642	1.234	0.0543	0.0005	0.0119	0.0002	0.0840	0.0016	0.0512	0.0006	0.770	76.3	1	248	28	69
20.2	Core	4532	29,995	6.62	279	0.000094	0.11	13.938	0.219	0.0567	0.0001	0.0716	0.0011	0.5464	0.0088	0.0553	0.0002	0.975	446	7	426	8	–5
21.1	Rim	4637	23,888	5.15	277	0.000044	–0.05	14.377	0.221	0.0552	0.0002	0.0695	0.0011	0.5224	0.0082	0.0545	0.0002	0.973	433	6	392	8	–10
21.2	Core	2133	27,555	12.92	130	0.000087	0.11	14.083	0.234	0.0566	0.0003	0.0709	0.0012	0.5407	0.0094	0.0553	0.0003	0.953	442	7	425	12	–4
22.1	Rim	6807	23,818	3.50	322	0.000042	0.13	18.130	0.277	0.0544	0.0003	0.0551	0.0008	0.4091	0.0067	0.0538	0.0003	0.934	346	5	364	13	5
22.2	Rim	4900	33,791	6.90	305	0.000057	0.01	13.807	0.205	0.0560	0.0003	0.0724	0.0011	0.5504	0.0087	0.0552	0.0003	0.938	450	6	419	12	–7

(continued)

TABLE 1. SUMMARY OF SENSITIVE HIGH-RESOLUTION ION MICROPROBE (SHRIMP) U-Pb RESULTS FOR MONAZITE FROM SAMPLES ZNK136 AND ZNK119 *(continued)*

Grain spot	Position	U (ppm)	Th (ppm)	Th/U	206Pb* (ppm)	204Pb/206Pb	f206 %	238U/206Pb	±	207Pb/206Pb	±	206Pb/238U	±	207Pb/235U	±	207Pb/206Pb	±	206Pb/238U	±	207Pb/206Pb	±	% disc.
								Total ratios								Radiogenic ratios		Age (Ma)				
																			σ				
Sample ZNK136 (leucogranite related to thrusting)																							
1.1	Core	8368	42,665	5.10	26	0.000989	0.02	272.2	4.1	0.0580		0.0036	0.00002		0.0007		0.00002	23.30	0.35			
2.1	Rim	7494	27,648	3.69	26	0.000837	0.33	247.7	3.7	0.0557		0.0040	0.00002		0.0004		0.00002	25.67	0.38			
3.1	Rim	6453	28,702	4.45	21	0.000874	0.25	262.4	4.0	0.0564		0.0038	0.00002		0.0004		0.00002	24.22	0.37			
3.2	Core	4939	33,835	6.85	17	0.001295	0.40	238.9	6.3	0.0645		0.0041	0.00003		0.0006		0.00003	26.32	0.70			
4.1	Core	5009	20,995	4.19	17	0.001323	0.06	251.6	3.8	0.0559		0.0039	0.00002		0.0006		0.00002	25.27	0.38			
5.1	Rim	5823	43,067	7.40	19	0.001002	0.53	256.1	3.8	0.0604		0.0038	0.00002		0.0007		0.00002	24.69	0.37			
6.1	Rim	8788	23,386	2.66	28	0.000899	0.34	265.1	4.0	0.0563		0.0037	0.00002		0.0004		0.00002	23.97	0.36			
6.2	Core	6426	42,228	6.57	20	0.001317	0.32	266.1	3.9	0.0600		0.0037	0.00002		0.0006		0.00002	23.77	0.35			
7.1	Rim	6307	25,269	4.01	22	0.001016	0.68	248.0	3.9	0.0554		0.0040	0.00002		0.0005		0.00002	25.65	0.41			
7.2	Core	4073	33,762	8.29	13	0.001878	0.26	257.6	4.1	0.0654		0.0038	0.00002		0.0007		0.00002	24.38	0.38			
8.1	Rim	9000	21,610	2.40	29	0.000754	0.77	264.7	5.1	0.0540		0.0037	0.00002		0.0004		0.00002	24.07	0.47			
8.2	Core	5555	41,415	7.46	18	0.001329	0.15	259.3	3.8	0.0620		0.0038	0.00002		0.0006		0.00002	24.33	0.36			
9.1	Rim	4047	25,996	6.42	12	0.001558	0.21	275.4	7.6	0.0640		0.0036	0.00003		0.0006		0.00003	22.85	0.63			
10.1	Rim	4600	20,959	4.56	15	0.001011	0.00	261.6	7.0	0.0566		0.0038	0.00003		0.0004		0.00003	24.28	0.65			
10.2	Core	3634	30,487	8.39	11	0.001815	0.33	290.4	4.6	0.0623		0.0034	0.00002		0.0007		0.00002	21.72	0.34			
11.1	Rim	5891	22,685	3.85	17	0.000903	0.50	302.8	4.5	0.0524		0.0033	0.00002		0.0004		0.00002	21.10	0.31			
11.2	Core	5012	29,274	5.84	15	0.001118	0.46	287.4	4.4	0.0570		0.0034	0.00002		0.0005		0.00002	22.09	0.34			
12.1	Core	4214	31,565	7.49	13	0.001093	0.41	263.6	3.9	0.0613		0.0037	0.00002		0.0006		0.00002	23.95	0.36			
14.1	Rim	3354	22,156	6.61	11	0.001739	0.25	268.6	4.2	0.0589		0.0037	0.00002		0.0005		0.00002	23.58	0.37			
14.2	Core	5980	39,256	6.56	19	0.001200	0.68	263.0	3.9	0.0592		0.0037	0.00002		0.0006		0.00002	24.08	0.36			
15.1	Core	4970	27,340	5.50	16	0.001590	0.15	259.1	3.8	0.0612		0.0038	0.00002		0.0005		0.00002	24.37	0.36			

Note: Uncertainties are given at the 1σ level. Error in 44069 reference monazite calibration was 1.46% for the analytical session (not included in above errors but required when comparing 206Pb/238U data from different mounts). f206 % denotes the percentage of 206Pb that is common Pb. Correction for common Pb in ZNK119 sample was made using the measured 204Pb/206Pb ratio. Correction for common Pb in ZNK136 for the U/Pb data has been made using the measured 238U/206Pb and 207Pb/206Pb ratios following Tera and Wasserburg (1972) as outlined in Williams (1998). For % discordance (disc.), 0% denotes a concordant analysis.

monazite and zircon ages (ca. 180–280 Ma) for granites in western and eastern Zanskar. This single spot age could represent a rare inherited grain from such granites.

Five monazite analyses yielded ages between 37 and 29 Ma (Figs. 14C and 14D; Table 2): One monazite grain (grain 3 in Fig. 14A) shows oscillatory zoned core with single ages of 37.2 ± 0.8 Ma and 35.5 ± 0.8 Ma, and one monazite grain a Cambrian core (494 ± 10.4 Ma) yielded a rim age of 37.4 ± 1 Ma. Monazite with clear patchy zoning yielded ages of 29 ± 0.6 Ma and 29 ± 0.8 Ma (e.g., grain 2, Fig. 14A; Table 2). Walker et al. (1999) reported U-Pb monazite ages between ca. 35 Ma and 28 Ma for pelitic schists close to Gumburanjun and interpreted them as reflecting new monazite growth during regional Barrovian metamorphism. Walker et al. (1999) also reported similar ages of 37–29 Ma for monazite from deformed mylonitic pegmatites that are crosscut by undeformed Gumburanjun leucogranite, suggesting a major thermal perturbation at this time.

The remaining 15 analyses yielded slightly discordant single 206Pb/238U ages ranging between ca. 26 and 21.7 Ma (Figs. 14C and 14D). This prominent age group does not reveal any systematic relationship between ages and zoning (Fig. 14A). Some grains show similar ages in cores and rims (e.g., grains 4 and 6), some yield slightly older cores than rims (e.g., grain 1), and some have slightly older rims than cores (e.g., grains 7 and 8). The weighted mean 206Pb/238U age for these 15 analysis is 23.1 ± 0.75 Ma (2σ, MSWD = 26). The MSWD value suggests excess scatter, and the probability density plot shows one broad peak between 21.5 Ma and 24.5 Ma (Fig. 14D). We argue that the age spread is real and reflects crystallization ages of the leucogranite during shearing, and that any weighted mean calculation would yield an arbitrary mixed date of no geological significance.

ZNK17E: Undeformed Leucogranite

Like the previous sample, sample ZNK17E is from domain 2b close to Gumburanjun dome, immediately below the Tethyan sedimentary series (ZNK17E: 32°57′21.1″N, 77°14′44.8″E; Fig. 2). It is a fine-grained, undeformed, Tur-Ms leucogranite that crosscuts previously sheared leucogranites (Fig. 8B).

This sample is poor in monazite and yielded only a few grains. These are euhedral with grain size of 50–100 μm (Fig. 14E). One monazite grain contains a large zircon inclusion (Fig. 14E). Three grains show patchy zoning in BSE (grains 1, 3, and 4), and two show concentric zoning (grains 1 and 5 in Fig. 14E). The monazite grains have high U concentrations

Switch from thrusting to normal shearing in the Zanskar shear zone, NW Himalaya: Implications for channel flow

TABLE 2. SUMMARY OF SENSITIVE HIGH-RESOLUTION ION MICROPROBE (SHRIMP) U-Pb RESULTS FOR MONAZITE FROM SAMPLES ZNK103A AND ZNK17E

Grain spot	Position	U (ppm)	Th (ppm)	Th/U	^{206}Pb* (ppm)	^{204}Pb/^{206}Pb	f_{206} %	Total ^{238}U/^{206}Pb	±	^{207}Pb/^{206}Pb	±	Radiogenic ^{206}Pb/^{238}U	±	Age (Ma) ^{206}Pb/^{238}U	±
Sample ZNK103A (leucogranite related to normal shearing)															
1.1	Core	1873	44,860	23.95	6.45	0.00510	7.58	249.59	3.47	0.1064	0.0024	0.00370	0.00005	23.8	0.3
1.2	Rim	4412	46,580	10.56	13.27	0.00321	3.80	285.66	3.30	0.0765	0.0013	0.00337	0.00004	21.7	0.3
2.1	Rim	3457	45,942	13.29	13.99	0.00232	3.11	212.19	2.53	0.0712	0.0010	0.00457	0.00005	29.4	0.4
2.2	Core	4186	60,520	14.46	16.88	0.00267	3.39	213.03	2.52	0.0734	0.0010	0.00454	0.00005	29.2	0.3
3.1	Rim	4356	73,653	16.91	20.84	0.00113	0.75	179.58	2.04	0.0527	0.0007	0.00553	0.00006	35.5	0.4
3.2	Core	6459	99,225	15.36	32.35	0.00085	0.64	171.52	1.93	0.0518	0.0006	0.00579	0.00007	37.2	0.4
3.3	Rim	13,988	45,082	3.22	43.65	0.00097	1.58	275.28	2.88	0.0590	0.0004	0.00358	0.00004	23.0	0.2
4.1	Rim	6461	51,023	7.90	21.03	0.00382	5.77	263.95	3.01	0.0921	0.0010	0.00357	0.00004	23.0	0.3
4.2	Core	5662	56,779	10.03	19.47	0.00400	5.80	249.86	3.01	0.0924	0.0012	0.00377	0.00005	24.3	0.3
4.3	Rim	5998	55,286	9.22	20.23	0.00240	4.21	254.69	2.82	0.0798	0.0012	0.00376	0.00005	24.2	0.3
5.1	Core	6840	65,150	9.52	20.50	0.00230	2.31	286.65	3.25	0.0647	0.0008	0.00341	0.00004	21.9	0.2
6.1	Core	10,822	51,705	4.78	32.35	0.00076	0.96	287.40	3.15	0.0541	0.0006	0.00345	0.00004	22.2	0.2
6.2	Rim	8593	61,410	7.15	25.67	0.00165	1.64	287.54	3.21	0.0595	0.0009	0.00342	0.00004	22.0	0.2
7.1	Rim	4982	42,990	8.63	18.36	0.00350	3.55	233.18	2.72	0.0746	0.0009	0.00414	0.00005	26.6	0.3
7.2	Core	8943	89,702	10.03	27.66	0.00129	1.38	277.79	3.20	0.0574	0.0008	0.00355	0.00004	22.8	0.3
8.1	Rim	3500	41,274	11.79	12.39	0.00262	3.61	242.65	2.87	0.0751	0.0010	0.00397	0.00005	25.6	0.3
8.2	Core	2905	49,013	16.87	9.83	0.00355	4.96	253.85	3.25	0.0857	0.0013	0.00374	0.00005	24.1	0.3
9.1	Core	5507	56,232	10.21	361.80	0.00005	0.01	13.08	0.14	0.0567	0.0003	0.07647	0.00081	475.0	4.9
10.1	Rim	10,198	59,677	5.85	31.63	0.00221	2.95	276.96	2.98	0.0698	0.0005	0.00350	0.00004	22.5	0.2
10.2	Core	3305	9855	2.98	226.11	0.00008	<0.01	12.56	0.13	0.0569	0.0002	0.07965	0.00087	494.0	5.2
11.1	Core	9740	12,811	1.32	29.26	0.00177	3.16	285.99	3.12	0.0715	0.0007	0.00339	0.00004	21.8	0.2
12.1	Rim	7183	48,770	6.79	37.04	0.00173	3.10	166.59	2.42	0.0713	0.0008	0.00582	0.00008	37.4	0.5
12.2	Core	10,880	82,788	7.61	357.11	0.00012	0.86	26.17	0.27	0.0579	0.0002	0.03788	0.00040	239.7	2.5
13.1	Core	4684	35,320	7.54	295.14	0.00005	0.08	13.63	0.14	0.0567	0.0002	0.07329	0.00079	456.0	4.7
13.2	Core	6891	40,633	5.90	431.60	0.00005	0.09	13.72	0.15	0.0568	0.0002	0.07284	0.00079	453.3	4.7
Sample ZNK17E (undeformed leucogranite)															
1.1	Core	2769	47,478	17.14	14.2	0.017236	33.41	167.8	3.6	0.3107	0.0680	0.00397	0.00052	25.5	3.3
1.2	Rim	2638	49,731	18.85	8.6	0.005500	7.01	264.9	3.4	0.1019	0.0015	0.00351	0.00005	22.6	0.3
2.1	Core	3689	84,013	22.77	13.3	0.005625	7.41	238.6	2.8	0.1052	0.0012	0.00388	0.00005	25.0	0.3
3.1	Core	14,414	176,644	12.25	46.4	0.002856	4.51	266.9	2.9	0.0822	0.0037	0.00358	0.00004	23.0	0.3
3.2	Rim	8323	88,506	10.63	25.6	0.004360	6.21	279.1	3.3	0.0955	0.0037	0.00336	0.00004	21.6	0.3
4.1	Core	3952	48,915	12.38	22.3	0.005912	10.30	152.1	16.2	0.1283	0.0100	0.00590	0.00063	37.9	4.1
5.1	Core	9962	63,368	6.36	95.7	0.031548	62.01	89.4	1.4	0.5372	0.0200	0.00425	0.00032	27.3	2.0
5.2	Rim	10,909	44,355	4.07	35.7	0.000766	0.69	262.7	2.8	0.0519	0.0004	0.00378	0.00004	24.3	0.3
5.3	Rim	22,470	67,834	3.02	119.2	0.017932	44.47	162.0	3.3	0.3981	0.0026	0.00343	0.00009	22.1	0.6

Note: Uncertainties are given at the 1σ level. Error in 44069 reference monazite calibration was 0.65% for the analytical session (not included in above errors but required when comparing data from different mounts). f_{206} % denotes the percentage of ^{206}Pb that is common Pb. Correction for common Pb for the U/Pb data has been made using the measured ^{238}U/^{206}Pb and ^{207}Pb/^{206}Pb ratios following Tera and Wasserburg (1972) as outlined in Williams (1998).

(2600–22,000 ppm, Ø = 8800 ppm; Table 2). Nine spots on the five mounted monazites were analyzed. All analyses are slightly normally discordant (Fig. 14F). One single monazite core yielded an age of 38 ± 8.2 Ma (Fig. 14E). The remaining analyses yielded single ages between 27 Ma and 21.6 Ma (Fig. 14G; Table 2) with a broad peak at ca. 23–21.5 Ma. We interpret these as the crystallization ages of this late leucogranite dike.

In summary, leucogranites related to thrusting yielded two ^{206}Pb/^{238}U age groups: a younger one between 26 and 21 Ma, with a weighted mean age of 24.0 ± 0.25 Ma (Fig. 13) and an older, ill-defined group of Ordovician to Devonian ages (between 460 and 360 Ma) with a weighted mean ^{207}Pb/^{206}Pb age of 427 ± 7.6 Ma (Fig. 13). The latter is thought to represent the age of the Kade orthogneiss that forms the bulk of the Zanskar Range. The younger age spread is interpreted to indicate the duration of anatexis from thrusting through normal movement to the end of pervasive normal shearing. The leucogranite sheared by the Zanskar shear zone shows a prominent age group between ca. 26 and 21.7 Ma. The late leucogranite sample,

crosscutting previously sheared granites, has ages between 23 and 21.5 Ma (Fig. 14).

METAMORPHISM IN THE GUMBURANJUN AREA (DOMAIN 2b): EARLY METAMORPHIC REMNANT

Metamorphism in the High Himalayan Crystalline sequence in the Gumburanjun region has been studied by several authors (e.g., Pognante, 1992; Dézes et al., 1999; Walker et al., 1999). Peak metamorphism was a result of top-to-the-SW thrusting and folding, and isograds were exhumed right-way-up and telescoped during normal shearing (Dézes et al., 1999; Walker et al., 1999). Previous work describes regional metamorphic isograds (from kyanite to biotite zone from footwall to hanging wall) tightly spaced over the thickness of the Zanskar shear zone (Herren, 1987; Dézes et al., 1999; Walker et al., 1999), separating the hot migmatites and granite injection complexes of the High Himalayan Crystalline sequence footwall to the south from greenschist facies rocks of the Tethyan sedimentary series hanging wall to the north. Within this broad pattern, we have found that there are

small regions within the Zanskar shear zone in the Gumburanjun area (domain 2b) where the opposite pattern is preserved (Figs. 15 and 16).

South of the Gumburanjun dome complex, a metamorphic series from biotite to kyanite zone is exposed in two regions (Fig. 15). In locality ZNK95, the full sequence is exposed vertically over a structural thickness (perpendicular to the foliation) of ~20 m; in the other locality (field points ZNK106–108), the full sequence is exposed over a structural thickness of ~70 m (Fig. 15). The metamorphic facies are distributed so that lower metamorphic conditions are found closer to the granite intrusions toward the footwall, and the higher metamorphic conditions are found structurally above, toward the hanging wall, thus defining an inverted metamorphic sequence at decametric scale.

In this section, we detail the assemblage and mineral composition in each main zone. The mineral composition in selected samples was analyzed using the Tescan Vega Electron Microscope with attached Oxford EDS (Energy Dispersive Spectroscopy system) detector at IPSG (Institute of Petrology and Structural Geology), Charles University, Prague, Czech Republic, at
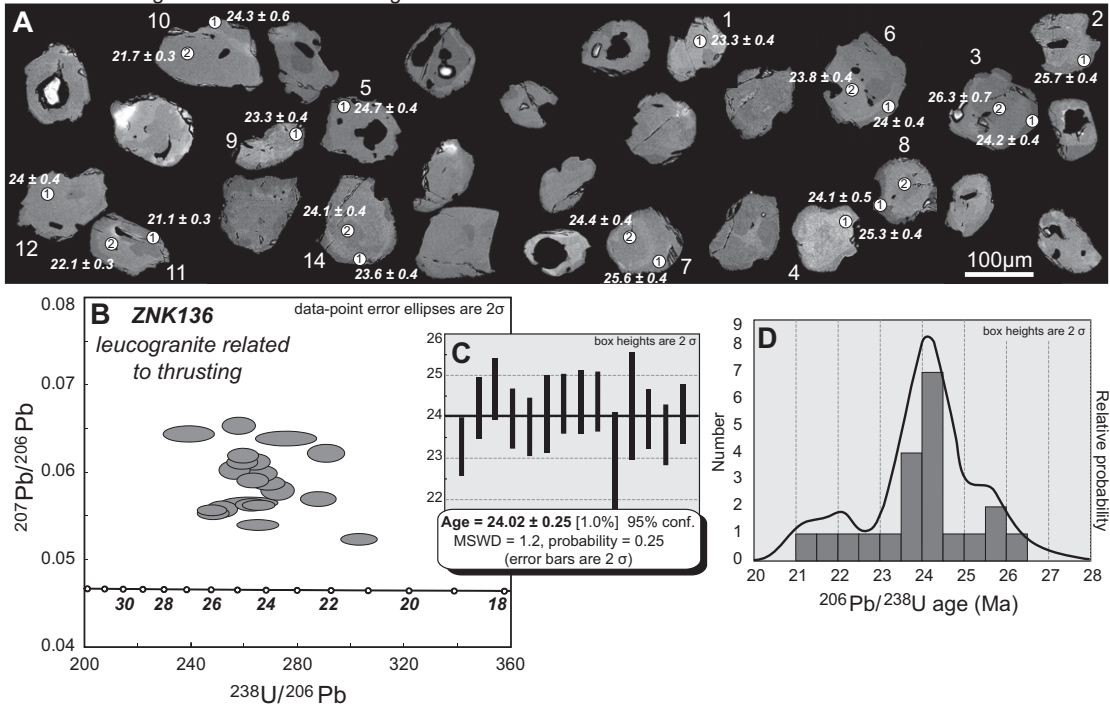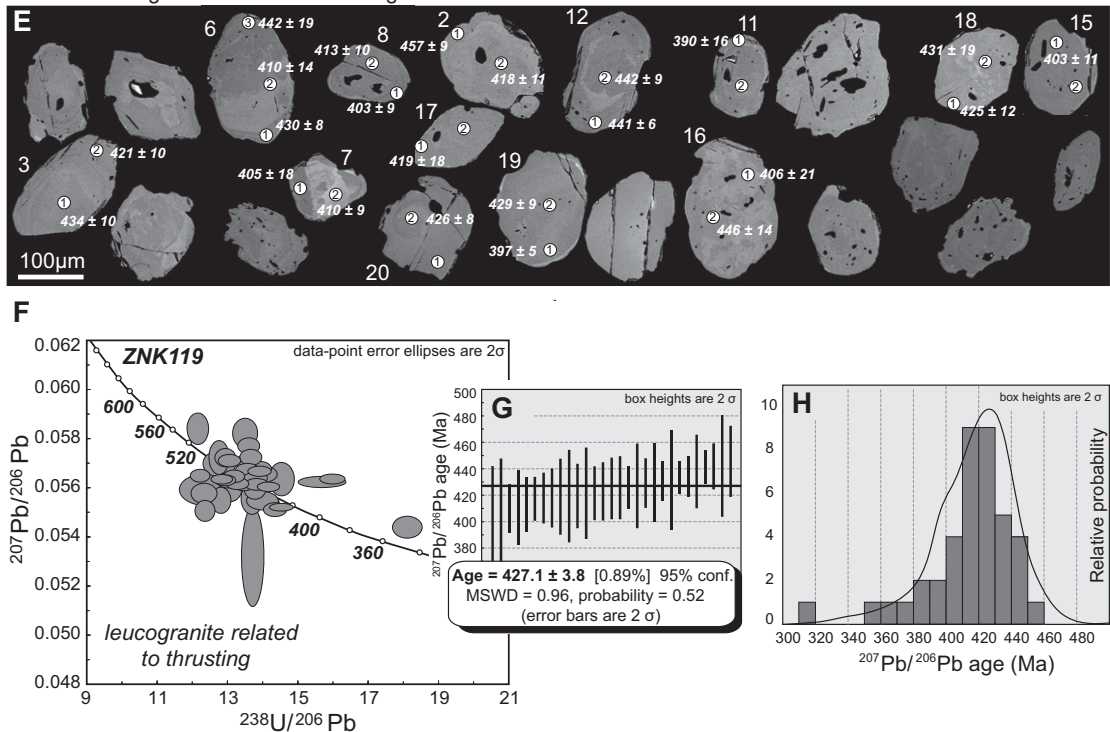
Figure 13. Results of monazite geochronology for leucogranite samples ZNK136 (A–D) and ZNK119 (E–H), both related to thrusting. Sample ZNK 136: (A) Backscattered electron (BSE) images of selected grains. Analyzed spots with obtained $^{206}Pb/^{238}U$ ages (Ma) are marked. Uncertainties are given at 1σ level. Grain and spot numbers correspond to numbering in Table 1. (B) Tera-Wasserburg concordia plot for all analyses. MSWD—mean square of weighted deviates. (C) Weighted mean average plot of $^{206}Pb/^{238}U$ ages for monazites. Error bars are 2σ. (D) $^{206}Pb/^{238}U$ age (Ma) probability density plot for all individual data. Sample ZNK119: (E) BSE images of selected grains. Analyzed spots with obtained $^{207}Pb/^{206}Pb$ ages (Ma) are marked. Uncertainties are given at 1σ level. Grain and spot numbers correspond to numbering in Table 1. (F) Tera-Wasserburg concordia plot for all analyses. (G) Weighted mean average plot of $^{207}Pb/^{206}Pb$ ages for monazites. Error bars are 2σ. (H) $^{207}Pb/^{206}Pb$ age (Ma) probability density plot for all individual data. Calculated $^{207}Pb/^{206}Pb$ ages were used for sample ZNK119, as most of the data are reversely discordant.
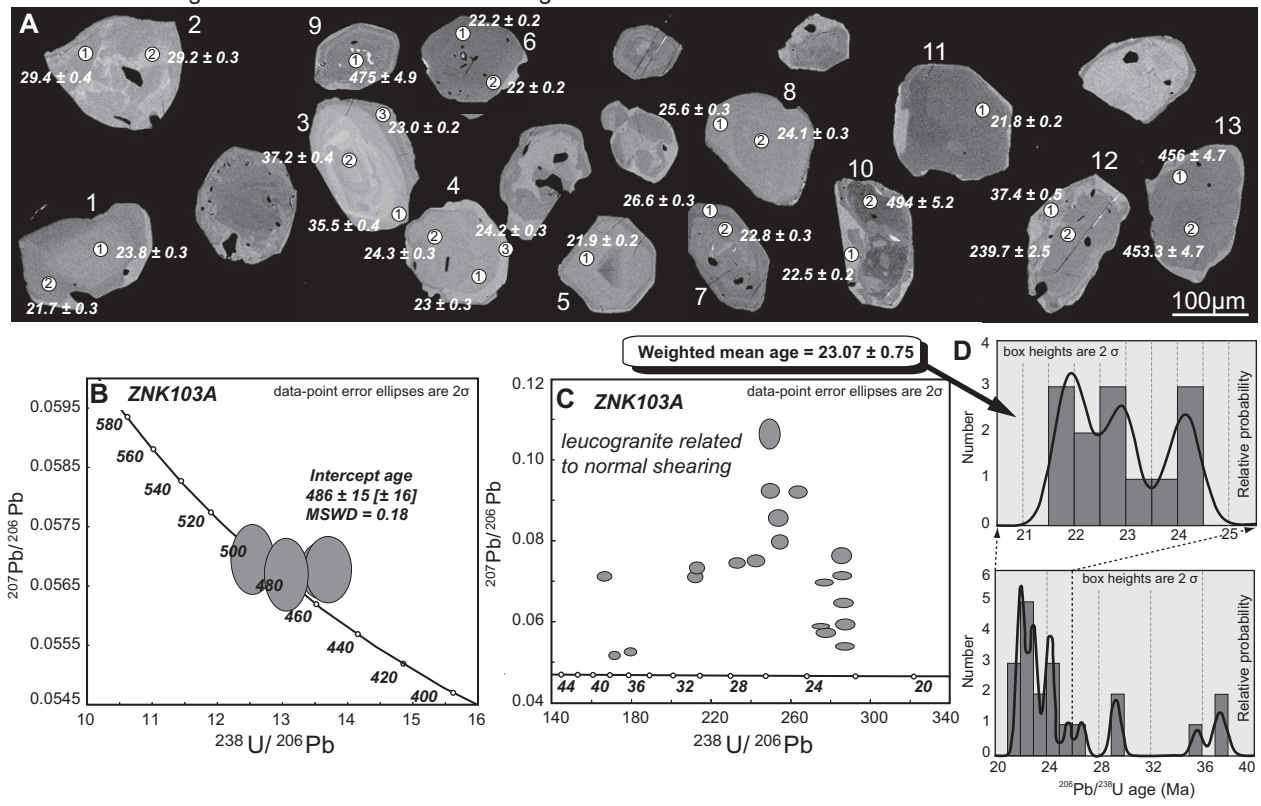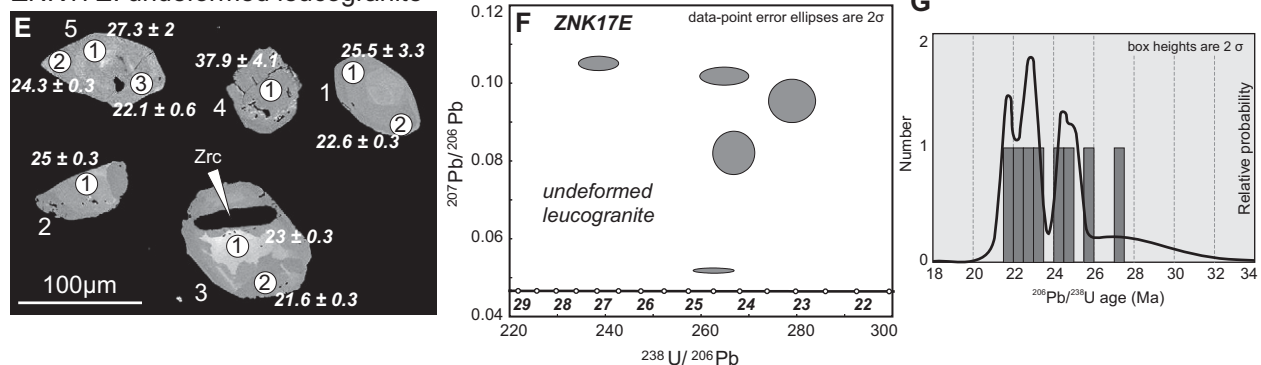
Figure 14. Results of monazite geochronology for leucogranite sample ZNK103A sheared by normal movement (A–D) and for undeformed leucogranite sample ZNK17E postdating normal shearing (E–G). ZNK103A: (A) Backscattered electron (BSE) images of selected grains. Analyzed spots with obtained $^{206}Pb/^{238}U$ ages (Ma) are marked. Uncertainties are given at 1σ level. Grain and spot numbers correspond to numbering in Table 2. (B) Tera-Wasserburg concordia plot for the old ages group. MSWD—mean square of weighted deviates. (C) Tera-Wasserburg concordia plot for the main age group. (D) $^{206}Pb/^{238}U$ age (Ma) probability density plot for the main data group. Upper plot reveals $^{206}Pb/^{238}U$ age (Ma) probability density plot for the youngest and most prominent age group. ZNK17E: (E) BSE images of selected grains. Analyzed spots with obtained $^{206}Pb/^{238}U$ ages (Ma) are marked. Uncertainties are given at 1σ level. Grain and spot numbers correspond to numbering in Table 2. (F) Tera-Wasserburg concordia plot for all analyses. (G) $^{206}Pb/^{238}U$ age (Ma) probability density plot for the main data group.

15 kV and 10 nA. The abbreviations used are almandine (alm) = Fe/(Fe + Ca + Mn + Mg); pyrope (py) = Mg/(Fe + Ca + Mn + Mg); grossular (grs) = Ca/(Fe + Ca + Mn + Mg); spessartine (sps) = Mn/(Fe + Ca + Mn + Mg); and $X_{Fe} = Fe_{tot}/(Fe_{tot} + Mg)$. Representative mineral analyses are summarized in Table 3.

Biotite Zone

In both localities, there is a biotite zone closest to the intrusion complex in the footwall. The schists in this zone usually contain Bt + Ms + Pl + Qtz and late chlorite replacing biotite. Foliation is defined by recrystallized quartz and plagioclase grains and preferred orientation of biotite and muscovite.

Garnet Zone

This zone is structurally above the biotite zone, away from the footwall, and mica schists are composed of Bt + Ms + Pl + Qtz + Grt +

Chl with accessory amounts of Ilm, Gr, Ap, Mnz, and Zrn. The foliation is defined by the alignment of biotite and muscovite (Figs. 9A and 9B). Garnet porphyroblasts (0.5–1 mm in size) are sub- to euhedral in shape, and there are two distinct groups. One contains straight inclusion trails of quartz, plagioclase, and ilmenite, defining an internal foliation discontinuous with the external foliation defined by elongate biotite and muscovite (Fig. 9A). The external foliation wraps around these garnets, forming asymmetric strain shadows. The other group displays curved inclusion trails of quartz and plagioclase that are continuous with the external foliation (Fig. 9B). This indicates two possible generations of garnet (Fig. 9G).

Compositionally, garnet is mostly unzoned ($\sim alm_{75–80}prp_{10–12}grs_{4–6}sps_{10–16}$; $X_{Fe} = 0.86–0.89$) or displays rims enriched in Ca and depleted in Mn. There is no significant compositional difference between the two different garnet groups. Biotite X_{Fe} ranges between 0.52 and 0.55, and Ti ranges between 0.09 and 0.11 apfu. Plagioclase has anorthite content of ~0.2, and chlorite is retrograde and present in small amounts at contacts with biotite.

Staurolite Zone

Further up structurally, this zone has a mineral assemblage including Bt + Ms + Pl + Qtz + St + Grt + Chl with accessory amounts of Ilm, Tur, Gr, Ap, Mnz, and Zrn (this compares to sample WAK 9 of Walker et al. [1999], discussed in section "Timing of Peak Metamorphism, Anatexis, and Switch in Movement Direction on the Zanskar Shear Zone"). Euhedral garnet porphyroblasts (0.5–1 mm in size) are either inclusion free or have straight to curved inclusion trails of quartz and plagioclase, similar to those found in the garnet zone. Garnet composition is $\sim alm_{73–76}prp_{10–12}grs_{6–8}sps_{12–18}$; X_{Fe} ~0.87. Staurolite grains up to 2 cm in size have varied textures, from euhedral to highly corroded grains, and are poikiloblastic to inclusion free (Figs. 9C–9E). Most staurolite is elongate parallel to the main foliation (SW-NE direction; Figs. 9C and 9E) with fractures at a high angle to the foliation that are filled with chlorite (Fig. 9E), indicative of stretching along the foliation. Inclusion trails of quartz, ilmenite, and graphite are either continuous with the external foliation (C and S planes; Fig. 9C) or parallel to C′ planes (Fig. 9D). The external foliation wraps around the grains, producing asymmetric strain shadows of quartz and mica (Figs. 9C and 9D). Staurolite porphyroblasts are chemically unzoned with an X_{Fe} range of 0.77–0.85. Chlorite is retrograde and seen in small amounts at contacts with biotite or partially replacing

staurolite. Biotite and muscovite define S, C, and C′ planes (Figs. 9C–9E). Biotite has $X_{Fe} = 0.45–0.50$ and Ti = 0.07–0.11 apfu.

Kyanite Zone

Mica schists from this zone are furthest from the intrusion complex and contain Bt + Ms + Pl + Qtz + Ky + St and accessory amounts of Grt, Mnz, Zrn, Ap, Ilm, and Tur. Kyanite porphyroblasts (up to 1 cm in size) do not contain inclusions, and their prisms are oriented parallel to foliation (Fig. 9F). Similar to staurolite, kyanite is stretched, with fractures filled with muscovite perpendicular to foliation. Staurolite X_{Fe} values range between 0.74 and 0.82. Biotite

X_{Fe} values range between 0.39 and 0.42, and Ti ranges between 0.08 and 0.11 apfu.

From the biotite zone toward the kyanite zone, the X_{Fe} of staurolite (0.87 =>0.73), garnet (0.95 =>0.84), and biotite (0.57 =>0.4) decreases gradually, which is consistent with increasing temperatures. Staurolite, garnet, and kyanite porphyroblasts reveal a complex history (Fig. 9G). There are either porphyroblasts with straight or curved inclusion trails continuous with external foliation, or with straight inclusion trails, discontinuous with the external foliation. The long direction of porphyroblasts is parallel to C and/or S planes or to C′ planes (Fig. 9G).

Inverted metamorphic sequence, with hotter rocks structurally above colder rocks (Figs. 15

Figure 15. Inverse Barrovian metamorphic sequences south of Gumburanjun dome in domain 2b. (A) Geological map showing locations of lithons that contain remnant isograds related to thrusting. ZSZ—Zanskar shear zone; HHL—High Himalayan leucogranites; HHC—High Himalayan Crystalline sequence; TSS—Tethyan sedimentary series. (B) Cross section of locality ZNK95 showing isograd distribution over 20 m, C-S shear bands, and antithetic and synthetic C′ shear bands indicative of top-down-to-the-S shear. (C) Cross section of localities ZNK106–108 showing isograd distribution and antithetic and synthetic C′ shear bands indicative of top-down-to-the-S. Mineral abbreviations after Kretz (1983).

Figure 16. Schematic block diagram of Gumburanjun dome and the preserved lithons of inverted metamorphism, with high-temperature minerals closer to hanging wall grading to lower-temperature minerals toward footwall. Regional metamorphic gradient related to normal shearing shows opposite pattern, grading to high-temperature minerals toward footwall. The inverted metamorphic gradient is a result of the earlier stage of thrusting, but distance between metamorphic isograds in lithons has been telescoped during normal shearing. Figure is schematic and not to scale; see Figures 2 and 15 for scale of dome and lithons. HHC—High Himalayan Crystalline sequence; TSS—Tethyan sedimentary series. Mineral abbreviations after Kretz (1983).

and 16) has not been documented by previous authors, and is the opposite of the regional isograds, which have high-grade rocks below low-grade rocks (Fig. 16). These inverted isograd sequences suggest they result from the early thrusting event. The proximity between isograds in the field indicates telescoping of the original distances, perhaps caused by normal shearing, and presumably overprinted, but not actually significantly modified, by the later right-way-up metamorphism related to normal movement (Figs. 15 and 16).

Pressure-Temperature Estimates for the Inverted Metamorphic Sequence

In order to estimate the pressure-temperature conditions for the inverted metamorphic sequence, we calculated a pseudosection for sample ZNK106C, a Grt-Bt schist from the garnet zone (Fig. 17) in the system MnO–Na$_2$O–CaO–K$_2$O–FeO–MgO–Al$_2$O$_3$–SiO$_2$–H$_2$O–TiO$_2$–O (MnNCKFMASHTO) with H$_2$O and quartz in excess. The rock composition consisted of molar amounts of these oxides normalized to 100%, and Fe was treated as FeO (Fig. 17). The calculations were performed using THERMOCALC 3.33 (Powell et al., 1998; 2005 upgrade) and the internally consistent thermodynamic data set 5.5 (Holland and Powell, 1998; November 2003 upgrade). The activity-composition relationship is from White et al. (2000) for chloritoid and magnetite, from Holland and Powell (2003) for the feldspars, from Coggon and Holland (2002) for paragonite–muscovite, from White et al. (2005) for garnet and biotite, from Mahar et al. (1997) for cordierite and staurolite, from White et al. (2002) for orthopyroxene, and from White et al. (2005) for ilmenite and hematite. Mineral compositional isopleths were plotted for the phases of interest (garnet, biotite, and staurolite) in order to decipher the pressure-temperature conditions for each of the metamorphic zones. Compositions of minerals used to determine the metamorphic conditions are listed in Table 3.

The major features of the MnNCKFMASHTO system are stability of garnet above 3.5 kbar (at <650 °C), stability of staurolite between 550 °C (at 3.4 kbar) and 655 °C (below 7.5 kbar), and sillimanite stability above 580 °C (4 kbar) and below 6.5 kbar (at 650 °C). Paragonite is present at low temperatures; muscovite is absent in the high-temperature and low-pressure part of the pseudosection.

The pseudosection indicates, as expected, a gradual increase in metamorphic conditions from the biotite to the kyanite zone (Fig. 17B). The mineral assemblage of Bt + Ms + Pl + Ilm + Pa of the biotite zone is stable at metamorphic conditions of 550–560 °C and 5–6.1 kbar (Fig. 17). The assemblage Grt + Bt + Ms + Pa + Qtz + Pl + Ilm of the garnet zone, and observed composition of biotite (X_{Fe} = 0.52–0.54) and

Finch et al.

TABLE 3. REPRESENTATIVE ANALYSES OF GARNET, STAUROLITE, BIOTITE, AND PLAGIOCLASE FROM THE DIFFERENT METAMORPHIC ZONES

| | Garnet zone | | | | | | Staurolite zone | | | | | | | | | Kyanite zone | | | | | |
| | ZNK95C | | | ZNK106 | | | ZNK95B | | | | | ZNK107 | | | | ZNK95A | | | ZNK108 | | |
Mineral:	Grt-core	Grt-rim	Bt	Grt-core	Grt-rim	Bt	Bt	St-core	St-rim	Grt-core	Grt-rim	Bt	St-core	St-rim	Pl	Bt	St-core	St-rim	Bt	St-core	St-rim
Oxide (wt%)																					
SiO$_2$	36.51	36.55	35.18	36.16	36.68	34.98	53.74	26.54	26.53	36.13	37.02	36.42	26.73	26.79	62.86	36.57	26.72	26.66	35.98	26.45	26.19
TiO$_2$			1.67	0.00	0.00	1.81	1.29	0.54	0.57	0.00	0.00	1.75	0.65	0.54		1.57	0.59	0.75	1.69	0.72	0.62
Al$_2$O$_3$	20.77	20.90	19.57	20.77	21.10	18.73	13.69	54.38	54.20	20.64	21.20	19.67	54.55	55.25	23.31	19.84	54.40	54.70	19.45	54.75	54.97
FeO	31.96	36.18	19.63	34.07	34.75	21.31	12.68	14.00	13.82	33.73	33.34	17.37	12.91	12.33		14.99	12.66	12.50	15.60	12.82	12.98
MnO	3.40	1.94	0.00	2.55	2.11	0.00	0.04	0.26	0.29	4.14	3.52	0.00	0.38	0.34		0.14	0.46	0.54	0.13	0.44	0.49
MgO	2.08	3.11	9.32	2.61	2.89	9.12	8.15	1.87	1.77	2.57	2.98	11.14	1.82	1.80		12.90	2.23	1.88	12.80	1.85	1.75
CaO	5.25	1.55		3.39	2.59					2.72	3.02				4.28						
Na$_2$O			0.27			0.24	0.29					0.37			9.04	0.41			0.48		
K$_2$O			8.83			8.73	6.46					8.69			0.13	8.83			8.91		
Total	99.97	100.24	94.47	99.56	100.12	94.92	96.34	97.60	97.18	99.92	101.09	95.41	97.04	97.05	99.62	95.25	97.42	97.27	95.04	97.03	97.00
Oxygens	12	12	11	12	12	11	11	48	48	12	12	11	48	48	12	11	48	48	11	48	48
Si	2.94	2.94	2.77	2.93	2.95	2.76	4.20	7.53	7.56	2.92	2.95	2.81	7.61	7.61	2.79	2.78	7.57	7.58	2.75	7.53	7.46
Ti	0.00	0.00	0.10	0.00	0.00	0.11	0.08	0.12	0.12	0.00	0.00	0.10	0.14	0.12		0.09	0.13	0.16	0.10	0.15	0.13
Al	1.97	1.98	1.82	1.98	2.00	1.74	1.26	18.18	18.20	1.97	1.99	1.79	18.31	18.50	1.22	1.78	18.17	18.32	1.75	18.37	18.45
Fe^{3+}	0.15	0.13		0.16	0.10			2.53	2.43	0.19	0.12		2.19	2.05			2.50	2.26		2.26	2.36
Fe^{2+}	2.01	2.30	1.29	2.14	2.24	1.41	0.83	0.79	0.86	2.09	2.10	1.12	0.89	0.88		0.95	0.50	0.71	1.00	0.79	0.73
Mn	0.23	0.13	0.00	0.18	0.14	0.00	0.00	0.06	0.07	0.28	0.24	0.00	0.09	0.08		0.01	0.11	0.13	0.01	0.11	0.12
Mg	0.25	0.37	1.09	0.32	0.35	1.07	0.95	0.79	0.75	0.31	0.35	1.28	0.77	0.76		1.46	0.94	0.79	1.46	0.79	0.74
Ca	0.45	0.13		0.29	0.22					0.24	0.26				0.20						
Na			0.04			0.04	0.04					0.06			0.78	0.06			0.07		
K			0.89			0.88	0.64					0.85			0.01	0.86			0.87		
X$_{Fe(tot)}$	0.90	0.87	0.54	0.88	0.87	0.57	0.47	0.80	0.80	0.88	0.86	0.47	0.79	0.78	0.78 An	0.39	0.74	0.78	0.41	0.78	0.79
Prp	0.08	0.12		0.10	0.11					0.10	0.12				0.21 Ab						
Alm	0.70	0.79		0.74	0.77					0.73	0.72				0.79 Or						
Grs	0.15	0.04		0.10	0.07					0.08	0.08				0.01						
Sps	0.13	0.09		0.11	0.09					0.17	0.14										

Note: X$_{Fe}$ = Fe$_{tot}$/(Fe$_{tot}$ + Mg); Alm = Fe/(Fe + Mg + Ca + Mn); Prp = Mg/(Fe + Mg + Ca + Mn); Grs = Ca/(Ca + Na + K); An = Ca/(Ca + Na + K); Ab = Na/(Ca + Na + K); Or = K/(Ca + Na + K). Alm—Almandine; Prp—Pyrope; Grs—Grossular; Sps—Spessartine.

garnet (Alm = 75–80; Sps = 4–6), indicates metamorphic conditions of ~590 °C at 5.2–6 kbar (Fig. 17). The assemblage of Grt + Bt + Ms + St + Pl + Qtz + Ilm in the staurolite zone and observed composition of biotite (X_{Fe} = 0.48–0.50), garnet (Alm = 74–76), and staurolite (X_{Fe} = 0.84–0.85) indicate a further increase in metamorphic conditions to 600–640 °C at 6–6.8 kbar (Fig. 17). Finally, the kyanite zone, with its mineral assemblage of Ky + St + Grt + Pl + Qtz + Ilm suggests conditions of ~650 °C at 6.4–7.5 kbar. Altogether, the results indicate a minimum temperature difference of ~100 °C with an accompanying increase in pressure of the order of 1 kbar between the biotite (~550 °C, 5–6.1 kbar) and kyanite (~650 °C, 6.4–7.5 kbar) metamorphic zones (Fig. 17B). This difference in conditions over the current structural thickness of 20 to 70 m indicates significant telescoping of the original isograd distances.

STRAIN ANALYSIS AND LOCALIZATION

The Zanskar shear zone in domain 2a is bound in its hanging wall, in the northeast, by a decrease in normal shear strain, signaled by relics of thrusting and accompanied by a change in lithology. A similar decrease in normal shearing intensity is seen in the footwall of the Zanskar shear zone (domain 1; Fig. 5). The horizontal thickness of the Zanskar shear zone, from footwall to hanging wall in domain 2a, measured perpendicular to strike of the dominant shear foliation, is 1.55 km (see subsection on domain 2a for description of the boundaries of the Zanskar shear zone). Correcting for the 33° (+18°/–12°) average dip of the foliation yields a true thickness of 0.83 km (+0.14/–0.29 km).

Within the shear zone, leucogranite dikes form sills following alternatively one of the three main shear planes: C, S, or C′ planes (Fig. 18). The typical pattern of these curved dikes is that they step up and across the shear zone, alternating in orientation between thin and stretched sections parallel with the C plane, and shorter and wider sections parallel to the S plane (Figs. 18A–18C). This pattern is interrupted by spaced, crosscutting C′ planes that stretch the dike and move it downwards (Fig. 18). Combined, this deformation leads to dikes with an overall trend that is parallel to the shear zone, but that locally trends at an angle to it.

Within mylonitic Kade orthogneisses and leucogranites, strain is localized to shear zones along micaceous planes and marked by considerable displacement of markers such as leucogranitic dikelets (Figs. 6 and 18). These zones cause leucogranitic dikes and lenses that were
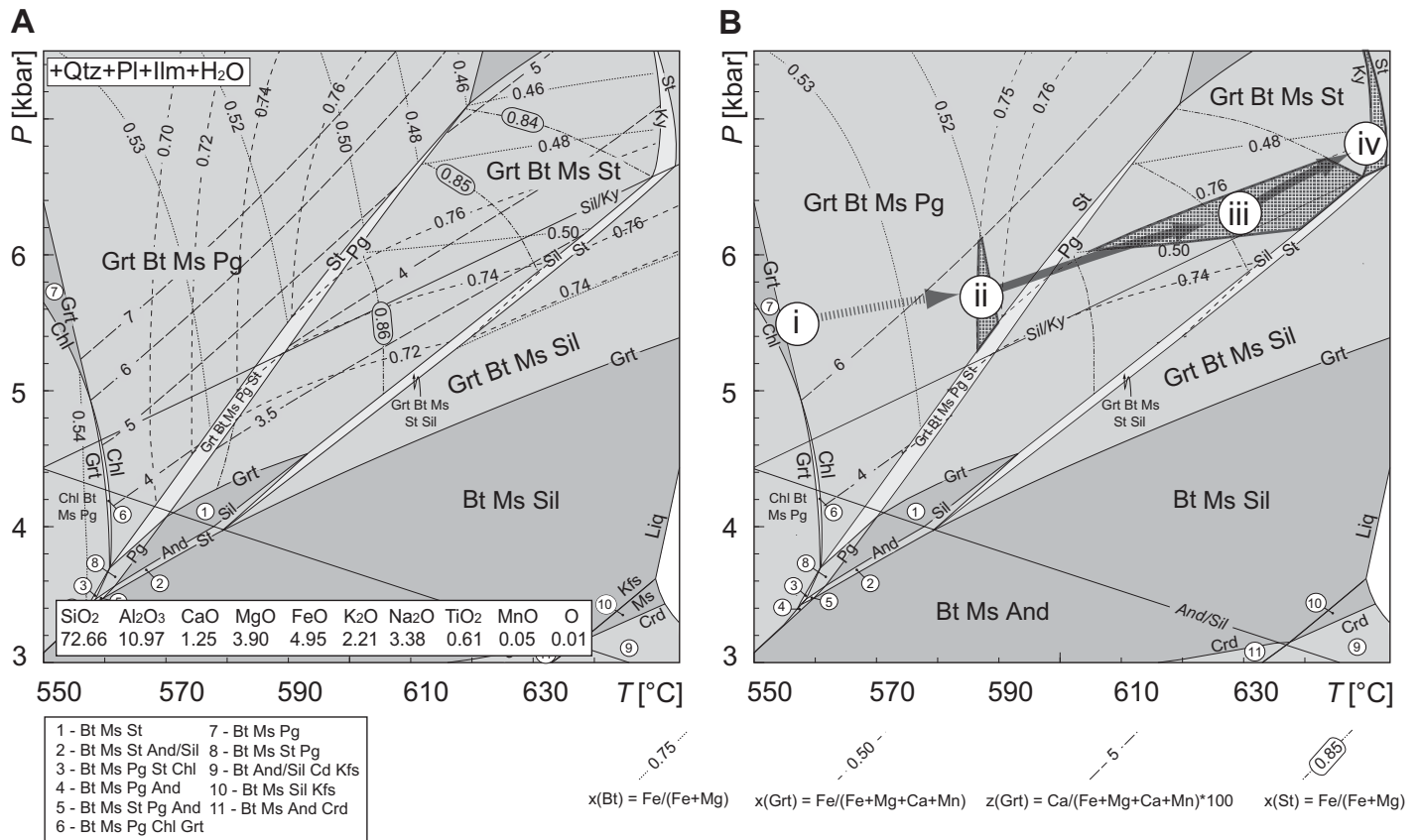
Figure 17. (A) MnO–Na₂O–CaO–K₂O–FeO–MgO–Al₂O₃–SiO₂–H₂O–TiO₂–O (MnNCKFMASHTO) pressure-temperature pseudosection for sample ZNK106. Isopleths of x(Grt), z(Grt), x(Bt), and x(St) are shown. (B) Simplified version of A marking suggested pressure-temperature path from biotite zone (i) to garnet zone (ii), staurolite zone (iii), and finally to kyanite zone (iv). Mineral abbreviations after Kretz (1983).

once continuous to be separated into semicontinuous or discontinuous asymmetric lenses (Fig. 18). The effect of this is also seen on a smaller scale with σ-clasts derived from strongly sheared dikes (Fig. 6B).

We use the fact that dikes are rotated into parallelism with the shear plane at the metric to decametric scale to estimate the total amount of shear strain on these structures, rather than the angle between the S and C planes (Fig. 18; Ramsay and Graham, 1970). For this approach, we assume dikes intruded on average approximately perpendicular to the foliation, an assumption that cannot be verified since they are all now rotated to the shear planes. This approach also assumes strain was roughly similar across the width of the shear zone. Our observations across the shear zone indicate this is a reasonable assumption. We assume here an overall angle between average dike orientation and shear planes to be a conservative 2°. A lower angle is possible, and the results are strongly sensitive to such a decrease in angle. A larger angle is unlikely because we would have

been able to measure it in the large exposures available. Using the following equation from Ramsay and Graham (1970, p. 799):

$$\gamma = 2/\tan 2\theta, \qquad (1)$$

where γ is the shear strain, and θ is the angle between dike orientation and shear plane, yields an average value of γ = 28.6. Over the 0.83 (+0.14/–0.29) km thickness of the Zanskar shear zone, a γ value of 28.6 yields a heave of 20 km, throw of 13 km, and ~24 km (–8/+4 km) displacement parallel to the shear plane. This result is within error of those calculated by Herren (1987) and Dézes (1999), who used the thinning of metamorphic isograds and found a minimum displacement of 25 km and 35 ± 9 km, respectively. This technique measures only simple shear; however, several studies have shown that there is a significant component of pure shear in the High Himalayan Crystalline sequence shear zones (e.g., Law et al., 2004; Jessup et al., 2006; Larson and Godin, 2009), and this could modify our estimates.

DISCUSSION

The ~1 km thickness of the Zanskar shear zone in domain 2a is narrower than in other areas in Zanskar, where it reaches up to 6.75 km (Herren, 1987). Strain analysis indicates that the Zanskar shear zone in domain 2a accommodated ~24 km of movement, which caused the high-grade rocks of the High Himalayan Crystalline sequence to be exhumed and emplaced in direct contact with greenschist facies Tethyan sedimentary series. The structural evolution of the four structural domains combined record an evolution from pervasive thrusting during Himalayan orogenesis to localized normal movement focused on the Zanskar shear zone (Fig. 2; McElroy et al., 1990). Domain 2 encompasses the Zanskar shear zone, where normal shearing was localized to the top section of the High Himalayan Crystalline sequence, immediately below the Tethyan sedimentary series (Fig. 2). Evidence of thrust movement within domain 2 was presumably obliterated by high strain related to normal movement (Fig. 6). This high strain wanes both
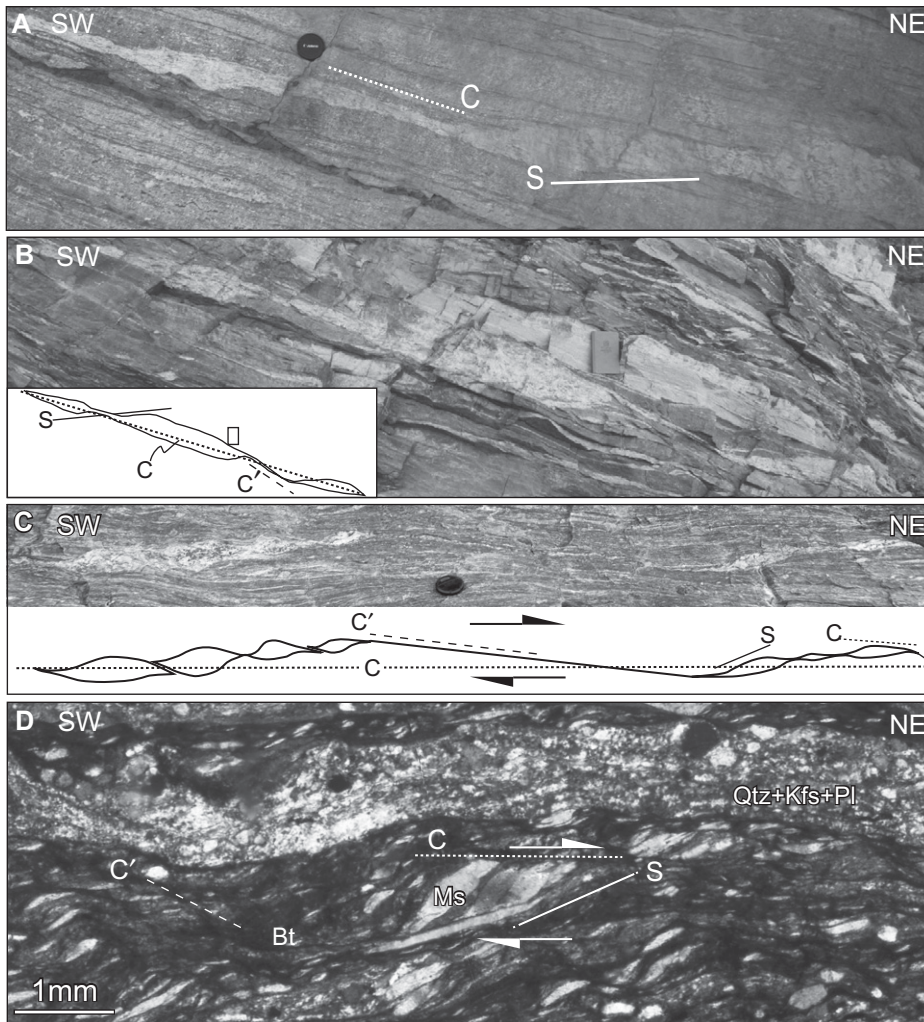
Figure 18. Shearing of leucogranitic dikes in domain 2a (locality ZNK55). (A) Leucogranite dike rotated toward the orientation of C through localized top-to-the-NE normal shearing on S-C planes. (B–C) Leucogranite dikes rotated into C through combined motion on top-to-the-NE S-C-C′ planes. (D) Photomicrograph equivalent of the mesoscale features shown in A–C and top-to-the-NE shearing of micaceous and leucogranitic layers in Kade orthogneiss. Asymmetric mica fish and alignment of fine-grained biotite define S, C, and C′ planes. Leucogranitic dikelet has been rotated into parallelism with shear plane (C) through combined shearing on S, C, and C′ planes. Mineral abbreviations after Kretz (1983).

toward the footwall (domain 1) and hanging wall (domains 3 and 4), and this is where overprinting relationships become well defined (Figs. 6, 7, and 10). Here, we discuss the nature of the overprinting relationship, its connection to melting, and the relative timing of the deformation switch and melting, and possible implications for the extrusion mechanism of the High Himalayan Crystalline sequence.

Regional Contact: Control on Shear Zone Localization and Leucogranite Intrusion

The domains described here record different expressions of the evolution of the Himalaya, beginning with thrusting, followed by inversion of the transport direction to normal movement focused on the Zanskar shear zone (Fig. 3). This is also where leucogranite intrusions accumulated at the time of normal shearing. Hodges et al. (1998) suggested that Himalayan leucogranites crosscut the South Tibetan detachment system in two regions in the central Himalaya, an interpretation that was subsequently contested by Searle and Godin (2003). In Zanskar, we have not observed any instance where leucogranites intrude the Tethyan sedimentary series. This could be: (1) because the leucogranites did not intrude the sedimentary rocks, presumably due to change in rheological properties from

the Kade orthogneiss to the Tethyan sedimentary series, or (2) because the region where they did intrude has been buried in the hanging wall by the shear zone. The fact that leucogranite intrusions continued in the High Himalayan Crystalline sequence where it was sheared by the Zanskar shear zone suggests that the contact between High Himalayan Crystalline sequence and Tethyan sedimentary series was a major rheological discontinuity, which controlled not only the localization of shearing to form the Zanskar shear zone, but also the upward extent of magma migration, leading to magma accumulation below the boundary.

Remnant Metamorphic Sequences Related to Thrusting

Within the larger-scale and dominant isograd distribution characterized by hot rocks of the High Himalayan Crystalline sequence below cold rocks of the Tethyan sedimentary series, we have identified a metamorphic series in two locations south of Gumburanjun dome where lower-grade rocks are found underneath higher-grade rocks. The lower-grade rocks are closest to the high-grade dome (Figs. 15 and 16). These two localities have metamorphic grades increasing upward, a pattern that is inconsistent with the right-way-up isograds (decreasing upward) that are dominant along the Zanskar shear zone and expected from normal shearing. We therefore interpret these two outcrops as representing remnant metamorphic sequences related to the earlier thrusting event, which placed hotter rocks on top of colder ones.

These two examples of inverted metamorphic series have been severely telescoped, with paragenesis equilibrated at temperatures differing by ~100 °C and 1 kbar (Fig. 17), usually separated by a few kilometers (Dézes, 1999) but now separated by just 75 m in one locality and ~20 m in the other (Fig. 15). While the metamorphic sequence is not associated with extension above the Gumburanjun dome, it has been physically overprinted by normal shearing at the dome's margins, and this is most likely responsible for the telescoping of preexisting isograds. This interpretation is consistent with the steep thermal gradient ubiquitously reported for the Zanskar shear zone due to thinning during normal shearing (e.g., Herren, 1987; Pognante, 1992; Dézes, 1999; Walker et al., 2001).

Inverted metamorphic gradients have been recognized above the Main Central thrust in Zanskar and have been attributed to large-scale, south-directed recumbent folding of the High Himalayan Crystalline sequence, overturning isograds above the Main Central thrust, while isograds immediately below the Zanskar

shear zone are right way up (Searle and Rex, 1989). The findings here suggest that inverted metamorphic isograds may be a more common feature of thrusting in the Zanskar Himalaya. We envisage the stacking of smaller thrust blocks, possibly repeated several times over the thickness of the High Himalayan Crystalline sequence, as a result of the sequential piling up of thrusted packages of rocks, each containing its own inverted metamorphic sequence.

This is the first instance of inverted metamorphic isograds recorded within the South Tibetan detachment system, and it suggests that steady-state geothermal gradients cannot be assumed when normal shearing started. Complexity in the tectono-thermal evolution of the metamorphic rocks predating the South Tibetan detachment system indicates that the isograds and their current distances are not a simple result of shearing and thinning of a preexisting steady-state, large-scale thermal structure. Rather they are the result of the early piling up of metamorphic rocks during thrusting—involving a thermal evolution of its own—which then got interrupted and overprinted by normal shearing. Thus, exhumation of the High Himalayan Crystalline sequence after initiation of normal shearing on the Zanskar shear zone led to a thermal evolution that overprinted an initially complex distribution of isotherms and isograds related to the earlier metamorphic history shuffled and distorted by thrusting. Thus, the total amount of movement on the Zanskar shear zone cannot be calculated using only the telescoping of metamorphic isograds, or thermal profiles derived from quartz CPOs (e.g., Herren, 1987; Dézes et al., 1999; Law et al., 2011).

Timing of Peak Metamorphism, Anatexis, and Switch in Movement Direction on Zanskar Shear Zone

Timing of metamorphism in the upper part of High Himalayan Crystalline sequence has been studied in detail by Walker et al. (1999; pelitic schist samples WAK 3, WAK 6, and WAK 9; U-Pb monazite, TIMS). These samples have monazite grains with ages reflecting early Paleozoic, pre-Himalayan metamorphism (ca. 490 Ma; Fig. 19). Our monazite geochronology results from both normally and reversely sheared leucogranite samples (ZNK119 and ZNK103A) yield a similar to slightly younger age range between ca. 494 and 360 Ma (Figs. 13, 14, and 19). However, because of the presence of the ca. 500–400 Ma Kade orthogneiss (Pognante and Lombardo, 1989; Pognante, 1992) and common appearance of these ages (sample ZNK119 yields only these ages), we suggest that these monazites are not inherited from surrounding
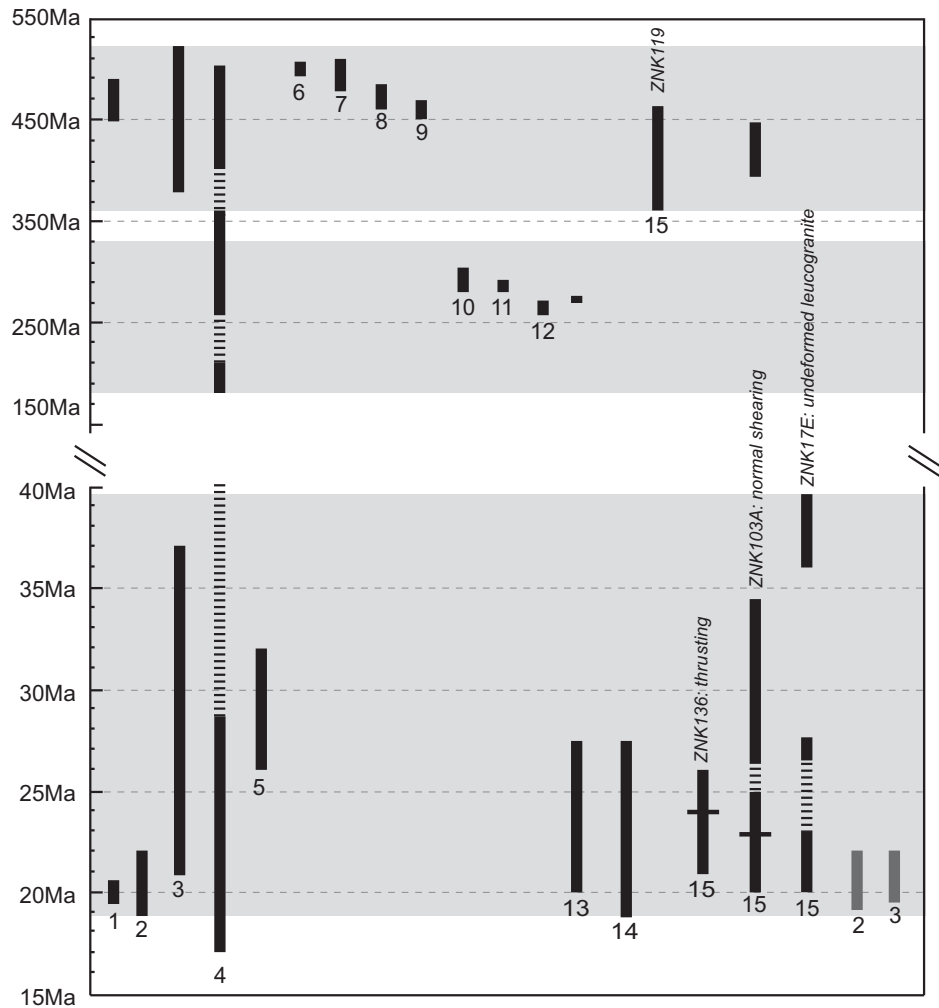
Figure 19. Summary of published geochronological data for Zanskar Range and Leo Pargil dome, together with our U-Pb monazite sensitive high-resolution ion microprobe (SHRIMP) results. Black lines are U-Pb monazite and zircon ages; gray lines are $^{40}Ar/^{39}Ar$ muscovite cooling ages. Plotted data are from: 1—Noble and Searle (1995), U-Pb monazite (SE Zanskar); 2—Dézes et al. (1999), U-Pb monazite and Ar/Ar muscovite (in gray; SE Zanskar); 3—Walker et al. (1999), U-Pb monazite, Ar/Ar muscovite (in gray; SE Zanskar); 4—Horton (2011), U-Pb monazite/zircon (SE Zanskar); 5—Vance and Harris (1999), Sm-Nd garnet (from NW Zanskar); 6—Mehta (1977), Rb-Sr whole rock (SE Zanskar); 7—Frank et al. (1977), Rb-Sr whole rock (SE Zanskar); 8—Pognante et al. (1990), U-Pb zircon (central Zanskar); 9—Stutz and Thöni (1987), Rb-Sr whole rock (NE Zanskar); 10—Honegger et al. (1982), Rb-Sr muscovite (NW Zanskar); 11—Inger (1998), Rb-Sr muscovite (central Zanskar); 12—Noble et al. (2001), U-Pb zircon (NW Zanskar); 13—Robyr et al. (2006), Th-Pb monazite (Gianbul dome); 14—Leech (2008), U-Pb zircon (Leo Pargil dome); 15—this study (SE Zanskar).

schists, but that they are inherited from the Kade orthogneiss.

In pelitic schist samples, Walker et al. (1999) also found ages between ca. 32 and 28 Ma (Fig. 19), which they interpreted as reflecting the age of prograde or near-peak Oligocene metamorphism. This is consistent with the ca. 33–26 Ma Sm-Nd garnet ages of Vance and Harris (1999) from central and western Zanskar, and with the

27.3 ± 1.2 Ma age (garnet-schist sample Z-40; U-Pb zircon) of Horton (2011) from Nun-Kun valley, to the east of Zanskar (Fig. 14). However, rather than defining a separate age group, there seems to be a continuum in ages from around 35 Ma to 20 Ma in the literature (Fig. 19).

Our analyses are broadly consistent with those of Walker et al. (1999), but we interpret them differently. First, leucosome sample

ZNK136 related to thrusting yielded ages between ca. 26 and 21 Ma with a weighted mean $^{206}Pb/^{238}U$ age of 24.0 ± 0.25 Ma (Figs. 13B–13D; Table 1). We disregard the mean age and interpret the values as recording a period of monazite growth or open-system behavior, and that some time during this period, there was the shift recorded in the rocks from anatexis during thrusting to the SW, to anatexis during normal movement to the NE. Similarly, Robyr et al. (2006) constrained onset of thrusting in the nearby Gianbul dome at 26.6 Ma (U-Pb monazite, TIMS). Rubatto et al. (2013) dated anatexis in Sikkim, NE Himalaya, and obtained a similar range of ages between ca. 31 and 17 Ma. They too disregarded the mean ages and argued that this age spread is real and corresponds to the long-lasting metamorphism in the region, with the higher structural levels reaching melting and peak condition later (26–23 Ma) than the lower structural levels (31–27 Ma). This is consistent with our interpretation that the weighted mean calculation yields an arbitrary mixed date.

Leucogranite sample ZNK103A, recording normal shearing in the Zanskar shear zone, yielded three groups of monazite ages: the old Cambrian–Ordovician ages (ca. 494–453 Ma) discussed previously, followed by ages between ca. 37 and 29 Ma, and finally the younger ages (Figs. 14A and 14C; Table 2). The older group (ca. 37 and 29 Ma) is similar to the Oligocene age range found by previous authors (Fig. 19). By combining these data with our structural observations, we suggest that these monazite U-Pb ages record the duration of the high-temperature event resulting from thrusting that peaked with anatexis recorded by the migmatites and intrusions in domain 1.

Leucogranites in the High Himalayan Crystalline sequence in Zanskar, including those from Gumburanjun, were previously dated at 24–17 Ma (Fig. 19; U-Pb monazite, zircon, uraninite; Dézes et al., 1999; Walker et al., 1999; Horton, 2011; Horton and Leech, 2013) and commonly included inherited monazite/zircon from the Kade orthogneiss and other older sources. Walker et al. (1999) also documented older ages of ca. 37–29 Ma (U-Pb monazite; TIMS; Fig. 19) in intensely deformed pegmatites (samples WAK21 and WAK26), which correspond to the age of metamorphic monazites from the surrounding pelitic schists. These authors suggested that these ages reflect a major thermal perturbation in the High Himalayan Crystalline sequence during the Oligocene.

We have documented leucogranites with the same mineralogy throughout all domains comprising rocks of the High Himalayan Crystalline sequence, where they record thrusting (domain 1, Fig. 4), normal movement, or are unsheared

(domain 2b, Fig. 8B). Our oldest sample (ZNK136) was interpreted to date thrusting and the change to normal shearing age between ca. 26 and 21 Ma. This contrasts with the age of our structurally youngest sample ZNK17E, from an undeformed dike crosscutting intensely foliated rocks of the Zanskar shear zone and with broad peak between 23 and 21.5 Ma, interpreted to indicate its crystallization age and to essentially postdate movement on the Zanskar shear zone.

The dominant monazite age group from the intensely normally sheared leucogranites in the Zanskar shear zone (the youngest age group in ZNK103A) yielded an age range between ca. 26 and 22 Ma, with average of 23.0 ± 0.8 Ma (Figs. 14C and 14D; Table 2). Given that there are a number of leucogranite ages reported in the literature from samples collected within the Zanskar shear zone that are between 23 and 21 Ma (Fig. 19; e.g., Dézes et al., 1999; Walker et al., 1999; Robyr et al., 2006; Horton, 2011; Horton and Leech, 2013), we take this age range as indicative of the timing of normal movement during intense magma generation and intrusion.

The waning stage of normal movement and magmatism is constrained not only by the ages of our undeformed leucogranite (ZNK17E) but also by other ages reported in the literature (Fig. 19). Walker et al. (1999) reported U-Pb monazite ages of 22.1 ± 0.4 Ma from a discordant leucogranite dike crosscutting sheared leucogranites (sample WAK27) from Gumburanjun. Horton (2011) reported an age of 20.3 ± 1.7 Ma for an undeformed pegmatite dike in Haptal valley (sample Z5: 33°27′4.20″N, 76°46′6.50″E, SE of domain 1). Altogether U-Pb dating constrains the end of deformation to between 23 and 19 Ma (Walker et al., 1999; Horton, 2011). Furthermore, muscovite $^{40}Ar/^{39}Ar$ ages from leucogranite samples at Gumburanjun indicate rapid cooling immediately after intrusion, with ages of ca. 20 Ma (Fig. 19; Dézes et al., 1999; Walker et al., 1999; Horton and Leech, 2013). We therefore take this age as marking the end of normal ductile shearing and magmatism. Rapid cooling and denudation immediately after intrusion of the youngest dikes have been also observed elsewhere in the Himalaya (e.g., Zeitler et al., 1993; Booth et al., 2009).

The overlapping age ranges of our samples, similar to other published age determinations for the area (Figs. 13, 14, and 19), may indicate that monazite grew semicontinuously during the peak period of the thermal event, possibly starting before the onset of anatexis and then continuing during anatexis, first accompanying thrusting followed by normal shearing. If so, each sample records monazite growth periods rather than absolute crystallization/cooling ages. Thus, while the samples do not provide

an absolute age for the switch from thrusting to normal movement, they bracket the maximum possible duration of normal shearing. As an upper bound, we take the oldest age recorded by monazites of the leucogranite in the normal shear zone, which coincides with the oldest age for the thrusted leucogranite at ca. 26 Ma. As a lower bound, we take the $^{40}Ar/^{39}Ar$ muscovite cooling ages of ca. 20 Ma, which is slightly younger than the youngest monazite age dated in the post-tectonic leucogranite sample ZNK17E (Fig. 19). This yields a maximum possible duration of ductile normal movement of ~6 m.y.

Gumburanjun Dome

The Gumburanjun dome is in the immediate vicinity of the much larger Gianbul dome, located northwest of domain 2b (Fig. 1A), with which it shares many similarities, such as being composed of orthogneiss intruded by leucogranites (Dézes et al., 1999; Robyr et al., 2002, 2006). This is also true for other gneiss domes ubiquitous through the High Himalaya, including the Mabja dome (Fig. 1A; Robyr et al., 2002; Lee et al., 2004; Aoya et al., 2005; Langille et al., 2010) and the Leo Pargil dome (Fig. 1A; Thiede et al., 2006; Langille et al., 2012). Like these, it developed during extension perpendicular to the trend of the Himalaya and consists of a core of gneissic or mylonitic leucogranite that is in normal shear or fault contact with overlying cover rocks. The foliation around these domes is parallel to the contact between the core and cover, with a downdip stretching lineation. The upper-crustal dome cover is displaced and commonly exhibits a decrease in metamorphic grade away from the dome. Metamorphic isograds in the dome cover are often closely spaced due to normal shearing and thinning at the dome margins (Lee et al., 2004).

Beaumont et al. (2004) inferred that one of the factors that controls extrusion of the High Himalayan Crystalline sequence through a midcrustal channel is a high rate of erosion. When the erosion rate is low and the upper crust is sufficiently weak, the High Himalayan Crystalline sequence may extrude as domes at a position more internal to the orogen. While this may appear to be a viable explanation for exhumation in the NW Himalaya, our results suggest otherwise. The absence of high-grade rocks at the Main Central thrust (Robyr et al., 2006) suggests that wholesale tunneling and exhumation of the High Himalayan Crystalline sequence did not occur. Combined with the relatively short duration of normal movement (6 m.y.) constrained here, we argue that exhumation in the NW Himalaya by means

of large-scale domes, such as the Gumburanjun and Gianbul domes (Robyr et al., 2002), is unrelated to channel flow.

Normal Movement, Strain Rate, and Crustal Weakening

We argue that the initiation of anatexis and increase in melt fraction in the High Himalayan Crystalline sequence in the Oligocene (some time before 26 Ma) weakened the crust and triggered the initiation of normal movement some time between 26 and 20 Ma. The conclusion that synthrusting anatexis preceded normal movement implies that melting did not result from decompression due to normal shearing, and was possibly the actual cause of relaxation of the system and initiation of normal movement. While it is currently not possible to constrain either the melt fraction or the thickness of the anatectic layer through time, we note that the presence of only a few volume percent of melt can halve the strength of rocks (Rosenberg and Handy, 2005). The suggestion that anatexis and accompanying crustal weakening triggered the switch in deformation is further supported by the fact that normal movement simply inverted the sense of movement from top-to-the-SW thrusting to top-to-the-NE normal shearing, indicative of a simple swap between the maximum shortening and maximum extension strain axes, without a change in their orientation.

Bringing the results together, we propose that during ductile thrusting of the Tethyan sedimentary series to the SW over the High Himalayan Crystalline sequence, crustal thickening caused increased temperatures and melting of the High Himalayan Crystalline sequence. Anatexis caused crustal weakening and a switch in movement sense, with normal movement localized at the regional contact between the High Himalayan Crystalline sequence and Tethyan sedimentary series. Decompression may have boosted the melting, increasing the melt fraction and leucogranites accumulated at this regional boundary, doming the Gumburanjun area. Exhumation driven by normal movement led to cooling of the crust and termination of the anatectic event (e.g., Dézes et al., 1999; Walker et al., 1999; Aoya et al., 2005) and brittle-ductile normal faults overprinting ductile deformation. Normal shearing overprinted the early isograds and led to the telescoping of the early metamorphic isograds related to thrusting, as preserved locally in lithons close to Gumburanjun dome (Figs. 15 and 16). Thus, structures and metamorphism record an evolution from hot conditions during thrusting to cooling as the High Himalayan Crystalline sequence was exhumed along the detachment. Finally, we can estimate

the minimum strain rate during normal movement by dividing the strain of 28.6 estimated herein by the 6 m.y. maximum duration of normal fault movement, yielding $\sim 1.5 \times 10^{-13}$ s^{-1}.

Channel Flow: Implications

It has been suggested that the High Himalayan Crystalline series may have been extruded from underneath the Tibetan Plateau as a result of channel flow (Grujic et al., 1996; Beaumont et al., 2001). In this model, the High Himalayan Crystalline sequence would have channeled toward the Himalayan front due to pressure gradients resulting from the high topography of the Tibetan Plateau. The channel would have extruded through a combination of movement on two subparallel shear zones with opposite senses of shear: the Main Central thrust at the base, and the South Tibetan detachment at the top. These would have operated contemporaneously over an extended period of time (Hodges, 2000; Godin et al., 2006) and were assisted by erosion to allow for continued channeling of the High Himalayan Crystalline sequence.

As summarized by Grujic (2006), there was a change from burial to exhumation of the High Himalayan Crystalline sequence (Greater Himalaya sequence) reflected in the change in shear sense along the upper bounding shear zone, from southward thrusting to northward normal movement, of the kind reported and constrained temporally in this paper. It has been demonstrated in Bhutan (Chambers, 2008; Chambers et al., 2009), Nepal (Hodges et al., 1996), and now also in Zanskar, that this occurred at or after ca. 24 Ma. Anatexis accompanied normal movement and exhumation of the High Himalayan Crystalline sequence (Grujic et al., 1996, 2002; Davidson et al., 1997; Daniel et al., 2003; Harris et al., 2004; Sachan et al., 2010). While this is also the case in Zanskar, our structural study indicates that anatexis started during thrusting and finished soon after inception of normal movement (for the Garhwal Himalaya, see Sachan et al., 2010).

The contemporaneity of thrusting and normal faulting above and below the High Himalayan Crystalline series, and of Miocene peak metamorphism and anatexis, has been demonstrated by structural studies and geochronology (Burchfiel et al., 1992; Hodges et al., 1992, 1998; but see also Murphy and Harrison, 1999). Geochronological evidence indicates continued movement on the Main Central thrust until a few million years ago (e.g., Harrison et al. 1997; Catlos et al., 2002), with estimates of reverse movement between a minimum of several tens of kilometers and a maximum of 150–

250 km (Brunel and Kienast, 1986). This contrasts with the duration of normal movement on the South Tibetan detachment, constrained here for the Zanskar shear zone to between ca. 26 Ma and 21–20 Ma, similar to estimates for the Garhwal Himalaya (Sachan et al., 2010) and for the Everest area, where the ductile strands of the South Tibetan detachment were active at 18–16 Ma, and the upper brittle strands were active at less than 16 Ma (Searle et al., 2003; see also Hodges et al., 1998; Murphy and Harrison, 1999).

Quantitative constraints on minimum normal-sense dip-slip displacement are available for three regions of the South Tibetan detachment system. In Zanskar, cumulative normal sense displacement has been estimated based on the thinning of metamorphic isograds to a minimum of between 25 km and possibly 35 km (Herren, 1987; Dézes, 1999) or based on strain estimates (this paper; Herren, 1987). To the north of Everest, minimum dip-slip displacement on the South Tibetan detachment was estimated at 35–40 km (Burchfiel et al., 1992; Hodges et al., 1998), and may have exceeded 90–100 km (Searle et al., 2003). In the eastern Himalaya of Bhutan, structural overlap between the Tethyan sedimentary rocks and the Higher Himalayan Crystalline sequence (Grujic et al., 2002) suggests minimum normal displacement of 140 km.

Grujic (2006) listed a number of potentially diagnostic geological features expected of channel flow, for example: (1) the existence of two (sub)parallel shear zones with opposite shear sense bounding the high-grade rocks of the High Himalayan Crystalline series, (2) syntectonic partial melt of the high-grade rocks to create a weak channel between strong crustal layers, (3) inversion of shear sense from thrusting to normal movement in the roof of the channel, (4) jump in metamorphic conditions across channel boundaries, such as the change from upper-amphibolite or granulite facies to greenschist facies across the Zanskar shear zone, and (5) existence of a strong orographic, focused erosion of the rocks extruded in the channel.

Despite the presence of all these elements in Zanskar, there are two key elements missing: time and total displacement. The brief period of normal movement and the relatively small total normal movement on the Zanskar shear zone suggest that the extrusion of the High Himalayan Crystalline sequence as a channel would have required tens of millions of years and significant total movement along the bounding shear zones (see Godin et al., 2006). We propose instead that mechanical weakening of the midcrust due to anatexis caused a decrease in the critical taper angle of the thrust front of

the orogeny (e.g., Dahlen, 1990; England and Molnar, 1993; Northrup, 1996). Normal movement, lasting a few million years, allowed a decrease in the taper angle and exhumation and cooling of the anatectic core of the thrust front (see also Sachan et al., 2010; Chambers et al., 2011).

CONCLUSION

The Zanskar shear zone is a ductile, normal shear zone that overprints and reactivates earlier thrust planes. The Zanskar shear zone developed at the contact between the Kade orthogneiss at the top of the High Himalayan Crystalline series and the Tethyan sedimentary series. Leucogranites accumulated at this contact, as did strain, locally forming domes such as the Gumburanjun dome. The thickness of the Zanskar shear zone varies from ~1 km (current study; Dézes et al., 1999) to 6.75 km (Herren, 1987). Strain analysis indicates that the Zanskar shear zone accommodated ~24 km of movement, which exhumed the granulite and upper-amphibolite facies rocks of the High Himalayan Crystalline sequence, placing them in direct contact with greenschist facies Tethyan sedimentary series rocks. The normal and thrust shear planes and movement directions are parallel to each other but have opposite transport directions, suggesting a simple swap between the x and z strain axes. Melting commenced during thrusting and ended after normal shearing. We suggest that crustal anatexis weakened the upper crust, eventually causing the switch in transport direction and the onset of normal shearing. This switch must have occurred between 26 and 20 Ma, i.e., the estimated age range of leucogranitic intrusions. Normal shearing initially caused a boost in melt generation due to decompression, followed by exhumation, cooling, and the telescoping of right-way-up isograds, with cool rocks above hot rocks. However, lithons of Barrovian metamorphic series representative of metamorphism during thrusting are preserved. They record an inverted metamorphism with the lowest-grade, biotite zone rocks closest to the intrusion zone in the footwall of the shear zone, and the highest-grade, kyanite zone rocks toward the hanging wall. This inverted metamorphism was overprinted by normal shearing, which caused the telescoping of thrust-related isograds. Given the short duration and small amount of total normal movement, we find little support for the hypothesis of channel flow. We postulate that Miocene anatexis was the cause of the switch from thrusting to normal fault movement, due to crustal weakening and a decrease in the critical taper angle of the thrust front of the orogeny.

REFERENCES CITED

Aleinikoff, J.N., Schenck, W.S., Plank, M.O., Srogi, L., Fanning, C.M., Kamo, S.L., and Bosbyshell, H., 2006, Deciphering igneous and metamorphic events in high-grade rocks of the Wilmington Complex, Delaware: Morphology, cathodoluminescence and backscattered electron zoning, and SHRIMP U-Pb geochronology of zircon and monazite: Geological Society of America Bulletin, v. 118, p. 39–64, doi:10.1130/B25659.1.

Aoya, M., Wallis, S.R., Terada, K., Lee, J., Kawakami, T., Wang, Y., and Heizler, M., 2005, North-south extension in the Tibetan crust triggered by granite emplacement: Geology, v. 33, p. 853–856, doi:10.1130/G21806.1.

Beaumont, C., Jamieson, R.A., Nguyen, M.H., and Lee, B., 2001, Himalayan tectonics explained by extrusion of a low-viscosity crustal channel coupled to focused surface denudation: Nature, v. 414, p. 738–742, doi:10.1038/414738a.

Beaumont, C., Jamieson, R.A., Nguyen, M.H., and Medvedev, S., 2004, Crustal channel flows: 1. Numerical models with applications to the tectonics of the Himalayan-Tibetan orogen: Journal of Geophysical Research, v. 109, B06406, doi:10.1029/2003JB002809.

Beaumont, C., Nguyen, M.H., Jamieson, R.A., and Ellis, S., 2006, Crustal flow models in large hot orogens, *in* Law, R.D., Searle, M.P., and Godin, L., eds., Channel Flow, Ductile Extrusion and Exhumation in Continental Collision Zones: Geological Society of London Special Publication 268, p. 91–145.

Booth, A.L., Chamberlain, C.P., Kidd, W.S.F., and Zeitler, P.K., 2009, Constraints on the metamorphic evolution of the eastern Himalayan syntaxis from geochronologic and petrologic studies of Hamche Barwa: Geological Society of America Bulletin, v. 121, p. 385–407, doi:10.1130/B26041.1.

Brunel, M., and Kienast, J.-R., 1986, Etude petrostructurale des chevauchements ductiles himalayens sur la transversale de l'Everest-Makalu (Nepal oriental): Canadian Journal of Earth Sciences, v. 23, p. 1117–1137, doi:10.1139/e86-111.

Burchfiel, B.C., and Royden, L.H., 1985, North-south extension within the convergent Himalayan region: Geology, v. 13, p. 679–682, doi:10.1130/0091-7613(1985)13<679:NEWTCH>2.0.CO;2.

Burchfiel, B.C., Chen, Z., Hodges, K.V., Liu, Y., Royden, L.H., Deng, C., and Xu, J., 1992, The South Tibetan Detachment System, Himalayan Orogen: Extension Contemporaneous with and Parallel to Shortening in a Collisional Mountain Belt: Geological Society of America Special Paper 269, 41 p., doi:10.1130/SPE269-p1.

Burg, J.P., and Chen, G.M., 1984, Tectonics and structural zonation of southern Tibet, China: Nature, v. 311, p. 219–223, doi:10.1038/311219a0.

Catlos, E.J., Harrison, M.T., Manning, C.E., Grove, M., Rai, S.M., Hubbard, M.S., and Upreti, B.N., 2002, Records of the evolution of the Himalayan orogen from in situ Th-Pb ion microprobe dating of monazite: Eastern Nepal and western Garhwal: Journal of Asian Earth Sciences, v. 20, p. 459–479, doi:10.1016/S1367-9120 (01)00039-6.

Chambers, J.A., 2008, Thermal Evolution of the Mid-Crust from the Himalayan Orogen [Ph.D. thesis]: Milton-Keynes, UK, Open University, 304 p.

Chambers, J.A., Parrish, R.R., Argles, T., Harris, N., and Horstwood, M., 2009, Geochronological and micro-fabric constraints on pulsed extrusion of the metamorphic core in the eastern Himalaya (Bhutan): Geological Society of America Abstracts with Programs, v. 41, no. 7, p. 586.

Chambers, J.A., Parrish, R.R., Argles, T., and Harris, N., 2011, A short duration pulse of ductile normal shear on the outer South Tibetan detachment in Bhutan: Alternating channel flow and critical taper mechanics of the eastern Himalaya: Tectonics, v. 30, p. 1–12, doi:10.1029/2010TC002784.

Cheney, J.T., Alexander, A., Webb, G., Coath, C.D., and McKeegan, K.D., 2004, In situ ion microprobe [207]Pb/[206]Pb dating of monazite from Precambrian metamorphic suites, Tobacco Root Mountains, Montana, *in* Brady, J.B., Burger, H.R., Cheney, J.T., and Harms, T.A., eds., Precambrian Geology of the Tobacco Root Mountains, Montana: Geological Society of America Special Paper 377, p. 151–179, doi:10.1130/0-8137-2377-9.151.

Coggon, R., and Holland, T.J.B., 2002, Mixing properties of phengitic micas and revised garnet-phengite thermobarometers: Journal of Metamorphic Geology, v. 20, p. 683–696, doi:10.1046/j.1525-1314.2002.00395.x.

Coleman, M.E., 1998, U-Pb constraints on Oligocene-Miocene deformation and anatexis within the Central Himalaya, Marsyandi Valley, Nepal: American Journal of Science, v. 298, p. 553–571, doi:10.2475/ajs.298.7.553.

Cottle, J.M., Jessup, M.J., Newell, D.L., Searle, M.P., Law, R.D., and Horstwood, M., 2007, Structural insights into the early stages of exhumation along an orogen-scale detachment: The South Tibetan detachment system, Dzakaa Chu section, eastern Himalaya: Journal of Structural Geology, v. 29, p. 1781–1797, doi:10.1016/j.jsg.2007.08.007.

Dahlen, F.A., 1990, Critical taper model of fold-and-thrust belts and accretionary wedges: Annual Review of Earth and Planetary Sciences, v. 18, p. 55–99, doi:10.1146/annurev.ea.18.050190.000415.

Daniel, C.G., Hollister, L.S., Parrish, R.R., and Grujic, D., 2003, Exhumation of the Main Central thrust from lower crustal depths, eastern Bhutan Himalaya: Journal of Metamorphic Geology, v. 21, p. 317–334, doi:10.1046/j.1525-1314.2003.00445.x.

Davidson, C., Grujic, D.E., Hollister, L.S., and Schmid, S.M., 1997, Metamorphic reactions related to decompression and synkinematic intrusion of leucogranite, High Himalayan Crystallines, Bhutan: Journal of Metamorphic Geology, v. 15, no. 5, p. 593–612, doi:10.1111/j.1525-1314.1997.tb00638.x.

Dézes, P., 1999, Tectonic and Metamorphic Evolution of the Central Himalayan Domain in Southeast Zanskar (Kashmir, India) [Ph.D. thesis]: Lausanne, Switzerland, University of Lausanne, 149 p.

Dézes, P.J., Vannay, J.-C., Steck, A., Bussy, F., and Cosca, M., 1999, Synorogenic extension: Quantitative constraints on the age and displacement of the Zanskar shear zone (northwest Himalaya): Geological Society of America Bulletin, v. 111, p. 364–374, doi:10.1130/0016-7606(1999)111<0364:SEQCOT>2.3.CO;2.

England, P., and Molnar, P., 1993, Cause and effect among thrust and normal faulting, anatectic melting and exhumation in the Himalaya, *in* Treloar, P.J., and Searle, M.P., eds., Himalayan Tectonics: Geological Society of London Special Publication 74, p. 401–411.

Fitzgerald, J., and Stünitz, H., 1993, Deformation of granitoids at low metamorphic grade. I: Reactions and grain size reduction: Tectonophysics, v. 221, p. 299–324, doi:10.1016/0040-1951(93)90164-F.

Frank, W., Thoni, M., and Purtscheller, F., 1977, Geology and petrography of Kulu-South Lahoul area: Ecologie et geologie de l'Himalaya: Colloques Internationaux de Centre National de la Recherche Scientifique, v. 268, p. 147–166.

Fuchs, G., 1987, The geology of southern Zanskar (Ladakh); evidence for the autochthony of the Tethys zone of the Himalaya: Jahrbuch der Geologischen Bundesanstalt Wien, v. 130, p. 465–491.

Godin, L., Grujic, D., Law, R.D., and Searle, M.P., 2006, Channel flow, ductile extrusion and exhumation in continental collision zones: An introduction, *in* Law, R.D., Searle, M.P., and Godin, L., eds., Channel Flow, Ductile Extrusion and Exhumation in Continental Collision

Zones: Geological Society of London Special Publication 268, p. 1–23.

Grujic, D., 2006, Channel flow and continental collision tectonics: An overview, *in* Law, R.D., Searle, M.P., and Godin, L., eds., Channel Flow, Ductile Extrusion and Exhumation in Continental Collision Zones: Geological Society of London Special Publication 268, p. 25–37.

Grujic, D., Casey, M., Davidson, C., Hollister, L.S., Kündig, R., Pavlis, T., and Schmid, S., 1996, Ductile extrusion of the Higher Himalayan Crystalline in Bhutan: Evidence from quartz microfabrics: Tectonophysics, v. 260, p. 21–43, doi:10.1016/0040-1951(96)00074-1.

Grujic, D., Hollister, L.S., and Parrish, R., 2002, Himalayan metamorphic sequence as an orogenic channel: Insight from Bhutan: Earth and Planetary Science Letters, v. 198, p. 177–191, doi:10.1016/S0012-821X(02)00482-X.

Guillot, S., Hodges, K., Le Fort, P., and Pêcher, A., 1994, New constraints on the age of the Manaslu leucogranite: Evidence for episodic tectonic denudation in the central Himalayas: Geology, v. 22, p. 559–562, doi:10.1130/0091-7613(1994)022<0559:NCOTAO>2.3.CO;2.

Harris, N., Caddick, M., Košler, J., Goswami, S., Vance, D., and Tindle, A.G., 2004, The pressure-temperature-time path of migmatites from the Sikkim Himalaya: Journal of Metamorphic Geology, v. 22, p. 249–264, doi:10.1111/j.1525-1314.2004.00511.x.

Harrison, M.T., Ryerson, F.J., Le Fort, P., Yin, A., Lovera, O.M., and Catlos, E.J., 1997, A late Miocene–Pliocene origin for the Central Himalayan inverted metamorphism: Earth and Planetary Science Letters, v. 146, no. 1–2, p. E1–E7, doi:10.1016/S0012-821X(96)00215-4.

Harrison, T.M., Grove, M., Lovera, O.M., and Catlos, E.J., 1998, A model for the origin of Himalayan anatexis and inverted metamorphism: Journal of Geophysical Research, v. 103, p. 27,017–27,032, doi:10.1029/98JB02468.

Harrison, T.M., Grove, M., McKeegan, K.D., Coath, C.D., Lovera, O.M., and Le Fort, P., 1999, Origin and episodic emplacement of the Manaslu intrusive complex, Central Himalaya: Journal of Petrology, v. 40, p. 3–19, doi:10.1093/petroj/40.1.3.

Hawkins, D.P., and Bowring, S.A., 1997, U-Pb systematics of monazite and xenotime: Case studies from the Paleoproterozoic of the Grand Canyon, Arizona: Contributions to Mineralogy and Petrology, v. 127, p. 87–103, doi:10.1007/s004100050267.

Herren, E., 1987, Zanskar shear zone: Northeast-southwest extension within the Higher Himalayas (Ladakh, India): Geology, v. 15, p. 409–413, doi:10.1130/0091-7613(1987)15<409:ZSZNEW>2.0.CO;2.

Hodges, K., Bowring, S., Davidek, K., Hawkins, D., and Krol, M., 1998, Evidence for rapid displacement on Himalayan normal faults and the importance of tectonic denudation in the evolution of mountain ranges: Geology, v. 26, p. 483–486, doi:10.1130/0091-7613(1998)026<0483:EFRDOH>2.3.CO;2.

Hodges, K.V., 2000, Tectonics of the Himalaya and southern Tibet from two perspectives: Geological Society of America Bulletin, v. 112, p. 324–350, doi:10.1130/0016-7606(2000)112<324:TOTHAS>2.0.CO;2.

Hodges, K.V., Parrish, R.R., Housh, T.B., Lux, D.R., Burchfiel, B.C., Royden, L.H., and Chen, Z., 1992, Simultaneous Miocene extension and shortening in the Himalayan orogen: Science, v. 258, p. 1466–1470, doi:10.1126/science.258.5087.1466.

Hodges, K.V., Parrish, R.R., and Searle, M.P., 1996, Tectonic evolution of the central Annapurna Range, Nepalese Himalayas: Tectonics, v. 15, p. 1264–1291, doi:10.1029/96TC01791.

Holland, T.J.B., and Powell, R., 1998, An internally consistent thermodynamic data set for phases of petrological interest: Journal of Metamorphic Geology, v. 16, p. 309–343, doi:10.1111/j.1525-1314.1998.00140.x.

Holland, T.J.B., and Powell, R., 2003, Activity-composition relations for phases in petrological calculations: An asymmetric multicomponent formulation: Contributions to Mineralogy and Petrology, v. 145, p. 492–501, doi:10.1007/s00410-003-0464-z.

Honegger, K., Dietrich, V., Frank, W., Gansser, A., Thöni, M., and Trommsdorff, V., 1982, Magmatism and metamorphism in the Ladakh Himalayas (the Indus-Tsangpo suture zone): Earth and Planetary Science Letters, v. 60, p. 253–292, doi:10.1016/0012-821X(82)90007-3.

Horton, F., and Leech, M.L., 2013, Age and origin of granites in the Karakoram shear zone and Greater Himalaya Sequence, NW India: Lithosphere, v. 5, p. 300–320, doi:10.1130/L213.1.

Horton, F.M., 2011, Geochronology and Zircon Geochemistry of Greater Himalaya Leucogranites in Zanskar, NW India [M.Sc. thesis]: San Francisco, California, San Francisco State University, 104 p.

Hurtado, J.M., Hodges, K., and Whipple, K.X., 2001, Neotectonics of the Thakkhola graben and implications for recent activity on the South Tibetan fault system in the central Nepal Himalaya: Geological Society of America Bulletin, v. 113, p. 222–240, doi:10.1130/0016-7606(2001)113<0222:NOTTGA>2.0.CO;2.

Inger, S., 1998, Timing of an extensional detachment during convergent orogeny: New Rb-Sr geochronological data from the Zanskar shear zone, northwestern Himalaya: Geology, v. 26, p. 223–226, doi:10.1130/0091-7613(1998)026<0223:TOAEDD>2.3.CO;2.

Jamieson, R.A., Beaumont, C., Medvedev, S., and Nguyen, M.H., 2004, Crustal channel flows: 2. Numerical models with implications for metamorphism in the Himalayan-Tibetan orogen: Journal of Geophysical Research, v. 109, B06407, doi:10.1029/2003JB002811.

Jamieson, R.A., Beaumont, C., Nguyen, M.H., and Grujic, D., 2006, Provenance of the Greater Himalayan Sequence and associated rocks: Predictions of channel flow models, *in* Law, R.D., Searle, M.P., and Godin, L, eds., Channel Flow, Ductile Extrusion and Exhumation in Continental Collision Zones: Geological Society of London Special Publication 268, p. 165–182.

Jessup, M.J., Law, R.D., Searle, M.P., and Hubbard, M.S., 2006, Structural evolution and vorticity of flow during extrusion and exhumation of the Greater Himalayan slab, Mount Everest Massif, Tibet/Nepal: Implications for orogen-scale flow partitioning, *in* Law, R.D., Searle, M.P., and Godin, L, eds., Channel Flow, Ductile Extrusion and Exhumation in Continental Collision Zones: Geological Society of London Special Publication 268, p. 379–413.

Kellett, D.A., and Godin, L., 2009, Pre-Miocene deformation of the Himalayan superstructure, Hidden Valley, central Nepal: Journal of the Geological Society of London, v. 166, p. 261–275, doi:10.1144/0016-76492008-097.

Kellett, D.A., and Grujic, D., 2012, New insight into the South Tibetan detachment system: Not a single progressive deformation: Tectonics, v. 31, TC2007, doi:10.1029/2011TC002957.

Kretz, R., 1983, Symbols for rock-forming minerals: The American Mineralogist, v. 68, p. 277–279.

Kruhl, J.H., 1998, Reply: Prism- and basal-plane parallel subgrain boundaries in quartz: A microstructural geothermobarometer: Journal of Metamorphic Geology, v. 16, p. 142–146.

Langille, J., Lee, J., Hacker, B., and Seward, G., 2010, Middle crustal ductile deformation patterns in southern Tibet: Insights from vorticity studies in Mabja dome: Journal of Structural Geology, v. 32, p. 70–85, doi:10.1016/j.jsg.2009.08.009.

Langille, J.M., Jessup, M.J., Cottle, J.M., Lederer, G., and Ahmad, T., 2012, Timing of metamorphism, melting and exhumation of the Leo Pargil dome, northwest India: Journal of Metamorphic Geology, v. 30, p. 769–791, doi:10.1111/j.1525-1314.2012.00998.x.

Larson, K.P., and Godin, L., 2009, Kinematics of the Greater Himalayan sequence, Dhaulagiri Himal: Implications for the structural framework of central Nepal: Journal of the Geological Society of London, v. 166, p. 25–43, doi:10.1144/0016-76492007-180.

Law, R.D., Searle, M.P., and Simpson, R.L., 2004, Strain, deformation temperatures and vorticity of flow at the top of the Greater Himalayan slab, Everest Massif, Tibet: Journal of the Geological Society of London, v. 161, p. 305–320, doi:10.1144/0016-764903-047.

Law, R.D., Jessup, M.J., Searle, M.P., Francsis, M.K., Waters, D.J., and Cottle, J.M., 2011, Telescoping of isotherms beneath the South Tibetan detachment system, Mount Everest Massif: Journal of Structural Geology, v. 33, p. 1569–1594, doi:10.1016/j.jsg.2011.09.004.

Lee, J., Hacker, B., and Wang, Y., 2004, Evolution of North Himalayan gneiss domes: Structural and metamorphic studies in Mabja dome, southern Tibet: Journal of Structural Geology, v. 26, p. 2297–2316, doi:10.1016/j.jsg.2004.02.013.

Lee, J., McClelland, W., Wang, Y., Blythe, A., and McWilliams, M., 2006, Oligocene-Miocene middle crustal flow in southern Tibet: Geochronology of Mabja dome, *in* Law, R.D., Searle, M.P., and Godin, L, eds., Channel Flow, Ductile Extrusion and Exhumation in Continental Collision Zones: Geological Society of London Special Publication 268, p. 445–469.

Leech, M.L., 2008, Does the Karakoram fault interrupt mid-crustal channel flow in the western Himalaya?: Earth and Planetary Sciences, v. 276, p. 314–322, doi:10.1016/j.epsl.2008.10.006.

Le Fort, P., Cuney, M., Deniel, C., France-Lanord, C., Sheppard, S.M.F., Upreti, B.N., and Vidal, P., 1987, Crustal generation of the Himalayan leucogranites: Tectonophysics, v. 134, p. 39–57, doi:10.1016/0040-1951(87)90248-4.

Long, S., and McQuarrie, N., 2010, Placing limits on channel flow: Insights from the Bhutan Himalaya: Earth and Planetary Science Letters, v. 290, p. 375–390, doi:10.1016/j.epsl.2009.12.033.

Ludwig, K.R., 2001, Squid, Version 1.02: A User's Manual: Berkeley Geochronology Center Special Publication 2, 21 p.

Ludwig, K.R., 2003, ISOPLOT 3.0—A Geochemical Toolkit for Microsoft Excel: Berkeley Geochronology Center Special Publication, v. 4, p. 1–70.

Mahar, E.M., Baker, J.M., Powell, R., Holland, T.J.B., and Howell, N., 1997, The effect of Mn on mineral stability in metapelites: Journal of Metamorphic Geology, v. 15, p. 223–238, doi:10.1111/j.1525-1314.1997.00011.x.

McElroy, R., Cater, J., Roberts, I., Peckham, A., and Bond, M., 1990, The structure and stratigraphy of SE Zanskar, Ladakh Himalaya: Journal of the Geological Society of London, v. 147, p. 989–997, doi:10.1144/gsjgs.147.6.0989.

Mehta, P.K., 1977, Rb-Sr geochronology of the Kulu-Mandi belt: Its implications for the Himalayan tectonogenesis: Geologische Rundschau, v. 66, p. 156–175, doi:10.1007/BF01989570.

Mukherjee, S., and Koyi, H.A., 2010, Higher Himalayan shear zone, Zanskar Indian Himalaya: Microstructural studies and extrusion mechanism by a combination of simple shear and channel flow: International Journal of Earth Sciences, v. 99, no. 5, p. 1083–1110, doi:10.1007/s00531-009-0447-z.

Murphy, M.A., and Harrison, M.T., 1999, Relationship between leucogranites and the Qomolangma detachment in the Rongbuk Valley, south Tibet: Geology, v. 27, p. 831–834, doi:10.1130/0091-7613(1999)027<0831:RBLATQ>2.3.CO;2.

Nanda, M.M., and Singh, M.P., 1976, Stratigraphy and sedimentation of the Zanskar area, Ladakh and adjoining parts of the Lauhaul region of Himachal Pradesh, *in* Nautiyal, S., ed., Himalayan Geology, p. 365–388.

Noble, S.R., and Searle, M.P., 1995, Age of crustal melting and leucogranite formation from U-Pb zircon and monazite dating in the western Himalaya, Zanskar, India: Geology, v. 23, p. 1135–1138, doi:10.1130/0091-7613(1995)023<1135:AOCMAL>2.3.CO;2.

Noble, S.R., Searle, M.P., and Walker, C.B., 2001, Age and tectonic significance of Permian granites in western Zanskar, High Himalaya: The Journal of Geology, v. 109, p. 127–135, doi:10.1086/317966.

Northrup, C.J., 1996, Structural expressions and tectonic implications of general noncoaxial flow in the midcrust of a collisional orogen: The northern Scandinavian Caledonides: Tectonics, v. 15, p. 490–505, doi:10.1029/95TC02951.

Parrish, R.R., 1990, U-Pb dating of monazite and its application to geological problems: Canadian Journal of Earth Sciences, v. 27, p. 1431–1450, doi:10.1139/e90-152.

Passchier, C.W., and Trouw, R.A.J., 2005, Microtectonics: Berlin, Springer-Verlag, 366 p.

Patel, R.C., Singh, S., Asokan, A., Manickavasagam, R.M., and Jain, A.K., 1993, Extensional tectonics in the Himalayan orogen, Zanskar, NW India, *in* Treloar, P.J., and Searle, M.P., eds., Himalayan Tectonics: Geological Society of London Special Publication 74, p. 445–459.

Paterson, S.R., Vernon, R.H., and Tobisch, O.T., 1989, A review of criteria for the identification of magmatic and tectonic foliations in granitoids: Journal of Structural Geology, v. 11, p. 349–363, doi:10.1016/0191-8141 (89)90074-6.

Peternell, M., Hasalová, P., Wilson, C.J.L., Piazolo, S., and Schulmann, K., 2010, Evaluating quartz crystallographic preferred orientations and the role of deformation partitioning using EBSD and fabric analyser techniques: Journal of Structural Geology, v. 32, p. 803–817, doi:10.1016/j.jsg.2010.05.007.

Pognante, U., 1992, Migmatites and leucogranites of Tertiary age from the High Himalayan Crystallines of Zanskar (NW India): A case history of anatexis of Palaeozoic orthogneisses: Mineralogy and Petrology, v. 46, p. 291–313, doi:10.1007/BF01173569.

Pognante, U., and Lombardo, B., 1989, Metamorphic evolution of the High Himalayan Crystallines in SE Zanskar, India: Journal of Metamorphic Geology, v. 7, p. 9–17, doi:10.1111/j.1525-1314.1989.tb00571.x.

Pognante, U., Castelli, D., Benna, P., Genovese, G., Oberli, F., Meier, M., and Tonarini, S., 1990, The crystalline units of the High Himalayas in the Lahul, Zanskar region (northwest India): Metamorphic, tectonic history and geochronology of the collided and imbricated Indian plate: Geological Magazine, v. 127, p. 101–116, doi:10.1017/S0016756800013807.

Powell, R., Holland, T., and Worley, B., 1998, Calculating phase diagrams involving solid solutions via non-linear equations with examples using THERMOCALC: Journal of Metamorphic Geology, v. 16, p. 577–588, doi:10.1111/j.1525-1314.1998.00157.x.

Powell, R., Guiraud, M., and White, R.W., 2005, Truth and beauty in metamorphic phase equilibria: Conjugate variables and phase diagrams: Canadian Mineralogist, v. 43, p. 21–33, doi:10.2113/gscanmin.43.1.21.

Ramsay, J.G., and Graham, R.H., 1970, Strain variation in shear belts: Canadian Journal of Earth Sciences, v. 7, p. 786–813, doi:10.1139/e70-078.

Robyr, M., Vannay, J.C., Epard, J.L., and Steck, A., 2002, Thrusting, extension, and doming during the polyphase tectonometamorphic evolution of the High Himalayan Crystalline Zone in NW India: Journal of Asian Earth Sciences, v. 21, p. 221–239, doi:10.1016/S1367-9120 (02)00039-1.

Robyr, M., Hacker, B.R., and Mattinson, J.M., 2006, Doming in compressional orogenic settings: New geochronological constraints from the NW Himalaya: Tectonics, v. 25, p. 1–19, doi:10.1029/2004TC001774.

Rosenberg, C.L., and Handy, M.R., 2005, Experimental deformation of partially melted granite revisited: Implications for the continental crust: Journal of Metamorphic Geology, v. 23, p. 19–28, doi:10.1111/j.1525-1314.2005.00555.x.

Rowley, D.B., 1996, Age of initiation of collision between India and Asia: A review of stratigraphic data: Earth and Planetary Science Letters, v. 145, p. 1–13, doi:10.1016/S0012-821X(96)00201-4.

Rubatto, D., Chakraborty, S., and Dasgupta, S., 2013, Timescales of crustal melting in the Higher Himalayan Crystallines (Sikkim, Eastern Himalaya) inferred from trace element–constrained monazite and zircon chronology: Contributions to Mineralogy and Petrology, v. 165, p. 349–372, doi:10.1007/s00410-012-0812-y.

Sachan, H.K., Kohn, M.J., Saxena, A., and Corrie, S.L., 2010, The Malari leucogranite, Garhwal Himalaya, northern India: Chemistry, age, and tectonic implications: Geological Society of America Bulletin, v. 122, p. 1865–1876, doi:10.1130/B30153.1.

Sander, B., 1950, Einfuehrung in die Gefuegekunde der Geologischen Koerper; Zweiter Teil, Die Korngefuege: Wien-Innsbruck, Springer-Verlag.

Schärer, U., 1984, The effect of initial ^{230}Th disequilibrium on young U-Pb ages: The Makalu case, Himalaya:

Earth and Planetary Science Letters, v. 67, p. 191–204, doi:10.1016/0012-821X(84)90114-6.

Schmid, S.M., and Casey, M., 1986, Complete fabric analysis of some commonly observed quartz c-axis patterns, *in* Hobbs, B.E., and Heard, H.C., eds., Deformation of Rocks: Laboratory Studies: American Geophysical Union, Washington, Geophysical Monograph, v. 36, p. 263–286.

Searle, M.P., 1986, Structural evolution and sequence of thrusting in the High Himalayan, Tibetan-Tethys and Indus suture zones of Zanskar and Ladakh, Western Himalaya: Journal of Structural Geology, v. 8, p. 923–936, doi:10.1016/0191-8141(86)90037-4.

Searle, M.P., and Godin, L., 2003, The South Tibetan detachment and the Manaslu leucogranite: A structural reinterpretation and restoration of the Annapurna-Manaslu Himalaya, Nepal: The Journal of Geology, v. 111, p. 505–523, doi:10.1086/376763.

Searle, M.P., and Rex, A.J., 1989, Thermal model for the Zanskar Himalaya: Journal of Metamorphic Geology, v. 7, p. 127–134, doi:10.1111/j.1525-1314.1989.tb00579.x.

Searle, M.P., Waters, D.J., Dransfield, M.W., Stephenson, B.J., Walker, C.B., Walker, J.D., and Rex, D.C., 1999, Thermal and mechanical models for the structural and metamorphic evolution of the Zanskar High Himalaya, *in* Mac Niocaill, C., and Ryan, P.D., eds., Continental Tectonics: Geological Society of London Special Publication 164, p. 139–156.

Searle, M.P., Simpson, R.L., Law, R.D., Parrish, R.R., and Waters, D.J., 2003, The structural geometry, metamorphic and magmatic evolution of the Everest Massif, High Himalaya of Nepal-South Tibet: Journal of the Geological Society of London, v. 160, p. 345–366, doi:10.1144/0016-764902-126.

Steck, A., Spring, L., Vannay, J.C., Masson, H., Stutz, E., Bucher, H., Marchant, R., and Tieche, J.C., 1993, Geological transect across the northwestern Himalaya in eastern Ladakh and Lahul (a model for the continental collision of India and Asia): Eclogae Geologicae Helvetiae, v. 86, p. 219–263.

Stern, R.A., and Berman, R.G., 2000, Monazite U-Pb and Th-Pb geochronology by ion microprobe, with an application to in situ dating of an Archean metasedimentary rock: Chemical Geology, v. 172, p. 113–130, doi:10.1016/S0009-2541(00)00239-4.

Stipp, M., Stünitz, H., Heilbronner, R., and Schmid, S.M., 2002, The eastern Tonale fault zone: A 'natural laboratory' for crystal plastic deformation of quartz over a temperature range from 250 to 700 °C: Journal of Structural Geology, v. 24, p. 1861–1884, doi:10.1016/S0191-8141(02)00035-4.

Stutz, E., and Thöni, M., 1987, The lower Paleozoic Nyimaling Granite in the Indian Himalaya (Ladakh): New Rb/Sr data versus zircon typology: Geologische Rundschau, v. 76, p. 307–315, doi:10.1007/BF01821076.

Tera, G., and Wasserburg, T.F., 1972, U-Th-Pb systematics in three *Apollo 14* basalts and the problem of initial Pb in lunar rocks: Earth and Planetary Science Letters, v. 14, p. 281–304, doi:10.1016/0012-821X (72)90128-8.

Thiede, R.C., Arrowsmith, J.R., Bookhagen, B., McWilliams, M., Sobel, E.R., and Strecker, M.R., 2006, Dome formation and extension in the Tethyan Himalaya, Leo Pargil, northwest India: Geological Society of America Bulletin, v. 118, p. 635–650, doi:10.1130/B25872.1.

Thöni, M., Miller, C., Hager, C., Grasemann, B., and Horschinegg, M., 2012, New geochronological constraints on the thermal and exhumation history of the Lesser and Higher Himalayan Crystalline Units in the Kullu-Kinnaur area of Himachal Pradesh (India): Journal of Asian Earth Sciences, v. 52, p. 98–116, doi:10.1016/j.jseaes.2012.02.015.

Toy, V.G., Prior, D.J., and Norris, R.J., 2008, Quartz fabrics in the Alpine fault mylonites: Influence of pre-existing preferred orientations on fabric development during progressive uplift: Journal of Structural Geology, v. 30, p. 602–621, doi:10.1016/j.jsg.2008.01.001.

Vance, D., and Harris, N., 1999, Timing of prograde metamorphism in the Zanskar Himalaya: Geology, v. 27, p. 395–398, doi:10.1130/0091-7613(1999)027<0395: TOPMIT>2.3.CO;2.

Vannay, J.C., and Hodges, K.V., 1996, Tectonometamorphic evolution of the Himalayan metamorphic core between the Annapurna and Dhaulagiri, central Nepal: Journal of Metamorphic Geology, v. 14, p. 635–656, doi:10.1046/j.1525-1314.1996.00426.x.

Vannay, J.C., Grasemann, B., Rahn, M., Frank, W., Carter, A., Baudraz, V., and Cosca, M., 2004, Miocene to Holocene exhumation of metamorphic crustal wedges in the NW Himalaya: Evidence for tectonic extrusion coupled to fluvial erosion: Tectonics, v. 23, TC1014, doi:10.1029/2002TC001429.

Vernon, R.H., 1991, Questions about myrmekite in deformed rocks: Journal of Structural Geology, v. 13, p. 979–985, doi:10.1016/0191-8141(91)90050-S.

Viskupic, K., Hodges, K.V., and Bowring, S., 2005, Timescales of melt generation and the thermal evolution of the Himalayan metamorphic core, Everest region, eastern Nepal: Contributions to Mineralogy and Petrology, v. 149, p. 1–21, doi:10.1007/s00410-004-0628-5.

Walker, C.B., Searle, M.P., and Waters, D.J., 2001, An integrated tectonothermal model for the evolution of the High Himalaya in western Zanskar with constraints from thermobarometry and metamorphic modeling: Tectonics, v. 20, p. 810–833, doi:10.1029/2000TC001249.

Walker, J.D., Martin, M.W., Bowring, S.A., Searle, M.P., Waters, D.J., and Hodges, K.V., 1999, Metamorphism, melting, and extension: Age constraints from the High Himalayan slab of southeast Zanskar and northwest Lahaul: The Journal of Geology, v. 107, p. 473–495, doi:10.1086/314360.

Webb, A.A.G., Yin, A., Harrison, T.M., Célérier, J., and Burgess, W.P., 2007, The leading edge of the Greater Himalayan Crystalline complex revealed in the NW Indian Himalaya: Implications for the evolution of the Himalayan orogen: Geology, v. 35, p. 955–958, doi:10.1130/G23931A.1.

Webb, A.A.G., Yin, A., Harrison, T.M., Célérier, J., Gehrels, G.E., Manning, C.E., and Grove, M., 2011, Cenozoic tectonic history of the Himachal Himalaya (northwestern India) and its constraints on the formation mechanism of the Himalayan orogen: Geosphere, v. 7, p. 1013–1061, doi:10.1130/GES00627.1.

Weinberg, R.F., Mark, G., and Reichardt, H., 2009, Magma ponding in the Karakoram shear zone, Ladakh, NW India: Geological Society of America Bulletin, v. 121, p. 278–285, doi:10.1130/B26358.1.

White, R.W., Powell, R., Holland, T.J.B., and Worley, B.A., 2000, The effect of TiO_2 and Fe_2O_3 on metapelitic assemblages at greenschist and amphibolite facies conditions: Mineral equilibria calculations in the system $K_2O-FeO-MgO-Al_2O_3-SiO_2-H_2O-TiO_2-Fe_2O_3$: Journal of Metamorphic Geology, v. 18, p. 497–511, doi:10.1046/j.1525-1314.2000.00269.x.

White, R.W., Powell, R., and Clarke, G.L., 2002, The interpretation of reaction textures in Fe-rich metapelitic granulites of the Musgrave block, central Australia: Constraints from mineral equilibria calculations in the system $K_2O-FeO-MgO-Al_2O_3-SiO_2-H_2O-TiO_2-Fe_2O_3$: Journal of Metamorphic Geology, v. 20, p. 41–55, doi:10.1046/j.0263-4929.2001.00349.x.

White, R.W., Pomroy, N.E., and Powell, R., 2005, An in-situ metatexite-diatexite transition in upper amphibolite facies rocks from Broken Hill, Australia: Journal of Metamorphic Geology, v. 23, p. 579–602, doi:10.1111/j.1525-1314.2005.00597.x.

Williams, I.S., 1998, U-Th-Pb Geochronology by ion microprobe, *in* McKibben, M.A., Shanks III, W.C., and Ridley, W.I., eds., Applications of Microanalytical Techniques to Understanding Mineralizing Processes: Reviews in Economic Geology, v. 7, p. 1–35.

Williams, I.S., and Hergt, J.M., 2000, U-Pb dating of Tasmanian dolerites: A cautionary tale of SHRIMP analysis of high-U zircon, *in* Woodhead, J.D., Hergt, J.M., and Noble, W.P., eds., Proceedings, Beyond 2000 New Frontiers in Isotope Geoscience, Lorne, January–February 2000: Melbourne, University of Melbourne, p. 185–188.

Williams, I.S., Buick, I.S., and Cartwright, I., 1996, An extended episode of early Mesoproterozoic metamorphic fluid flow in the Reynolds Range, central Australia:

Switch from thrusting to normal shearing in the Zanskar shear zone, NW Himalaya: Implications for channel flow

Journal of Metamorphic Geology, v. 14, p. 29–47, doi: 10.1111/j.1525-1314.1996.00029.x.

Wilson, C.J.L., Russell-Head, D.S., and Sim, H.M., 2003, The application of an automated FA system to the textural evolution of folded ice layers in shear zones: Annals of Glaciology, v. 37, p. 7–17, doi:10.3189 /172756403781815401.

Wilson, C.J.L., Russell-Head, D.S., Kunze, K., and Viola, G., 2007, The analysis of quartz *c*-axis fabrics using a modified optical microscope: Journal of Microscopy, v. 227, p. 30–41, doi:10.1111/j.1365-2818.2007 .01784.x.

Yin, A., 2006, Cenozoic tectonic evolution of the Himalayan orogen as constrained by along-strike variation of structural geometry, exhumation history, and foreland sedimentation: Earth-Science Reviews, v. 76, p. 1–131, doi:10.1016/j.earscirev.2005.05.004.

Zeitler, P.K., Chamberlain, C.P., and Smith, H.A., 1993, Synchronous anatexis, metamorphism, and rapid denudation at Nanga Parbat (Pakistan Himalaya): Geology, v. 21, p. 347–350, doi:10.1130/0091-7613(1993)021 <0347:SAMARD>2.3.CO;2.

Zhang, H., Harris, N., Parrish, R., Kelley, S., Zhang, L., Rogers, N., Argles, T., and King, J., 2004, Causes and consequences of protracted melting of the mid-crust exposed in the North Himalayan antiform: Earth and Planetary Science Letters, v. 228, p. 195–212, doi: 10.1016/j.epsl.2004.09.031.

Zhu, X.K., and O'Nions, R.K., 1999, Monazite chemical composition: Some implications for monazite geochronology: Contributions to Mineralogy and Petrology, v. 137, p. 351–363, doi:10.1007/s004100050555.